

ABSTRACT

LAM, LETISHA MCLAUGHLIN. Mechanical Strength and Stability of DNA-modified Gold Nanoparticle Systems. (Under the direction of Professor Mohammed Zikry).

Systems in which gold nanoparticles (AuNPs) are functionalized with DNA have the potential for a broad range of applications in gene regulation therapies, drug delivery, sensing, innovative biomaterials and material templates. The use of DNA-modified gold nanoparticle (AuNP-DNA) systems is driven by their ease of assembly with bottom-up methods as well as the tunability of the systems' mechanical, optical, and electronic properties by exploiting AuNP characteristics and behavior in a multi-particle arrangement. Periodic arrangements of AuNPs precisely distributed through ligated DNA linkers may be assembled and used on relatively large length scales, on the order of hundreds of nanometers, for use in potential nanoscale technologies and applications. However, because of the size and heterogeneous composition of AuNP-DNA systems, their stability under mechanical loading is not well understood or quantified on relevant physical scales for these applications.

Hence, a large-scale specialized finite-element predictive approach with a dislocation-density based crystalline plasticity has been used to investigate the mechanical stability of AuNP-DNA-ligand systems with AuNPs within the physical dimensions required for plasmon resonance. The crystalline formulation for the AuNPs accounts for multiple crystalline slip, dislocation-density evolution, lattice rotations, and large inelastic strains. A hypoelastic formulation was used for the DNA and the ligands. The nonlinear finite-element scheme is based on accounting for finite elastic and inelastic strains. These approaches were employed to predict and understand the fundamental scale-dependent microstructural

behavior, the evolving heterogeneous microstructure, and localized phenomena that can contribute to failure initiation and instability. Each system was loaded using quasi-static plane strain tension and compression to simulate application loading conditions, and the elastic and inelastic evolutions were analyzed for evidence of mechanical strengthening as well as possible failure modes. To establish a foundation for AuNP-DNA stability analysis, several different two-particle conformations were investigated, including systems with pentagonally twinned AuNPs, systems with circular AuNPs, systems with non-textured and textured cuboctahedron AuNPs with 6 nm DNA, 12 nm DNA, and 18 nm DNA. In general, the analyses indicated that the systems' stability are mainly affected by large stress gradients at AuNP-ligand interfaces, as well as large dislocation-density, normal stresses, and inelastic accumulations in the region adjacent to these interfaces between the AuNPs and the DNA. The predictions also indicate that highly faceted f.c.c. AuNPs with DNA lengths of approximately 6 nm in biaxial loading conditions were found to have the highest strength and overall stability.

Furthermore, periodic AuNP-DNA superlattice composites, which mimic the crystallography of f.c.c. atomic lattices, were investigated for mechanical effectiveness as both a composite material and thin film. This investigation analyzed the stress behavior and inelastic evolution of f.c.c. AuNP-DNA superlattice systems with different Au volume fractions, matrix strengths, intrinsic nanoparticle crystallographic orientations and sizes. These analyses were also extended to superlattice f.c.c. composites on a silicon substrate. The results indicate that f.c.c. AuNP-DNA superlattices have a combination of high strength and toughness due to the ductile nature of the nanoparticles in conjunction with the physical

properties of the DNA and matrix materials. The superlattice films also exhibited high strengths and toughness, with the limiting factor being the interrelated aspects of film thickness and delamination. These predictions can be used as guidelines for using these composites, superlattices, and thin films as candidates for innovative building blocks for new material systems.

© Copyright 2013 Letisha McLaughlin Lam

All Rights Reserved

Mechanical Strength and Stability of DNA-modified Gold Nanoparticle Systems.

by
Letisha McLaughlin Lam

A dissertation submitted to the Graduate Faculty of
North Carolina State University
in partial fulfillment of the
requirements for the degree of
Doctor of Philosophy

Mechanical Engineering

Raleigh, North Carolina

2014

APPROVED BY:

Dr. Mohammed Zikry
Committee Chair

Dr. Kara Peters

Dr. Yong Zhu

Dr. Joe Tracy

DEDICATION

This dissertation is dedicated to everyone who has helped me to become the person that I am today: Mom, Jack, PJ, Alisha, Nikkie, Logan, Danielle, Greg, and so many more, including family, friends, and professors. It is impossible for you all to know how much you inspire me.

BIOGRAPHY

Letisha McLaughlin Lam, née Letisha Annette McLaughlin, was born in Asheboro, NC, in 1984. She attended Southwestern Randolph High School, and graduated in 2002. She continued her studies for two years at Randolph Community College, and then transferred to the University of North Carolina at Wilmington where she graduated *magna cum laude* with a Bachelor of Science in physics and a minor in mathematics in 2007. The same year, she enrolled in North Carolina State University's graduate school in physics. In 2010, she received a Master of Science with a concentration in astrophysics, including a completed thesis, *X-ray Observations of G296.8-0.3*.

ACKNOWLEDGMENTS

It is very important for me to acknowledge everyone who has helped me to this point, both professionally and otherwise.

Thank you Professor Zikry for your guidance and expertise. Not only have I learned much about mechanical engineering, but have also developed a mindset for research, publishing, and professionalism thanks to you.

To my PhD dissertation committee: Dr. Kara Peters, Dr. Yong Zhu, Dr. Joe Tracy and Dr. Elizabeth Dickey, I am grateful for your time and guidance.

Support from the National Science Foundation under grant #553463 is gratefully acknowledged.

Also, I would like to thank my officemates for the past three years: Tarek Hatem, Khalil Elkhodary, Pratheek Shanthraj, Siqi Xu, William Lee, Prasenjit Khanikar, Drew LaBarbera, Qifeng Wu, Shoayb Ziaei, Judy Brown, Bingxiao Zhao, Tamir Hasan, and Matt Bond. Much of what I've learned over the past three years was through conversations with you. It has been a pleasure to both cut up and get down to business with you all.

A great deal of appreciation also goes out to my past teachers and professors. Starting from high school, you all inspired me to pursue a life in the sciences.

I am also grateful for my many mentors along the way, including Dr. Russell Herman at UNCW, Dr. Sabrina Savage at NASA Marshall Space Flight Center, and Dr. David McKenzie at Montana State University at Bozeman.

Thanks also to the wonderful women role models by whom I have had the pleasure of being inspired to continue all the way to the PhD, even if it was by only a single

conversation. Thank you, Dr. Anne Cutter, Dr. Gail McLaughlin, Dr. Shadow Huang, Dr. Sabrina Savage, Dr. Elizabeth Dickey, Dr. Kara Peters, and Dr. Liping Gan.

Thank you to all the Lams and Ledfords for your support these past few years. A special thanks to Sandy, for the many graduate school related conversations, and Mrs. Lam for the delicious meals that kept me going.

Also I am extremely grateful to my siblings, PJ, Nikkie, and Alisha, for always believing in me and indulging me when the conversation turned to science. I appreciate every trip to the zoo and science museums. I look forward to inspiring Logan, Nate, Makayla, Emma, Jonathan and Banner into a life in science.

To my mother: thank you for always being there for me, and supporting me every step of the way. It means so much to me to be able to make you proud. You singlehandedly kindled my passion for science when you bought me that first telescope in the 7th grade, and I have been so lucky to have you on my side through every challenge since.

Finally, I owe a very special thanks to my husband, Dr. Jack Lam. Your support is seemingly endless. Through you I have gained so much, not limited to the love you have given me, the strength you have instilled in me, and the ever flowing well of knowledge and advice that is you. You are amazing.

TABLE OF CONTENTS

LIST OF TABLES	viii
LIST OF FIGURES	ix
CHAPTER 1: Introduction	1
1.1 Overview	1
1.2 Research Objectives and Approach	4
1.3 Dissertation Organization	5
REFERENCES—Chapter 1	6
CHAPTER 2: Dislocation-Density Based Crystalline Plasticity Constitutive Formulation	11
2.1 Gold Nanoparticles: Multiple Slip Crystalline Plasticity Formulation	12
2.2 Dislocation Density Evolution	14
2.3 DNA and Ligands: Isotropic Elasticity	19
REFERENCES—Chapter 2	21
CHAPTER 3: Numerical Methods	25
3.1 Total Velocity Gradient	25
3.2 Plastic Velocity Gradient	27
REFERENCES—Chapter 3	29
CHAPTER 4: Mechanical Strength and Stability of Two-particle DNA-modified Gold Nanoparticle Systems	30
4.1 Approach	31
4.2 Results	33
4.2.1 Non-textured Cuboctahedron NPs with 6 nm DNA	33
4.2.2 AuNP Morphology	34
4.2.3 AuNP Orientation and Texture	36
4.2.4 DNA Length	37
4.2.5 Biaxial Loading Condition	38
4.3 Conclusions	38
REFERENCES—Chapter 4	41
CHAPTER 5: Strength of AuNP-DNA Superlattice Systems	62
5.1 Motivation	62
5.2 Results	64
5.2.1 Effects of DNA and Ligands	66
5.2.2 Effects of Superlattice Crystallographic Orientation with Respect to the Loading Axis	69
5.2.3 Effects of Matrix Strength and Load Transfer	70
5.2.4 Effects of AuNP Orientations with Respect to the Loading Axis	71
5.2.5 Effect of Volume Fraction	73
5.3: Conclusions	74
REFERENCES—Chapter 5	75

CHAPTER 6: AuNP-DNA Superlattice Thin Films	90
6.1 Approach.....	91
6.2 Results.....	93
6.2.1 Thin Film Superlattice Behavior in Compression and Tension.....	93
6.2.2 Film-substrate Strength and Behavior	95
6.3 Conclusions.....	96
CHAPTER 6 – References.....	97
CHAPTER 7: Future Research Recommendations	112
Chapter 7 – References	113

LIST OF TABLES

Table 2.1: Summary of interactions and coefficient values in an f.c.c. crystal.	23
Table 2.2: g-coefficients for dislocation-density evolution equations.	24
Table 4.1: Elastic properties of the AuNP-DNA components.	42
Table 5.1: Elastic properties of the AuNP-DNA components.	78
Table 6.1: Elastic properties of the AuNP-DNA superlattices and Si matrix.	99

LIST OF FIGURES

Figure 1.1: Colloidal gold nanoparticle solutions demonstrating the AuNP size dependence on visible wavelength absorption (Mandela, 2012).	8
Figure 1.2: Two gold nanoparticles functionalized with oligonucleotides.	9
Figure 1.3: TEM observations of nanoparticles embedded in silica (Auyeung, Macfarlane, Choi, Cutler, & Mirkin, 2012).	10
Figure 4.1: Euler angle computations for the textured cuboctahedral nanoparticles.	43
Figure 4.2: The heterogeneous AuNP-DNA system in plane strain uniaxial displacement loading (<i>red arrows</i>) and plane strain biaxial displacement loading (<i>red + black arrows</i>).	44
Figure 4.3: Normalized (a) lateral, (b) normal, (c) shear, and (d) z-axis lateral stress for a system of 20 nm AuNPs with 6 nm DNA at 2% nominal compressive strain.	45
Figure 4.4: AuNP plasticity: (a) Immobile and (b) mobile dislocation-densities and (c) slip rates for 6 nm DNA and 20 nm non-textured AuNPs for the most active slip system (1-11)[011]. All values are normalized to their pre-loading values. Shear slip is also shown (d). Regions left blank have no plastic accumulation.	48
Figure 4.5: Normalized normal stresses for 13.5 nm pentagonal nanoparticles with 6 nm DNA and (b) for 20 nm circular nanoparticles with 6 nm DNA.	51
Figure 4.6: Normalized lateral stresses for 13.5 nm pentagonal nanoparticles with 6 nm DNA and (b) for 20 nm circular nanoparticles with 6 nm DNA.	52
Figure 4.7: (a) Shear slip for 13.5 nm pentagonal particles. (b) Shear slip and (c) slip rates for the most active slip system (1-11)[011] for 20 nm circular nanoparticles.	53
Figure 4.8: (a) Normalized lateral stress and (b) shear strain for 6 nm DNA and rotated, non-textured cuboctahedral particles.	56
Figure 4.9: (a) Shear slip, (b) immobile dislocation-density for the most active slip system (111)[-1-10], (c) immobile dislocation-density for the second most active slip system (111)[0-1-1], and (d) slip rates for the most active slip system (111)[-1-10].	57
Figure 4.10: Normalized normal stress in systems with (a) 12 nm and (b) 18 nm DNA. Compare with figure 4.3a.	60

Figure 4.11: (a) Normalized normal stress and (b) shear slip for the system with biaxial displacement loading conditions at 1.2% nominal compressive strain.....	61
Figure 5.1: An f.c.c. superlattice with AuNPs, DNA, and ligands (<i>inset</i>). The (1 1 1) close packed plane is shown, and loading is applied along the [1 1 -2] direction.	79
Figure 5.2: Normal stresses for a {1 1 1} cross section of an f.c.c. AuNP-DNA superlattice (<i>left</i>), AuNPs/matrix composite with the same nanoparticle-spacing without DNA (<i>middle</i>), and AuNPs/matrix composite with random nanoparticle spacing without DNA (<i>right</i>). The ligand and DNA attachments concentrate stresses at the ligand-AuNP interface.....	80
Figure 5.3: Global and local stress-strain curves for AuNP composites with and without DNA. (<i>Left</i>) When the AuNPs are regularly spaced using DNA (<i>blue</i>) a lower nominal stress is required to strain the material than when DNA is absent (<i>red</i>). However, the local stress-strain curve for one AuNP in the superlattice (<i>see inset for nanoparticle location</i>) and AuNP-matrix composite (<i>right</i>) reveal strengthening of the nanocrystals with the presence of the DNA. ..	81
Figure 5.4: Immobile dislocation-densities for superlattices and AuNP-matrix composites without DNA linkers. Concentrated regions of stress in AuNPs resulting from ligand and DNA linkers in AuNP-DNA superlattices resulted in high dislocation-density accumulation adjacent to the attachment region. Dislocation-densities were uniform for the systems without DNA linkers (<i>center</i>) and (<i>right</i>).....	82
Figure 5.5: Shear slip for superlattices and AuNP-matrix composites without DNA linkers. Concentrated regions of stress in AuNPs resulting from ligand and DNA linkers in AuNP-DNA superlattices resulted in higher slip adjacent to the attachment region. Shear slip was similar for the systems without DNA linkers (<i>center</i>) and (<i>right</i>).....	83
Figure 5.6: Effects of loading direction and anisotropy on stress. Normal stresses are shown along the components in two directions relative to loading, the [-1 1 0] and [1 0 1] directions. The interfacial stress gradients strongly correlate with loading direction.	84
Figure 5.7: Global stress-strain curves for AuNP-DNA superlattices (<i>left</i>) and normal stress contours (<i>right</i>) with (a) $E_{matrix} = 1/4 E_{Au}$; (b) $E_{matrix} = 1/10 E_{Au}$; (c) $E_{matrix} = 1/100 E_{Au}$	85
Figure 5.8: Immobile dislocation densities for three AuNP-DNA superlattice composites with different AuNP orientations for slip system (111) [-1 0 1]. The magnitudes of dislocation-densities are highly dependent on the orientation of each AuNP with respect to the loading axis, as shown by (<i>left</i>) uniform orientation alignment, (<i>center</i>) low angle alignment orientations, and	

(right) high angle alignment orientations. The dislocation-densities have been normalized to their initial values.....	86
Figure 5.9: Shear slip for three AuNP-DNA superlattice composites with different AuNP orientations for slip system (111) [-1 0 1] for (left) uniform alignment orientations, (center) low angle random orientations, and (right) high angle alignment orientations.....	87
Figure 5.10: Normal stress for different volume fraction but the same hydrodynamic radius.....	88
Figure 5.11: Shear slip for different volume fraction and the same hydrodynamic radius.....	89
Figure 6.1: The thin film model. The dashed line represents the continuous boundary between the substrate and the encapsulated Si particle lattice.....	100
Figure 6.2: The superlattice-Si composite model.	101
Figure 6.3: Normal stress in the f.c.c. superlattice thin film in compression. The dashed line represents the continuous interface between the substrate and the encapsulated Si particle lattice.....	102
Figure 6.4: Normal stresses in the f.c.c. superlattice thin film in tension.....	103
Figure 6.5: Shear stresses for the AuNP-DNA thin film in compression.	104
Figure 6.6: Shear stress for the AuNP-DNA superlattice thin film in tension.	105
Figure 6.7: Shear slip for a thin film in displaced to 1.6% nominal compressive strain. Highest plasticity occurred in the deformed AuNP shown in the inset. ...	106
Figure 6.8: Shear slip for a thin film in displaced to 1.6% nominal tensile strain. Highest plasticity occurred in the central most AuNP, as shown in the inset.	107
Figure 6.9: Mobile dislocation-densities are lower for the AuNP-DNA superlattice (right) than the thin film (left) for the most active slip system (-1 1 1) [0 -1 1]. .	108
Figure 6.10: Stress-strain curves for (red) the AuNP-DNA superlattice thin film and (blue) the AuNP-DNA lattice coating only (see Figure 6.1,2).	109
Figure 6.11: Normal stress in the f.c.c. superlattice-Si composite.	110
Figure 6.12: Normal stresses for the thin film in compression with contours adjusted to emphasize compressive stress contribution from the superlattice into the substrate.	111

CHAPTER 1: Introduction

1.1 Overview

Gold nanoparticles have been used throughout history for a variety of reasons ranging from art to medicine. Their popularity stems from the unique optical and electronic properties exhibited by gold crystals at nano-length scales, as opposed to characteristics found in bulk Au. For instance, a large nugget of gold appears its namesake color in the visible spectrum, but if many small gold particles are distributed in liquid, as in a colloidal solution, the mixture's color may appear blue, violet, or red depending on the sizes, shapes and distances between each particle (see Figure 1.1). This is because of a phenomenon called local surface plasmon resonance (LSPR), where photoexcitation causes conduction electrons in the Au particles to oscillate coherently, causing strong absorption of visible and UV wavelengths (Kelly, *et al.*, 2003). It is, in fact, their physical dimensions that dictate the interactions AuNPs have with incoming light, and similar absorptions occur for differently shaped and spaced AuNPs. Hence, precisely changing the dimensions of AuNPs in colloidal solutions allows one to tailor their desired optical and electronic characteristics.

Another benefit of AuNPs is their ability to easily functionalize with small molecules, called ligands. The high surface energies of the nanocrystals result in elevated reactivities, so that citrate molecules and thiols readily bind to their surfaces (Frens, 1973; Ulman, 1996). Ligands may be chosen such that other molecules, and even particles, may be easily linked to AuNPs, creating a great number of possible nanoparticle assemblies.

There are many uses for the interesting optical and electronic properties, as well as functionalization, of AuNPs. Currently, AuNPs are used for drug delivery and therapeutics,

sensing and diagnostics, and catalysis. In photothermal therapy, lasers are focused onto near IR-absorbing NPs that, in turn, produce damaging heat to targeted cells, such as tumors (El-Sayed, Huang, & El-Sayed, 2006; Huang, Jain, El-Sayed, & El-Sayed, 2008). Gold nanoparticles are well-suited for *in vivo* therapies, and are readily uptaken by cellular cytoplasm. However, when the AuNPs are capped with a peptide complex, uptake is more effective and NPs can enter into the nucleus with a 95% cell viability (Tkachenko, *et al.*, 2003). Hence, coated NPs may also be used for gene and drug delivery by using a ligand to attach the therapeutic payload without fear of toxic consequence. Additionally, colorimetric sensing, which exploits the color changes in the visible spectrum of colloidal AuNPs, provides a quick and effective method of detecting a specific substance or DNA sequence. For example, Kim *et al.* utilized AuNPs to positively detect heavy metal, and otherwise toxic ions by indirectly observing NP aggregation in the form of shifts in the solution's absorption spectrum when in the presence of such ions (2001).

One method of colorimetric sensing gaining momentum involves the use of DNA, or deoxyribonucleic acid, as a means to bring about controlled AuNP aggregation upon positive species identification. This process works by first chemically inducing the assembly of NPs with single strands of DNA (ssDNA) by using a short molecule, called a ligand, to coordinate DNA-AuNP bonding. The ssDNA-capped NPs are then introduced to certain probes that cause hybridization of the single-strands of DNA, hence bringing the AuNPs closer together as double-stranded DNA (dsDNA) is formed (Figure 1.2). In one such experiment, Elghanian *et al.* utilized mercaptoal-kyoligonucleotide-modified gold nanoparticles in a solution that exhibited a red to pinkish-purple color change when exposed to an identifying

probe (1997). These tests are powerful tools because they may be conducted in a single vial, test tube, or other container and the components of the system- DNA, AuNPs, and solutions- are readily available. Furthermore, DNA-AuNP colorimetric sensors provide results quickly and, in most cases, may be analyzed using the unaided eye.

As with colorimetric testing, DNA is participating in increasingly new and interesting roles in the sciences of sensing and materials because of its unique structure and binding capacity. For all living organisms and some viruses, DNA contains genetic code in the form of nucleotide bases chemically bonded to a backbone of alternating sugar and phosphate groups. The double helix structure is due to the complementary base pairing of cytosine (C) with guanine (G) and adenine (A) with thymine (T). Several stereochemical forms of DNA exist depending on the quantity of water molecules and ions present in the DNA solution. B-form DNA, for example, has an average of 3.4 Å between basal planes and a diameter of approximately 20 Å, while A-form DNA has 2.55 Å between basal planes and a 26 Å diameter (Dickerson, Drew, Conner, Wing, Fratini, & Kopka, 1982). The distance between basal planes is also called the rise per base pair, and defines the spacing between nucleotides along the helical backbone. For double-stranded B-form DNA, the rise per base pair and diameter fluctuate little along the strand length, allowing precise measurement of DNA length when the number of base pairs is known. For this reason, DNA has been employed as a ruler to precisely quantify the lengths of nanoscale matter. In many cases, molecules that absorb and reflect specific wavelengths or plasmon-exhibiting noble metal nanoparticles, like gold and silver, are tethered to ssDNA. During a DNA hybridization event, the NPs aggregate causing plasmons of nearby NPs to couple, causing a shift in absorbance

wavelengths (Qian, Zhou, & Nie, 2008; Sonnichsen, Reinhard, Liphardt, & Alivisatos, 2005).

From the examples above, the combination of gold nanoparticles and DNA in a single system has been shown here to have potential in a diverse range of scientific disciplines. Furthermore, AuNP-DNA systems can also be developed using bottom-up techniques in which the system can be assembled by taking advantage of the chemical properties of the AuNPs, ligands, and DNA (Winfrey, Liu, Wenzier, & Seeman, 1998). Utilizing the unique optical and electronic properties of gold and the special structure of DNA together create even more possibilities to develop tailored systems. Mirkin *et al.* have created systems of AuNPs and DNA with periodic spacing of the NPs that mimic crystallographic formations. For instance, for an f.c.c. lattice, atoms are replaced by AuNPs while DNA acts as the rod between NPs giving them their periodic spacing. These superlattices have been successfully assembled over several hundred nanometers and have been encapsulated in silica to allow the periodic arrangements to tolerate environments other than the solutions in which it is assembled (see Figure 1.3). This method of creating relatively large, regular AuNP-DNA structures exploits the fundamental optical and electronic properties of AuNPs while enlarging its application potential, including the development of nanomaterials and devices.

1.2 Research Objectives and Approach

The goals of this research are to address the limitations and possible failure mechanisms of AuNP-DNA systems by using a physically relevant analysis that represents the entire AuNP-DNA system. This study investigates AuNP-DNA systems' strength and stability using a large-scale finite-element approach and a dislocation-density based crystalline

plasticity model to represent the behavior of the Au nanoparticles, and a hypoelasticity model to represent the behavior of the ligands and DNA. The composite AuNP-DNA systems are exposed to various loading conditions representing application environments and their responses are calculated. The computational examinations include both AuNP-DNA systems in the elastic and plastic regime, allowing full-scale investigations of the composites' mechanical behaviors. The approach also focuses on the components of DNA-AuNP systems individually, allowing a qualitative investigation of material design. By modeling a portion of the system with, for example, different lengths of double-stranded DNA (dsDNA) and various shapes of AuNPs, the biomaterial may be optimized for maximum mechanical stability in future applications. Finally, to illuminate the performance of AuNP-DNA superlattices in applications, the analysis was scaled up to include multiple nanocrystals in an f.c.c. configuration with different volume fractions, matrix materials, and also modeled as a thin film with a silicon substrate.

1.3 Dissertation Organization

This dissertation is organized as follows: Chapter 2 contains the dislocation-density based crystalline plasticity constitutive formulation, which is used in conjunction with the finite element numerical methods covered in Chapter 3. Chapter 4 discusses two-particle AuNP systems and their mechanical strength and stability. Chapter 5 builds upon Chapter 4 by extending the investigation to larger f.c.c. AuNP-DNA superlattices. Finally, Chapter 6 examines the strength and failure mechanisms of f.c.c. superlattice composites in thin films. Future work is discussed in Chapter 7.

REFERENCES—Chapter 1

- Auyeung, E., Macfarlane, R. J., Choi, C. J., Cutler, J. I., & Mirkin, C. A. (2012). Transitioning DNA-engineered nanoparticle superlattices from solution to the solid state. *Advanced Materials*, *24*, 5181-5186.
- Dickerson, R. E., Drew, H. R., Conner, B. N., Wing, R. M., Fratini, A. V., & Kopka, M. L. (1982). The anatomy of A-, B-, and Z-DNA. *Science*, *216* (4545), 475-485.
- Elghanian, R., Storhoff, J. J., Mucic, R. C., Letsinger, R. L., & Mirkin, C. A. (1997). Selective colorimetric detection of polynucleotides on the distance-dependent optical properties of gold nanoparticles. *Science*, *277* (5329), 1078-1081.
- El-Sayed, I. H., Huang, X., & El-Sayed, M. A. (2006). Selective laser photo-thermal therapy of epithelial carcinoma using anti-EGFR antibody conjugated gold nanoparticles. *Cancer Letters*, *239* (1), 129-135.
- Frens, G. (1973). Controlled nucleation for regulation of particle-size in monodisperse gold suspensions. *Nature-Physical Science*, *241* (105), 20-22.
- Huang, X., Jain, P. K., El-Sayed, I. H., & El-Sayed, M. A. (2008). Plasmonic photothermal therapy (PPTT) using gold nanoparticles. *Lasers in Medical Science*, *23* (3), 217-228.
- Kelly, L. K., Coronado, E., Zhao, L. L., & Schatz, G. C. (2003). The optical properties of metal nanoparticles: the influence of size, shape, and dielectric environment. *Journal of Physical Chemistry B*, *107*, 668-677.
- Kim, Y., Johnson, R. C., & Hupp, J. T. (2001). Gold nanoparticle-based sensing of "spectroscopically silent" heavy metal ions. *Nano Letters*, *1* (4), 165-167.
- Mandela, I. (2012, 11 12). *Producing and conjugating colloidal metals*. Retrieved 01 22, 2013, from Biological & Biomaterials Preparation, Imaging, & Characterization Facility: <http://www.ansci.wisc.edu/bbpic/colloidalmetals.html>.
- Moore, A., & Le Floch, P. (2009). The metal nanoparticle plasmon band as a powerful tool for chemo- and biosensing. In A. Merkoci, *Biosensing using Nanomaterials* (pp. 137-176). Hoboken, NJ, USA: Wiley.
- Qian, X., Zhou, X., & Nie, S. (2008). Surface-enhanced Raman nanoparticle beacons based on bioconjugated gold nanocrystals and long range plasmonic coupling. *Journal of the American Chemical Society*, *130* (45), 14934-14935.

- Sonnichsen, C., Reinhard, B. M., Liphardt, J., & Alivisatos, A. P. (2005). A molecular ruler based on plasmon coupling of single gold and silver nanoparticles. *Nature Biotechnology*, 23 (6), 741-745.
- Storhoff, J. J., Lazarides, A. A., Mucic, R. A., Mirkin, C. A., Letsinger, R. L., & Schatz, G. C. (2000). What controls the optical properties of DNA-linked gold nanoparticle assemblies. *Journal of the American Chemical Society*, 122, 4640-4650.
- Tkachenko, A. G., Xie, H., Coleman, D., Glomm, W., Joseph, R., Anderson, M. F., *et al.* (2003). Multifunctional gold nanoparticle-peptide complexes for nuclear targeting. *Journal of the American Chemical Society*, 125 (16), 4700-4701.
- Ulman, A. (1996). Formation and structure of self-assembled monolayers. *Chemical Reviews*, 96 (4), 1533-1554.
- Winfrey, E., Liu, F., Wenzier, L. A., & Seeman, N. C. (1998). Design and self-assembly of two-dimensional DNA crystals. *Nature*, 394 (6693), 539-544.



Figure 1.1: Colloidal gold nanoparticle solutions demonstrating the AuNP size dependence on visible wavelength absorption (Mandela, 2012).

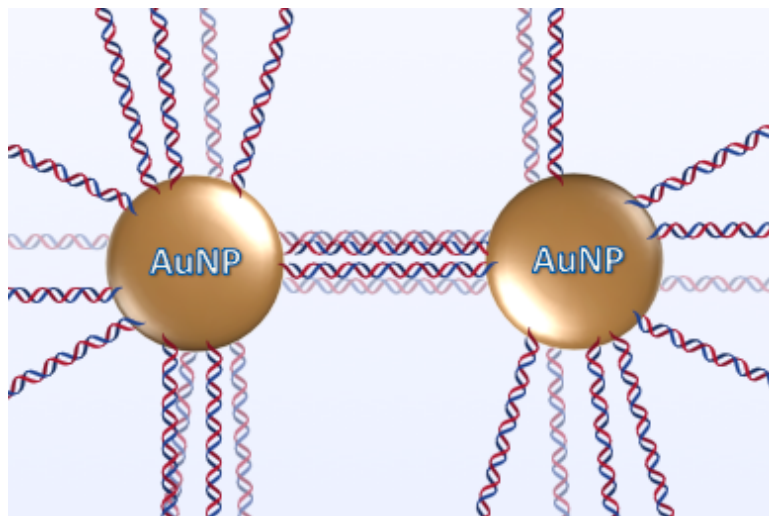


Figure 1.2: Two gold nanoparticles functionalized with oligonucleotides.

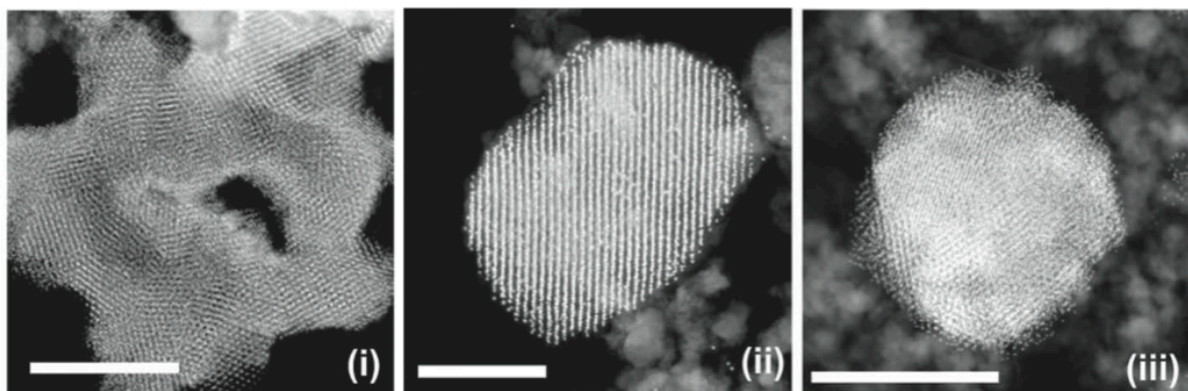


Figure 1.3: TEM observations of nanoparticles embedded in silica (Auyeung, Macfarlane, Choi, Cutler, & Mirkin, 2012).

CHAPTER 2: Dislocation-Density Based Crystalline Plasticity Constitutive Formulation

Many applications require AuNP-DNA systems to be mechanically and structurally stable, or to possess long-term stability for drug delivery and biomaterial applications. Additionally, AuNP-DNA systems have different requirements for particle and DNA conformations depending on the desired mechanical properties and behavior of the assembled system. For example, sensing applications requiring specific surface plasmon enhancement are based on tailoring AuNP sizes, orientations, and DNA lengths to achieve resonance (Storhoff, Lazarides, Mucic, Mirkin, Letsinger, & Schatz, 2000). Understanding the mechanical stability of the ensemble, as well as its individual constituents, is therefore essential to predict possible limitations of the system with respect to system stability and mechanical strength. *In situ* investigations using characterization techniques are lacking because imaging AuNPs and DNA simultaneously requires DNA staining. However, this staining would alter the elastic character of the DNA. Computational approaches, such as molecular dynamics (MD) and density functional theories (DFT), while providing valuable physical insights, are not suitable for the relatively long timescales and length scales, which are on the order of hundreds of nanometers.

Hence, this dissertation addresses the limitations and possible failure mechanisms of AuNP-DNA systems by using a physically relevant analysis that would represent the entire system. The strength and stability of Au-DNA-ligand systems was investigated using a large-scale finite-element approach and a dislocation-density based crystalline plasticity model to

represent the behavior of the Au nanoparticles, and a hypoelasticity model to represent the behavior of the ligands and DNA.

2.1 Gold Nanoparticles: Multiple Slip Crystalline Plasticity Formulation

The constitutive formulation for the AuNPs accounts for their multiple-slip behavior. A crystalline plasticity coupled to evolutionary equations for the dislocation-densities is used in the current investigation. A detailed description may be found in Orsini and Zikry (2001), Ashmawi and Zikry (2002), and Shanthraj and Zikry (2011) and only an outline will be presented here.

The velocity gradient, V_{ij} , is calculated from the deformation gradient, F_{ij} , as

$$V_{ij} = \dot{F}_{ik} \cdot F_{kj}^{-1}, \quad (2.1)$$

and then additively decomposed into the symmetric deformation rate tensor D_{ij} and an anti-symmetric spin tensor W_{ij}

$$V_{ij} = D_{ij} + W_{ij}, \quad (2.2)$$

where

$$D_{ij} = \frac{1}{2}(V_{ij} + V_{ji}), \quad W_{ij} = \frac{1}{2}(V_{ij} - V_{ji}). \quad (2.3a, b)$$

D_{ij} and W_{ij} are then additively decomposed into elastic and inelastic components,

$$D_{ij} = D_{ij}^* + D_{ij}^p, \quad W_{ij} = W_{ij}^* + W_{ij}^p, \quad (2.4a, b)$$

where the superscript $*$ denotes the elastic part, which includes the elastic lattice distortion as part of D_{ij}^* , and rigid body spin as part of W_{ij}^* . The superscript p denotes the plastic

component. The inelastic parts in (2.4) are defined in terms of the crystallographic slip rates as

$$D_{ij}^p = \sum_{\alpha} P_{ij}^{(\alpha)} \dot{\gamma}^{(\alpha)}, \quad W_{ij}^p = \sum_{\alpha} \omega_{ij}^{(\alpha)} \dot{\gamma}^{(\alpha)}, \quad (2.5a, b)$$

and α is summed over all slip systems. In the current configuration, $P_{ij}^{(\alpha)}$ is the symmetric component of the Schmid tensor and $\omega_{ij}^{(\alpha)}$ is the anti-symmetric part of the Schmid tensor given by

$$P_{ij}^{(\alpha)} = \frac{1}{2} (s_i^{(\alpha)} n_j^{(\alpha)} + s_j^{(\alpha)} n_i^{(\alpha)}), \quad \omega_{ij}^{(\alpha)} = \frac{1}{2} (s_i^{(\alpha)} n_j^{(\alpha)} - s_j^{(\alpha)} n_i^{(\alpha)}). \quad (2.6a, b)$$

As a measure of plastic strain, the effective plastic shear slip is calculated from the plastic deformation rate tensor as

$$\gamma_{eff} = \frac{2}{3} \int \sqrt{D_{ij}^p D_{ij}^p} dt. \quad (2.7)$$

In this formulation, the objective stress rate is co-rotational with the material element, and is given by

$$\sigma_{ij}^{\Delta} = L_{ijkl} \left(D_{kl} - D_{kl}^p \right) - W_{ij}^* \sigma_{kj} - W_{jk}^p \sigma_{ki}. \quad (2.8)$$

L_{ijkl} is the forth-order elastic modulus tensor of the crystal defined by

$$L_{ijkl} = G(\delta_{ik} \delta_{jl} + \delta_{jk} \delta_{il}) + \lambda \delta_{ij} \delta_{kl}. \quad (2.9)$$

G is the shear modulus. Combining both the Cauchy stress rate co-rotational with the elastic lattice distortion and the Jaumann stress rate co-rotational with the material element results in this objective stress rate.

For each slip system, the rate-dependent constitutive formulation is described as a power law relation for strain rates below a critical value $\dot{\gamma}_{critical}$ as

$$\dot{\gamma}^{(\alpha)} = \dot{\gamma}_{ref}^{(\alpha)} \left[\frac{\tau^{(\alpha)}}{\tau_{ref}^{(\alpha)}} \right] \left[\left[\frac{\tau^{(\alpha)}}{\tau_{ref}^{(\alpha)}} \right] \right]^{\frac{1}{m}-1} \quad (\text{no sum on } \alpha). \quad (2.10)$$

$\dot{\gamma}_{ref}^{(\alpha)}$ is the reference shear strain rate corresponding to a reference shear stress $\tau_{ref}^{(\alpha)}$, and m is the material rate sensitivity parameter. The reference stress is a modification of the classical forms that relate reference stress to immobile dislocation-density, ρ_{im} , as

$$\tau_{ref}^{(\alpha)} = \left(\tau_y^{(\alpha)} + G \sum_{\beta=1}^{nss} b^{(\beta)} \sqrt{a_{\alpha\beta} \rho_{ij}^{(\beta)}} \right) \left(\frac{T}{T_0} \right)^{-\xi}, \quad (2.11)$$

where $\tau_y^{(\alpha)}$ is the static yield stress on slip system α , nss is the number of active slip systems, $b^{(\beta)}$ is the magnitude of the Burgers vector, and the coefficients $a_{\alpha\beta}$ are Taylor coefficients relating the strength of interactions between slip systems. T is the temperature, T_0 is the reference temperature, and ξ is the thermal softening exponent.

2.2 Dislocation Density Evolution

It is assumed that for a given deformed state of the material that the total dislocation-density, $\rho^{(\alpha)}$, can be additively decomposed into mobile, $\rho_m^{(\alpha)}$, and immobile, $\rho_{im}^{(\alpha)}$, densities as

$$\rho^{(\alpha)} = \rho_{im}^{(\alpha)} + \rho_m^{(\alpha)}. \quad (2.12)$$

During an increment of strain on a slip system, a mobile dislocation-density rate is generated and an immobile dislocation-density rate is annihilated. Furthermore, the mobile and immobile dislocation-density rates can be coupled through the formation and destruction of junctions as the stored immobile dislocations act as obstacles for evolving mobile dislocations. This defect behavior is coupled, and leads to the differential equations governing dislocation density evolution,

$$\dot{\rho}_m^{(\alpha)} = \dot{\rho}_{generation}^{(\alpha)} - \dot{\rho}_{interaction-}^{(\alpha)}, \quad (2.13a)$$

$$\dot{\rho}_{im}^{(\alpha)} = \dot{\rho}_{interaction+}^{(\alpha)} - \dot{\rho}_{annihilation}^{(\alpha)}. \quad (2.13b)$$

The dislocation density evolution formulation used here is further explained in Shanthraj & Zikry (2011), but is outlined here. Dislocation generation is governed by the distance traveled by an emitted dislocation, y_{back} , from a source with dislocation-density, ρ_{source} . The Frank Read mechanism is employed, since both y_{back} and ρ_{source} are related to the spacing of immobile forest obstacles. The generation rate is then determined by the average velocity of mobile dislocations, $v^{(\alpha)}$, as

$$\dot{\rho}_{generation} = \rho_{source}^{(\alpha)} \frac{v^{(\alpha)}}{y_{back}}. \quad (2.14)$$

The Orowan equation,

$$\dot{\gamma}^{(\alpha)} = \rho_m^{(\alpha)} b^{(\alpha)} v^{(\alpha)}, \quad (2.15)$$

allows the generation rate to be recast as

$$\dot{\rho}_{generation} = \frac{\phi \sum_{\beta} \sqrt{\rho_{im}^{(\beta)}}}{b^{(\alpha)}} \left(\frac{\rho_{im}^{(\alpha)}}{\rho_m^{(\alpha)}} \right) \dot{\gamma}^{(\alpha)}, \quad (2.16)$$

where ϕ is a geometric parameter and $b^{(\alpha)}$ is the magnitude of the Burger's vector on slip system α .

Interaction between dislocations can occur between slip systems, causing junction formation and the immobilization of mobile dislocation segments. How often mobile dislocation-densities of slip system α interact with immobile dislocation densities on slip system β are defined by the frequencies,

$$\rho_m^{(\alpha)} \rho_m^{(\beta)} v^{(\alpha\beta)}, \quad (2.17a)$$

$$\rho_m^{(\alpha)} \rho_{im}^{(\beta)} v^{(\alpha)}, \quad (2.17b)$$

where $v^{(\alpha\beta)}$ is the relative velocity between slip systems and is defined by the Orowan equation (2.15) as,

$$v^{(\alpha\beta)} = \frac{\dot{\gamma}^{(\alpha)}}{\rho_m^{(\alpha)} b^{(\alpha)}} + \frac{\dot{\gamma}^{(\beta)}}{\rho_m^{(\beta)} b^{(\beta)}}. \quad (2.18)$$

Only a fraction of the junctions between slip systems are stable, f_0 , and the length of the junction formed is assumed to be proportional to the spacing of immobile dislocations as

$$l_c = \frac{1}{\sum_{\beta} \sqrt{\rho_{im}^{(\beta)}}}. \quad (2.19)$$

Rearranging (2.17-2.19) gives the immobilization rates for dislocation-densities on slip system α due to mobile (2.20a) and immobile (2.20b) dislocation-densities on slip system β as follows:

$$f_0 \rho_m^{(\alpha)} \rho_m^{(\beta)} l_c \mathbf{v}^{(\alpha\beta)}, \quad (2.20a)$$

$$f_0 \rho_m^{(\alpha)} \rho_{im}^{(\beta)} l_c \mathbf{v}^{(\alpha)}. \quad (2.20a)$$

The total rate of immobilization of mobile dislocation-densities on slip system α is therefore

$$\dot{\rho}_{interaction-}^{(\alpha)} = f_0 \sum_{\beta} \left(\rho_m^{(\beta)} l_c \frac{\dot{\gamma}^{(\alpha)}}{b^{(\alpha)}} + \rho_m^{(\alpha)} l_c \frac{\dot{\gamma}^{(\beta)}}{b^{(\beta)}} \right) + f_0 \sum_{\beta} \rho_{im}^{(\beta)} l_c \frac{\dot{\gamma}^{(\alpha)}}{b^{(\alpha)}}. \quad (2.21)$$

Because immobile dislocation-densities may also be created as a result of the formation of immobile junctions, the interaction term in (2.13b) must also be considered. Frank's rule is used to determine if immobile junction formation due to dislocation interaction is energetically favorable. A dislocation density interaction tensor for junction formation on slip system α due to interaction of slip systems β and γ is defined as

$$n_{\alpha}^{\beta\gamma} = \begin{cases} 1 & \text{if } \mu b^{(\alpha)2} < \mu b^{(\beta)2} + \mu b^{(\gamma)2} \text{ and } b^{(\alpha)} = b^{(\beta)} + b^{(\gamma)} \\ 0 & \text{otherwise} \end{cases}. \quad (2.22)$$

The rates of junction formation on slip system α are then defined as

$$n_{\alpha}^{\beta\gamma} f_0 \rho_m^{(\beta)} \rho_m^{(\gamma)} l_c \mathbf{v}^{(\beta\gamma)}, \quad (2.23a)$$

$$n_{\alpha}^{\beta\gamma} f_{\beta\gamma} l_c \left(\rho_m^{(\beta)} \rho_{im}^{(\gamma)} \mathbf{v}^{(\beta)} + \rho_m^{(\gamma)} \rho_{im}^{(\beta)} \mathbf{v}^{(\gamma)} \right), \quad (2.23b)$$

for mobile/mobile (2.23a) and mobile/immobile (2.23b) interactions. The total addition of immobile dislocation-densities due to interactions then becomes

$$\dot{\rho}_{interaction+}^{(\alpha)} = f_0 \sum_{\beta,\gamma} \left(\rho_m^{(\beta)} l_c \frac{\dot{\gamma}^{(\gamma)}}{b^{(\gamma)}} + \rho_m^{(\gamma)} l_c \frac{\dot{\gamma}^{(\beta)}}{b^{(\beta)}} \right) + f_0 \sum_{\beta,\gamma} \left(\rho_{im}^{(\beta)} l_c \frac{\dot{\gamma}^{(\gamma)}}{b^{(\gamma)}} + \rho_{im}^{(\gamma)} l_c \frac{\dot{\gamma}^{(\beta)}}{b^{(\beta)}} \right). \quad (2.24)$$

The six energetically favorable interactions: self interaction, co-linear interaction, co-planar interaction, Lomer locks, glissile junctions, and Hirth locks are used to create f.c.c. crystals' interaction tensor, and are summarized in Table 2.1 (Kubin, Devincere, & Hoc, 2008).

Dislocation-density annihilation due to recovery is modeled using an Arrhenius relationship (Vegge, Rasmussen, Leffers, Pedersen, & Jacobsen, 2000) as

$$\dot{\rho}_{annihilation}^{(\alpha)} = \nu^{(\alpha)} e^{\left(\frac{-H}{kT}\right)}. \quad (2.25)$$

The frequency with which immobile dislocations are intersected by mobile dislocations on other slip systems is related to the attempt frequency, $\nu^{(\alpha)}$, as

$$\nu^{(\alpha)} = f_0 \sum_{\beta} \rho_{im}^{(\alpha)} l_c \frac{\dot{\gamma}^{(\beta)}}{b^{(\beta)}}. \quad (2.26)$$

The activation enthalpy, H , is related to the immobile dislocation density and saturation density, ρ_s , as

$$H = H_0 \left(1 - \sqrt{\frac{\rho_{im}^{(\alpha)}}{\rho_s}} \right). \quad (2.27)$$

The annihilation rate of dislocation-densities on slip system α then becomes

$$\dot{\rho}_{annihilation}^{(\alpha)} = \left(f_0 \sum_{\beta} \rho_{im}^{(\alpha)} l_c \frac{\dot{\gamma}^{(\beta)}}{b^{(\beta)}} \right) e^{\left(\frac{-H_0 \left(1 - \sqrt{\frac{\rho_{im}^{(\alpha)}}{\rho_s}} \right)}{kT} \right)}. \quad (2.28)$$

The generation, interaction, and annihilation rates are then substituted into equations (2.13) to obtain a coupled nonlinear set of evolutionary equations for the dislocation densities. The evolutionary equations can be expressed as

$$\frac{d\rho_m^\alpha}{dt} = |\dot{\gamma}^{(\alpha)}| \left(\frac{g_{sour}^\alpha}{b^2} \left(\frac{\rho_{im}^\alpha}{\rho_m^\alpha} \right) - g_{mter}^\alpha - \rho_m^\alpha - \frac{g_{immob-}^\alpha}{b} \sqrt{\rho_{im}^\alpha} \right), \quad (2.29a)$$

$$\frac{d\rho_{im}^\alpha}{dt} = |\dot{\gamma}^{(\alpha)}| \left(g_{mter}^\alpha + \rho_m^\alpha - \frac{g_{immob+}^\alpha}{b} \sqrt{\rho_{im}^\alpha} - g_{recov}^\alpha \rho_{im}^\alpha \right), \quad (2.29b)$$

to delineate the dislocation activities such as generation, interaction, immobilization, and annihilation (Zikry & Kao, 1996). The coefficients, not known *a priori*, are summarized in Table 2.2 and are functions of the deformation mode. The dislocation activity is coupled to the stress response through the Taylor relationship (2.11).

2.3 DNA and Ligands: Isotropic Elasticity

Modeling and experimental investigations have shown that double helices below approximately 40 base pairs, known as the persistence length, display isotropic, rigid deformation (Bensimon, Simon, Croquette, & Bensimon, 1995; Olson, Marky, Jernigan, & Zhurkin, 1993). Consequently, the DNA and the ligand deformations were modeled using isotropic finite elasticity. The elastic formulation was based on a hypoelastic formulation of

equations 2.8a-b. This formulation is in terms of the elastic deformation strain-rate tensor, and it, therefore, accounts for finite elastic strains with the appropriate stress rate objectivity.

REFERENCES – Chapter 2

- Ashmawi, W. M., & Zikry, M. A. (2002). Prediction of grain-boundary interfacial mechanisms in polycrystalline materials. *Journal of Engineering Materials and Technology: Transactions of the ASME*, 124, 88-96.
- Auyeung, E., Macfarlane, R. J., Choi, C. J., Cutler, J. I., & Mirkin, C. A. (2012). Transitioning DNA-engineered nanoparticle superlattices from solution to the solid state. *Advanced Materials*, 24, 5181-5186.
- Bensimon, D., Simon, A. J., Croquette, V., & Bensimon, A. (1995). Stretching DNA with a receding meniscus: Experiments and models. *Physical Review Letters*, 74 (23), 4754-4757.
- Dickerson, R. E., Drew, H. R., Conner, B. N., Wing, R. M., Fratini, A. V., & Kopka, M. L. (1982). The anatomy of A-, B-, and Z-DNA. *Science*, 216 (4545), 475-485.
- Elghanian, R., Storhoff, J. J., Mucic, R. C., Letsinger, R. L., & Mirkin, C. A. (1997). Selective colorimetric detection of polynucleotides on the distance-dependent optical properties of gold nanoparticles. *Science*, 277 (5329), 1078-1081.
- El-Sayed, I. H., Huang, X., & El-Sayed, M. A. (2006). Selective laser photo-thermal therapy of epithelial carcinoma using anti-EGFR antibody conjugated gold nanoparticles. *Cancer Letters*, 239 (1), 129-135.
- Huang, X., Jain, P. K., El-Sayed, I. H., & El-Sayed, M. A. (2008). Plasmonic photothermal therapy (PPTT) using gold nanoparticles. *Lasers in Medical Science*, 23 (3), 217-228.
- Kim, Y., Johnson, R. C., & Hupp, J. T. (2001). Gold nanoparticle-based sensing of "spectroscopically silent" heavy metal ions. *Nano Letters*, 1 (4), 165-167.
- Kubin, L., Devincere, B., & Hoc, T. (2008). Modeling dislocation storage rates and mean free paths in face-centered cubic crystals. *Acta Materialia*, 56, 6040-6049.
- Olson, W. K., Marky, N. L., Jernigan, R. L., & Zhurkin, V. B. (1993). Influence of fluctuations on DNA curvature. A comparison of flexible and static wedge models of intrinsically bent DNA. *Journal of Molecular Biology*, 252, 530-554.
- Orsini, V. C., & Zikry, M. A. (2001). Void growth and interaction in crystalline materials. *International Journal of Plasticity*, 17, 1393-1417.
- Qian, X., Zhou, X., & Nie, S. (2008). Surface-enhanced Raman nanoparticle beacons based on bioconjugated gold nanocrystals and long range plasmonic coupling. *Journal of the American Chemical Society*, 130 (45), 14934-14935.

- Shanthraj, P., & Zikry, M. A. (2011). Dislocation density evolution and interactions in crystalline materials. *Acta Materialia*, 59, 7695-7702.
- Sonnichsen, C., Reinhard, B. M., Liphardt, J., & Alivisatos, A. P. (2005). A molecular ruler based on plasmon coupling of single gold and silver nanoparticles. *Nature Biotechnology*, 23 (6), 741-745.
- Storhoff, J. J., Lazarides, A. A., Mucic, R. A., Mirkin, C. A., Letsinger, R. L., & Schatz, G. C. (2000). What controls the optical properties of DNA-linked gold nanoparticle assemblies. *Journal of the American Chemical Society*, 122, 4640-4650.
- Tkachenko, A. G., Xie, H., Coleman, D., Glomm, W., Joseph, R., Anderson, M. F., *et al.* (2003). Multifunctional gold nanoparticle-peptide complexes for nuclear targeting. *Journal of the American Chemical Society*, 125 (16), 4700-4701.
- Vegge, T., Rasmussen, T., Leffers, T., Pedersen, O. B., & Jacobsen, K. W. (2000). Determination of the of rate cross slip of screw dislocations. *Physical Review Letters*, 85 (18), 3866-3869.
- Winfrey, E., Liu, F., Wenzler, L. A., & Seeman, N. C. (1998). Design and self-assembly of two-dimensional DNA crystals. *Nature*, 394 (6693), 539-544.
- Zikry, M. A., & Kao, M. (1996). Inelastic microstructural failure mechanisms in crystalline materials with high angle grain boundaries. *Journal of the Mechanics and Physics of Solids*, 44 (11), 1765-1798.

Table 2.1: Summary of interactions and coefficient values in an f.c.c. crystal.

Interaction type	Dissipation ($\propto a_{ij}^{1/2}$)	a_{ij}	a_{ij} from (Kubin <i>et al.</i>, 2008)
Self	$2kGb^2$	0.6	-
Co-linear	$2kGb^2$	0.6	0.625
Lomer lock	kGb^2	0.15	0.122
Glissile junction	kGb^2	0.15	0.137
Co-planar	kGb^2	0.15	0.122
Hirth lock	0	0.00	0.045

Table 2.2: g-coefficients for dislocation-density evolution equations.

g Coefficients	Expression
g_{sour}^{α}	$b^{\alpha} \phi \sum_{\beta} \sqrt{\rho_{im}^{\beta}}$
g_{mter-}^{α}	$l_c f_0 \sum_{\beta} \left[\frac{\rho_m^{\beta}}{\rho_m^{\alpha} b^{\alpha}} + \frac{\dot{\gamma}^{\beta}}{\dot{\gamma}^{\alpha} b^{\beta}} \right]$
g_{immob-}^{α}	$\frac{l_c f_0}{\sqrt{\rho_{im}^{\alpha}}} \sum_{\beta} \rho_{im}^{\beta}$
g_{mter+}^{α}	$\frac{l_c f_0}{\dot{\gamma}^{\alpha} \rho_m^{\alpha}} \sum_{\beta, \gamma} n_{\alpha}^{\beta \gamma} \left[\frac{\rho_m^{\gamma} \dot{\gamma}^{\beta}}{b^{\beta}} + \frac{\rho_m^{\beta} \dot{\gamma}^{\gamma}}{b^{\gamma}} \right]$
g_{immob+}^{α}	$\frac{l_c f_0}{\dot{\gamma}^{\alpha} \sqrt{\rho_{im}^{\alpha}}} \sum_{\beta} n_{\alpha}^{\beta \gamma} \rho_{im}^{\gamma} \dot{\gamma}^{\beta}$
$g_{re cov}^{\alpha}$	$\frac{l_c f_0}{\dot{\gamma}^{\alpha}} \left(\sum_{\beta} \frac{\dot{\gamma}^{\beta}}{b^{\beta}} \right) e^{\left(\frac{-H_0 \left(1 - \sqrt{\frac{\rho_{im}^{\alpha}}{\rho_s}} \right)}{kT} \right)}$

CHAPTER 3: Numerical Methods

Equations in Chapter 2 are related to the derivation and updating of the state of stress in all modeled materials. First, though, the elastic and plastic components of the velocity gradient, V_{ij} , must be obtained (2.3a,b). A specialized finite element method has been implemented to determine V_{ij} , and it is outlined below.

3.1 Total Velocity Gradient

The total velocity gradient, V_{ij} , can be obtained using a specialized implicit finite element method, and from it D_{ij} , the deformation rate tensor, may be derived (2.3a,b). In this dissertation, all analyses were quasi-static, and an incremental approach using a quasi-Newton solution of the static equilibrium equations with BFGS iteration was utilized to find the displacements. The deformation calculated using finite element analysis was then used to calculate the total velocity gradient, V_{ij} , using (2.1), and then the total deformation rate tensor and the spin tensor, W_{ij} could be calculated at each load level.

Q4 quadrilateral elements were used with reduced one point Gauss quadrature to avoid numerical locking due to incompressibility pressure constraints. This element was chosen primarily for its significant reduction in computation time. However, reduced one point integration can lead to zero-energy modes in bending and so stiffness-based hourglass control was implemented to suppress numerical instabilities that can be triggered by localized plastic slip (see, for instance, Belyschko, Liu, & Moran, 2000; Lee & Zikry, 2014). For more detailed information on stiffness-based hourglass control, see Flanagan & Belytschko, (1981), but a brief summary is included here.

For the Q4 elements with one-point integration, an hourglass base vector is used to describe hourglass modes as follows:

$$\mathbf{h}^T = [1 \ -1 \ 1 \ -1]. \quad (3.1)$$

When defined in the corotational frame, the hourglass shape vector, γ_i , is orthogonal to the linear velocity field,

$$\gamma_i = \frac{1}{4} [\mathbf{h} - (\mathbf{h}^T \mathbf{x}_i) \mathbf{b}_i], \quad i = x, y, \quad (3.2)$$

where \mathbf{b}_i are shape function derivatives and \mathbf{x}_i are the nodal coordinates. Also given in the corotational frame are the generalized hourglass velocity strains, \dot{q} in terms of the nodal velocities, \mathbf{v}_i ,

$$\dot{q}_x = \gamma^T \mathbf{v}_x \quad (3.3a)$$

$$\dot{q}_y = \gamma^T \mathbf{v}_y. \quad (3.3b)$$

The hourglass stress rates are found in the usual way, with

$$\dot{Q}_x = C^Q \dot{q}_x \quad (3.4a)$$

$$\dot{Q}_y = C^Q \dot{q}_y, \quad (3.4b)$$

and the coefficient C^Q given by

$$C^Q = \frac{1}{2} \alpha_s c^2 \rho A \mathbf{b}_i^T \mathbf{b}_i, \quad (3.5)$$

where α_s is the input parameter, c is the shear wavespeed and ρ is the density of the material. The stress rates are then integrated, multiplied by the area of the element, A , and used to augment the force vector through a stabilization force,

$$\mathbf{f}^{stab} = A \begin{Bmatrix} Q_x \gamma \\ Q_y \gamma \end{Bmatrix}, \quad (3.6)$$

while a stabilizing hourglass stiffness term is added to the elemental stiffness matrix, \mathbf{K}_e , as

$$\mathbf{K}_e = \mathbf{K}_{e,pl} + C^Q A \begin{bmatrix} \gamma \gamma^T & \gamma \gamma^T \\ \gamma \gamma^T & \gamma \gamma^T \end{bmatrix}. \quad (3.7)$$

For plastic elements the wavespeed is lower, and an effective modulus is needed

$$\hat{G} = \frac{1}{2} \frac{\hat{\sigma}_{ij}^e D_{ij}}{D_{ij} D_{ij}} \quad (3.8a)$$

$$\hat{\lambda} = \hat{\kappa} - \frac{2}{3} \hat{G} \quad (3.8b)$$

$$c = \sqrt{\frac{(\hat{\lambda} + 2\hat{G})}{\rho}} \quad (3.8c)$$

3.2 Plastic Velocity Gradient

For each slip plane, the objective stress rate from Chapter 2 is coupled with the time derivative of the stress to obtain the resolved shear stress as

$$\dot{\tau}^{(\alpha)} = \frac{d}{dt} \left(P_{ij}^{(\alpha)} \sigma_{ij} \right). \quad (3.9)$$

From (2.8) it may be derived such that

$$\dot{\boldsymbol{\tau}}^{(\alpha)} = L_{ijkl} P_{ij}^{(\alpha)} D_{kl}^e. \quad (3.10)$$

Using the formulations presented in Chapter 2, (3.10) may be expanded,

$$\dot{\boldsymbol{\tau}}^{(\alpha)} = 2\mu P_{ij}^{(\alpha)} \left[D_{ij} - \sum_{\xi=1, n_{ss}} P_{ij}^{(\xi)} \dot{\gamma}_{ref}^{(\xi)} \left(\frac{\boldsymbol{\tau}^{(\xi)}}{\boldsymbol{\tau}_{ref}^{(\xi)}} \right)^{\frac{1}{m}} \right], \quad (3.11)$$

and the plastic velocity gradient may then be found using the plastic deformation rate tensor, spin rate tensor, slip rates, and the Schmid tensor.

REFERENCES – Chapter 3

- Belyschko, T., Liu, W. K., & Moran, B. (2000). *Nonlinear Finite Elements for Continua and Structures*. Chichester, England: John Wiley & Sons, Ltd.
- Flanagan, D. P., & Belytschko, T. (1981). A iniform strain hexahedron and quadrilateral with orthogonal hourglass Control. *International Journal for Numerical Methods in Engineering*, 17, 679-706.
- Lee, W. M. & Zikry, M. A. (2014), Microstructurally induced computational and material instabilities, *International Journal of Plasticity*, 52, 95-104.

CHAPTER 4: Mechanical Strength and Stability of Two-particle DNA-modified Gold Nanoparticle Systems

Small AuNP-DNA systems, like those used in drug delivery and gene therapies, consist of few AuNPs capped with oligonucleotides (Uhlmann & Peyman, 1990; Rosi, Giljohann, Thaxton, Lytton-Jean, Han, & Mirkin, 2006). These subsets of larger systems may be easily modeled, and general principles concerning the mechanical strength and stability of AuNP-DNA systems may be established by investigating their response to loading. In order to create a foundation understanding of AuNPs modified with oligonucleotides, small systems composed of two nanoparticles with a single ligand-DNA tether was modeled in plane strain displacement loading. Furthermore, systems have been optimized by quantitatively comparing the mechanical responses of AuNP-DNA with various characteristics readily available during experimental development, like DNA strand length and AuNP size. Guidelines for improved stability of the systems have therefore been provided.

By using the constitutive formulations and finite element method described in Chapters 2-3, the limitations and possible failure mechanisms of AuNP-DNA systems has been addressed while simultaneously optimizing the response of the system. In order to do this, different AuNP morphologies and texture, DNA lengths, and loading conditions including a system with 13.5 nm pentagonally twinned AuNPs with 6 nm DNA, a system with 20 nm circular AuNPs with 6 nm DNA, a system with 20 nm cuboctahedron AuNPs with 6 nm DNA, 12 nm DNA, and 18 nm DNA, and a system with 20 nm textured cuboctahedrons have been investigated. The analyses indicate that the systems' stability and strength are mainly affected by the interfacial stress and dislocation-densities at the interface of the AuNPs with

the ligand. The systems that had the best mechanical stability and strengthening results were those with the shortest strands of DNA and for circular and cuboctahedron AuNPs. Shorter lengths of DNA reduced the stress gradients across the DNA-ligand interface, thereby reducing the possibility of failure. Circular and cuboctahedral nanoparticles provided regions of concentrated dislocation-densities just behind the ligand attachment points in the AuNPs, which resulted in the strengthening of the different particles.

4.1 Approach

The multiple slip dislocation-density based crystal plasticity and the specialized finite element algorithm discussed in Chapter 2 and 3 were used to investigate the mechanical stability of various heterogeneous AuNP-DNA nanosystems. The effects of different DNA lengths, AuNP morphologies textures, and plane strain uniaxial and biaxial loading conditions were investigated to assess system behavior and strength. In the case of textured AuNPs, Euler angle distributions are used to represent faceting in the nanoparticles (Figure 4.1). The angles α , β , and γ were calculated corresponding to the facets' respective surface orientations, and the y-axis was assumed to be [010].

A representative system with two AuNPs attached together with a ligand-DNA-ligand tether and a matrix material for load transfer to the nanoparticles and the DNA is shown in Figure 4.2. The assemblies were approximately sized at $50 \text{ nm} \times 25 \text{ nm}$ and were varied by 1 – 15 nm as a function of the different shapes of the AuNPs and lengths of the DNA. Symmetry boundary conditions were used and compressive plane strain displacement loading was applied along the appropriate axes.

As AuNPs are grown, surface tensions can fluctuate with increased diameter and the lowest energy AuNP morphology differs with length scale and growth mechanism (Yacaman *et al.*, 2001). To investigate different Au nanoscale morphologies, 13.5 nm pentagonally twinned particles and 20 nm f.c.c. cuboctahedral and circular nanoparticles were modeled. The mechanical properties of the different components of the heterogeneous system are given in Table 4.1.

The DNA dimensions and elastic properties are based on experimental investigations and modeled with different numbers of base pairs to examine how length variations would affect AuNP-DNA strength. The DNA is assumed to be double stranded, which would be representative of full hybridization between the single-stranded oligonucleotides and single-stranded components of staple DNA strands. Double-stranded DNA moduli are nucleotide sequence dependent (Olson & Zhurkin, 2000). Hence, assuming the DNA as an isotropic elastic material (Table 4.1), and that the sequences would not have intrinsic curvatures, are physically realistic. The DNA were assumed to have a rise per base pair length of approximately 0.26 nm and a 2 nm diameter, see for example, the experimental investigations of Macfarlane, *et al.* (2011). The stability of the system was analyzed by utilizing 24 (6 nm), 48 (12 nm), and 72 (18 nm) base pair DNA.

Gold and sulfur form a strong chemical bond, and therefore, it was assumed that the ligand is an alkanethiol. The AuNP-DNA system was modeled with one ligand-DNA-ligand assembly between each nanoparticle. The dimensions of the ligand material were chosen such that they encompassed each of the bonds in the alkanethiol (Figure 4.2). Isotropic elasticity was also used to represent the ligand deformation and its properties (Table 4.1).

4.2 Results

4.2.1 Non-textured Cuboctahedron NPs with 6 nm DNA

Figure 4.3 shows the normal and lateral stresses and pressure distributions (normalized by the yield stress of the gold nanoparticles) for the 20 nm cuboctahedron f.c.c. nanoparticles with approximately 6 nm long DNA in plane strain compression at a nominal strain of 2%. The loading is in the [010] direction. The DNA has the lowest stresses within the system due to its low elastic modulus, and the highest stresses are within the AuNPs near the ligand attachment. The large stress mismatches and the DNA's negative Poisson's ratio have resulted in the lateral expansion at the ligand-DNA attachment.

The high stresses that have occurred in the AuNPs, specifically at the attachment regions of the ligands, also resulted in high stress gradients and instabilities at the attachment points, as shown in the insets of Figure 4.3. The AuNPs were assumed as non-textured, meaning both cuboctahedron particles were treated as crystals with [010] aligned to the uniaxial displacement loading axis. The differences in stresses across the AuNP-ligand interface were as high as 5 times the yield stress of Au. The spatial distribution of the gradients indicated that the AuNP-ligand attachment site is the critical region in determining the stability of the entire AuNP-DNA system, since detachment at this point would weaken the entire system. Therefore, system conformations that can lower stress gradients between the AuNPs and ligands would be desirable.

There was significant dislocation-density accumulation around the ligand attachment sites in the AuNPs (Figure 4.4). This accumulation can provide strength, since increases in the dislocation-density can result in increases in the reference stress. The most active slip

systems for the AuNPs were the (1-11)[011] and (-1-11)[011] systems, and their immobile and mobile dislocation-densities and slip rates are shown in Figures 4.4a-c. The shear slip corresponding to the total accumulated slip due to all active slip systems is shown in Figure 4.4d, and the maximum shear strain is 2.6%. As shown in the insets of Figure 4.4, the plasticity was localized at the ligand attachment site, with maximum immobile dislocations 4.5 times the initial immobile dislocation-densities, and mobile dislocation-densities that were 35 times the initial values. As noted earlier, these dislocation-densities resulted in the hardening and strengthening of the AuNPs (cf. eq. 2.11).

4.2.2 AuNP Morphology

The localized stresses and plasticity in the AuNPs and high stress gradients across the ligand-AuNP interface indicate the critical nature of this region for the mechanical stability of the entire AuNP-DNA system. The effects of different AuNP morphologies were, therefore, examined to clearly delineate how this region affects stability in systems with those different morphologies. At the nanoscale, AuNPs exist in several morphologies depending on their growth and ambient conditions. Therefore, an analysis of AuNP-DNA systems using various nanoparticle shapes can determine how each system can be optimized for mechanical stability. For small particles with diameters that are approximately 5 nm, the most energetically favorable morphology is a decahedral, fivefold twin, consisting of ten $\{111\}$ twinned facets. Because the surface orientation consists only of $\{111\}$ twinned crystals, an angular gap of approximately 7.5° is needed to make the particle truly space filling (Marks 1994). In crystals, this required gap is addressed by inducing internal strains into the particle, which in turn give rise to structural defects (Elechiguerra, *et al.*, 2006). As

particle size increases, multifaceted f.c.c. particles, like the cuboctahedron, would be the dominant morphology due to their energetic stability at longer length scales (Elechiguerra, *et al.*, 2006). Furthermore, particles with many facets are often described as spherical or circular because of the presence of a multitude of facets, which essentially round out the particle. We, therefore, examined the mechanical stability of three AuNP morphologies: 13.5 nm pentagonally twinned, 20 nm f.c.c. cuboctahedral, and 20 nm round particles. The AuNP-DNA nanosystems consisted of approximately 6 nm DNA, a matrix-border of approximately 1 nm, and each particle was oriented in the same crystallographic orientation with [010] aligned to the loading axis. In this way, valid comparisons could be made with the previous analysis.

Figure 4.5 shows the normalized normal stress for the pentagonal and circular morphologies. The buildup of stress and high stress gradients can be seen at the attachment region for all three cases. The pentagonal nanoparticles had lower normal stresses in comparison with the other morphologies, but the lateral stresses were lower than the other cases by approximately 9.7% (Figure 4.6a). This can be due to the ligand attachment being on the long edge of a facet rather than being at the corner. The circular particles had similar stresses in comparison with the cuboctahedrons, and the stress gradients were approximately the same between the three systems, despite the lower lateral stresses in the pentagonal particles.

The two most active slip systems for the circular and the pentagonal crystals, (1-11)[011] and (-1-11)[011], were the same for the cuboctahedral particles. Between the three morphologies, the pentagonally shaped nanoparticles had the highest immobile and mobile

dislocation-densities with 4.9 times the initial immobile dislocation-density and 41 times the initial mobile dislocation-density. The circular particles had 2% less shear slip and dislocation-density accumulation, while the cuboctahedrons had 7% less shear strain than pentagonal crystals (Figure 4.7a,b). The total accumulated shear slip for pentagonal particles was 2.8%.

Each nanoparticle, despite its shape, had significant stress and mobile and immobile dislocation-density accumulations at the ligand attachment region. Nanoparticles are generally capped with oligonucleotides thereby reducing free surfaces in the particles. Any dislocation-density buildup would then be restricted, effectively hardening and strengthening the AuNP in this critical region.

4.2.3 AuNP Orientation and Texture

To further understand the differences in stress and plasticity of the various morphologies for the system, AuNPs and DNA were modeled so that the geometric effects of the cuboctahedron particles were delineated. In this system, the ligand was attached along one side at a corner of the particle, and on the other side it was attached at the middle of a facet by rotating the particle 90° (Figure 4.8). In general, the highest stresses and shear slip occurred at the binding locations of the corner-attached ligand in the right-hand particle. This substantiates that the lower stresses pertaining to the pentagonal nanoparticles are due to the ligand attachment site, because the lateral stresses are distributed along the entire facet, not just at the corner near the ligand.

To investigate the surface orientation and texture of the facets, each facet of the cuboctahedron particles were subdivided into regions with different Euler angles, such that it

could be compared with the non-textured results. Because the cuboctahedron nanoparticle is f.c.c., the $\{111\}$ and $\{100\}$ surface orientations were computed (Figure 4.1). The normal and lateral stresses were within 5% of the non-textured AuNPs; the plasticity, however, was significantly different. Texturizing the particles resulted in a substantial increase in the maximum dislocation-densities by approximately 32% in comparison with the non-textured case. New regions of high dislocation-density for the most active slip system (111) $[-1-10]$ occurred at the outer corners of the AuNPs on two facets (Figure 4.9a,b), and the highest immobile dislocation-densities were 6 times the initial values. The mobile dislocation-densities were 54 times the initial values, while the shear slip had a maximum value of 3.23%. Slip system (111) $[0-1-1]$ was the second most active slip system (Figure 4.9c), and similar to the non-textured particle case, plasticity accumulated adjacent to the ligand-Au binding site. The most active slip system, (111) $[-1-10]$ (Figure 4.9d), had the most significant increase in plasticity of the textured system, and this plasticity was larger than the non-textured by approximately 21%. These extreme differences in plastic behavior sufficiently prove the importance of modeling nanoscale AuNPs as textured particles, not simple crystals or rigid shapes.

4.2.4. DNA Length

To investigate the effects of DNA length on the stability of AuNP-DNA systems, 6, 12, and 18 nm DNA, or 24, 48, and 72 base pairs, attached to textured cuboctahedron nanoparticles were compared. Figure 4.10 shows the effects of varying DNA lengths on normal stress. Compared with the 6 nm system (Figure 4.3a), the stresses for the longer DNA have increased by approximately 9% and the stress gradients were correspondingly

higher across the DNA-ligand interface. The plasticity in the AuNPs did not increase significantly in comparison with the 6 nm case. Hence, the longer the DNA, the more instabilities would be expected in the AuNP-DNA system at the ligand AuNP attachment region. This is due to the interrelated effects of dislocation strengthening, increased stresses, and higher stress gradients at material binding sites in systems with the longer DNA strands.

4.2.5 Biaxial Loading Condition

Because AuNP-DNA systems have potential in many different biomedical and sensing applications, the analysis was extended to investigate the effects of plane strain compressive biaxial displacement loading. Displacements were applied along the top and the right hand side of the load-transferring matrix (see Figure 4.2) for a system with textured cuboctahedron particles and 6 nm DNA. Figure 4.11 shows the increased normal stresses, at a nominal strain of 1.2% for the AuNPs (also compare to the uniaxial loading case Figure 4.3a, which is at 2% nominal strain). The stress gradients were lower for this loading case in comparison with the uniaxial loading case. The shear slip and dislocation-densities also were highly localized in comparison with the system without biaxial loading (Figure 4.9a). This is due to the lateral confinement of the biaxial loading. The localization of plasticity and higher stresses in combination with the relative decrease in stress gradients indicate AuNP-DNA systems can be strengthened in the case of biaxial compression. Hence, DNA-AuNP systems are more stable in applications requiring biaxial loading as opposed to uniaxial loading.

4.3 Conclusions

The potential for AuNP-DNA systems spans many different applications, and hence the necessity for assessing the mechanical behavior of these heterogeneous systems. By

examining local distributions of stresses, strains, and dislocation-densities, a framework has been developed that encompasses several factors affecting system strength: nanoparticle morphology, texture and orientation, DNA length, and different loading conditions. The cuboctahedron and circular particles had higher strengths in comparison with the pentagonally shaped nanoparticles, because of their inherent ability to sustain higher stresses while inducing plasticity within the AuNPs. This inelastic deformation contributes to both the toughness and the strength of the system. The placement of the pentagonal particles' ligand attachments along the edge of a particle facet rather than on the corner had a significant effect on these stress distributions. If the attachments were on the corner it would result in higher stresses and higher strength. Each nanoparticle's morphology resulted in similar stress gradients across the Au-ligand interface, thus indicating that stress gradients will be significant for all the examined systems. Differences in DNA length also affected interface stability, and the shorter DNA lengths had lower gradients and stresses with similar plasticity as systems with longer DNA. This indicates that shorter DNA in AuNP-DNA systems provides greater stability at the interfacial regions and strengthening within the nanoparticles.

The analyses have also indicated that substantial increases in plasticity occur for the textured cuboctahedral AuNPs in comparison for the non-textured ones. Furthermore, for plane strain biaxial compression the system was strengthened, as indicated in the increased values of plasticity and stresses at the critical ligand attachment sites in comparison with the uniaxial loading case. There were also lower stress gradients between the ligand and the DNA, which further indicates the beneficial characteristics of the constraining effects of

biaxial loading. The present analysis underscores how the heterogeneous characteristics of AuNP-DNA systems can be optimized for a system's desired mechanical response. Each system's constituents are application dependent, however, if one has options of DNA length, AuNP shape, and loading conditions within their application requirements, highly faceted f.c.c. AuNPs with DNA lengths approximately 6 nm in in biaxial loading conditions will provide desirable mechanical behavior.

REFERENCES – Chapter 4

- Bensimon, D., Simon, A. J., Croquette, V., & Bensimon, A. (1995). Stretching DNA with a receding meniscus: Experiments and models. *Physical Review Letters*, 74 (23), 4754-4757.
- Macfarlane, R. J., Lee, B., Jones, M. R., Harris, N., Schatz, G. C., & Mirkin, C. A. (2011). Nanoparticle Superlattice Engineering with DNA. *Science*, 334, 204-208.
- Manning, G. S. (1986). Correlation of polymer persistence length with Euler buckling fluctuations. *Physical Review A*, 34 (5), 4467-4468.
- Manning, G. S. (2012). Poisson's ratio for a polyelectrolyte. *Soft Matter*, 8, 9334-9337.
- Marks, L. D. (1994). Experimental studies of small particle structures. *Reports on Progress in Physics*, 57 (6), 603.
- Olson, W. K., & Zhurkin, V. B. (2000). Modeling DNA deformations. *Current Opinion in Structural Biology*, 10, 286-297.
- Rosi, N. L., Giljohann, D. A., Thaxton, C. S., Lytton-Jean, A. K., Han, M. S., & Mirkin, C. A. (2006). Oligonucleotide-modified gold nanoparticles for intracellular gene regulation. *Science*, 312, 1027-1030.
- Uhlmann, E., & Peyman, A. (1990). Antisense oligonucleotides - a new therapeutic principle. *Chemical Reviews*, 90 (4), 543-584.
- Yacaman, M. J., Ascencio, J. A., Liu, H. B., & Gardea-Torresday, J. (2001). Structure shape and stability of nanometric sized particles. *Journal of Vacuum Science and Technology B*, 19 (4), 1091-1103.

Table 4.1: Elastic properties of the AuNP-DNA components.

	AuNP	Ligand	DNA	Matrix
E (GPa)	70.0	0.35	0.11 ^a	17.5
ν	0.42	0.35	-0.70 ^b	0.45
σ_Y (MPa)	200	1000	1000	5250

^a (Bensimon, *et al.*, 1995);

^b (Manning, 1986; Manning, 2012)

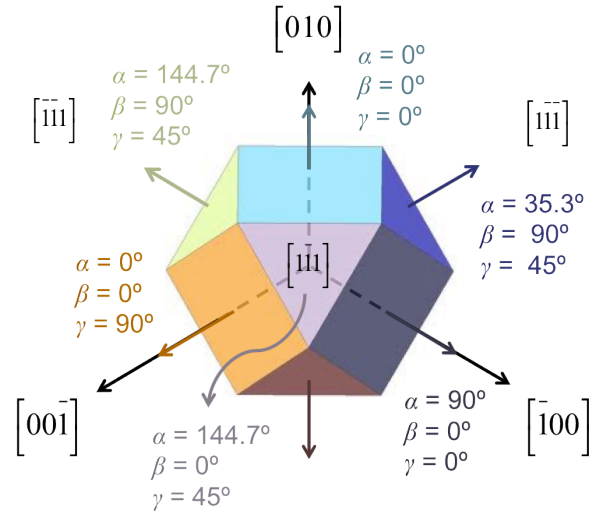


Figure 4.1: Euler angle computations for the textured cuboctahedral nanoparticles.

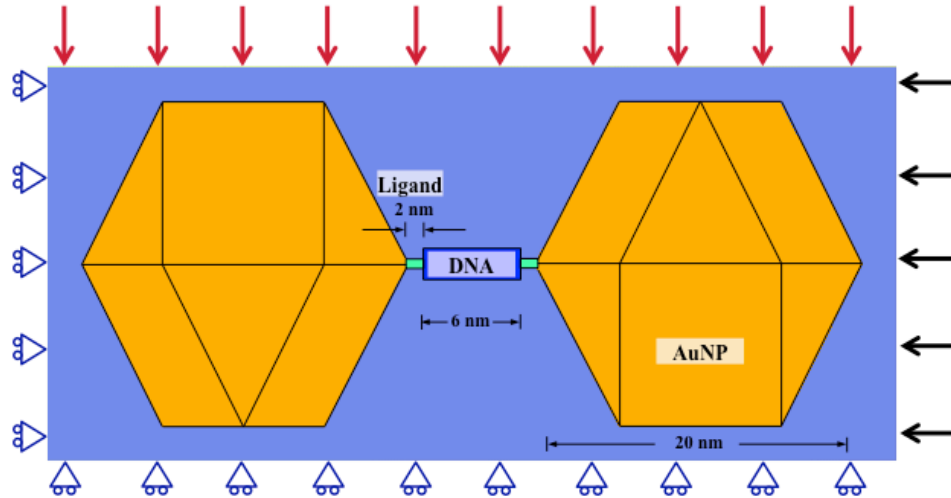
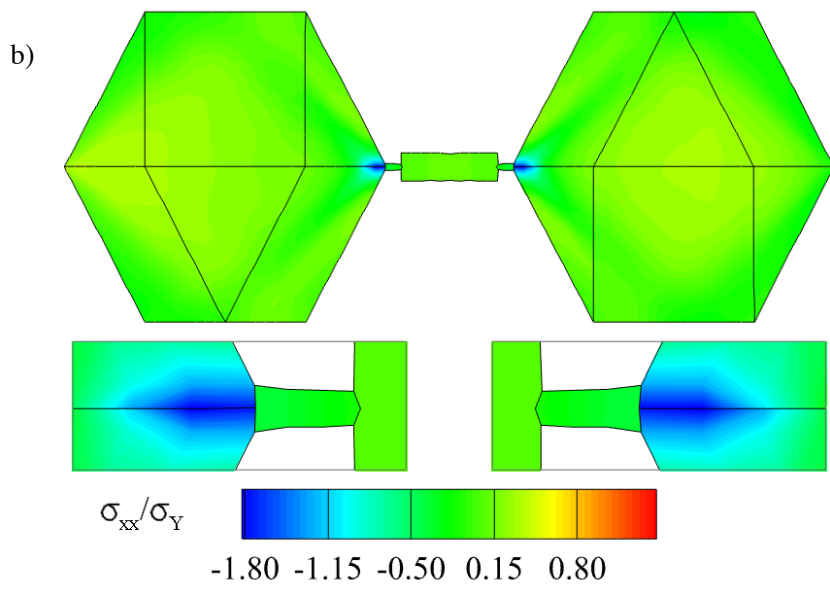
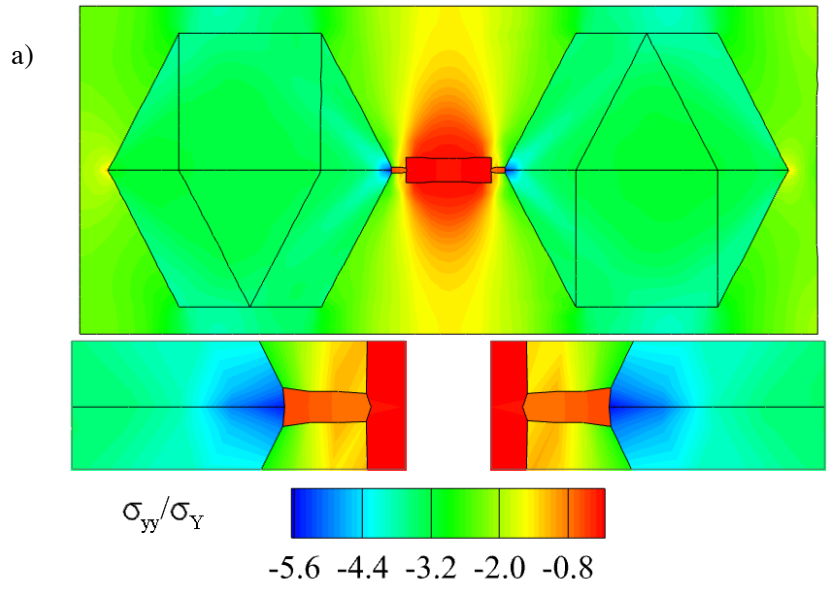


Figure 4.2: The heterogeneous AuNP-DNA system in plane strain uniaxial displacement loading (*red arrows*) and plane strain biaxial displacement loading (*red + black arrows*).

Figure 4.3: Normalized (a) lateral, (b) normal, (c) shear, and (d) z-axis lateral stress for a system of 20 nm AuNPs with 6 nm DNA at 2% nominal compressive strain.



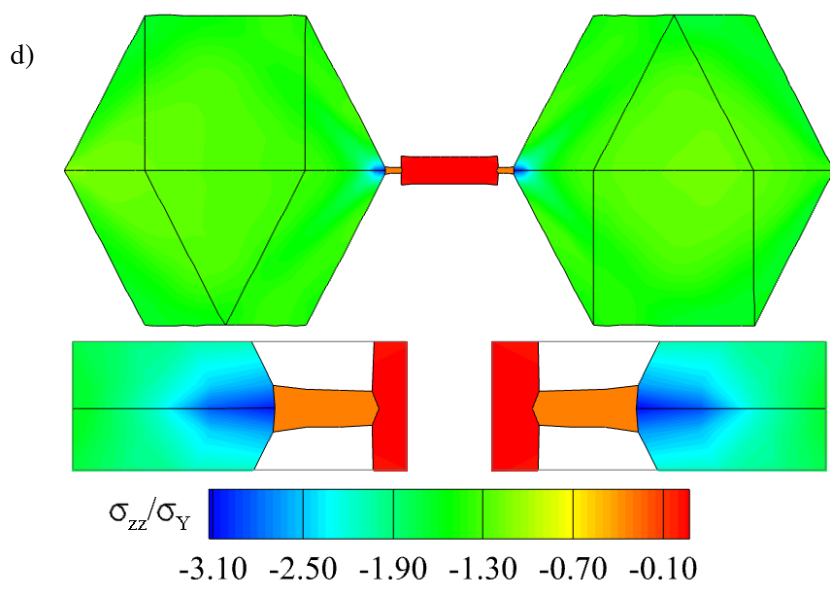
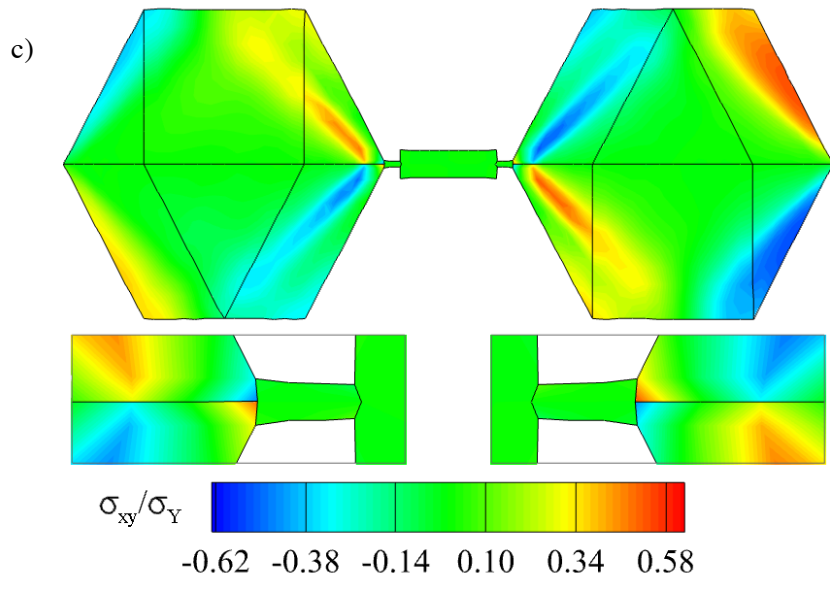
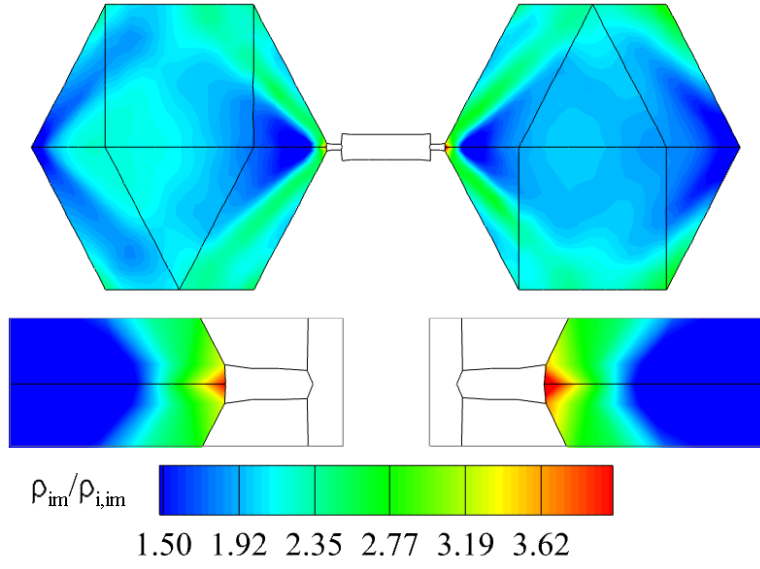
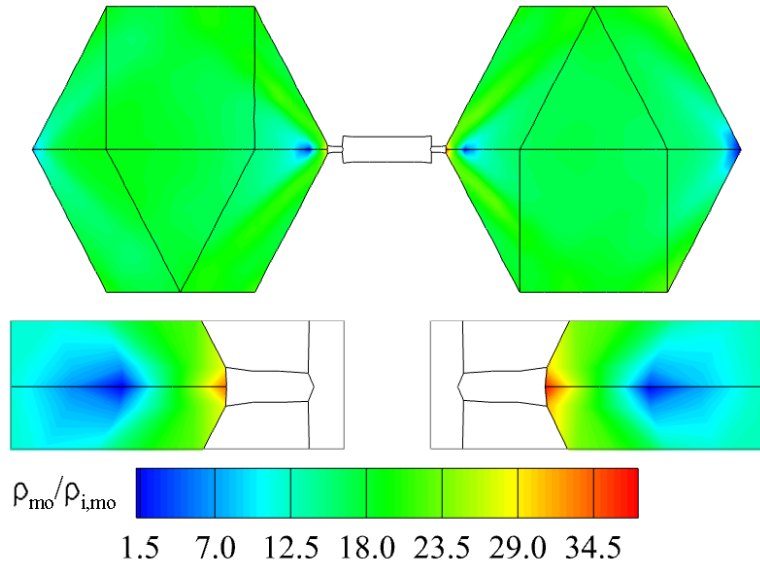


Figure 4.4: AuNP plasticity: (a) Immobile and (b) mobile dislocation-densities and (c) slip rates for 6 nm DNA and 20 nm non-textured AuNPs for the most active slip system (1-11)[011]. All values are normalized to their pre-loading values. Shear slip is also shown (d). Regions left blank have no plastic accumulation.

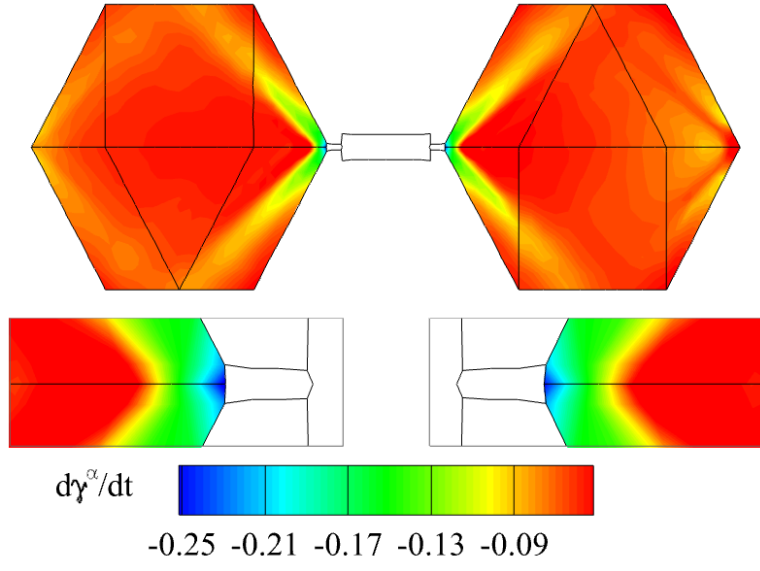
a)



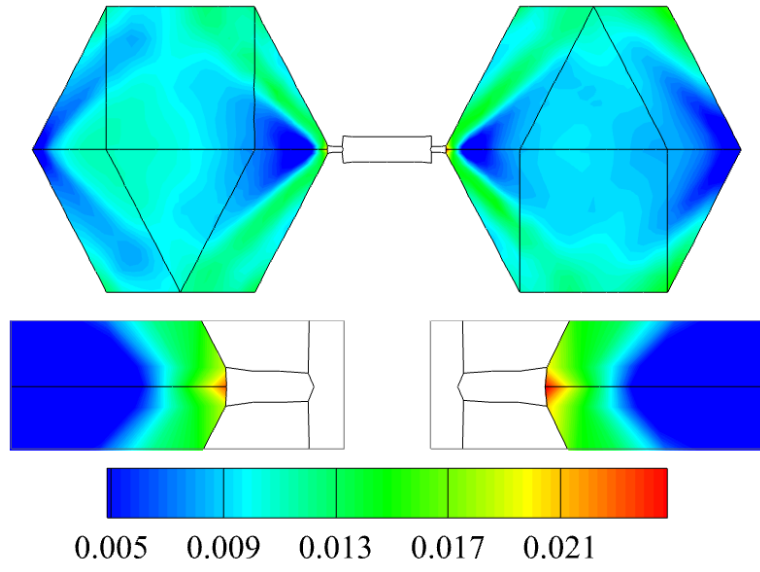
b)



c)



d)



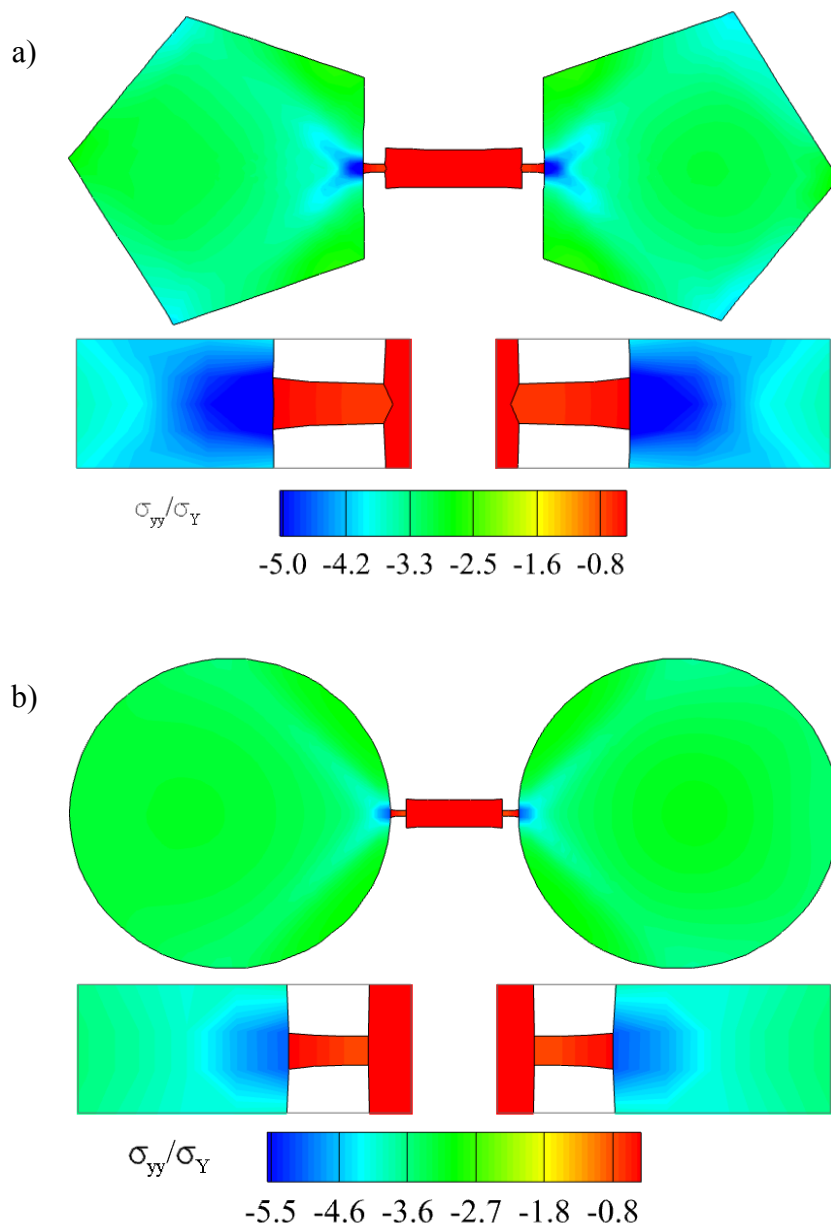


Figure 4.5: Normalized normal stresses for 13.5 nm pentagonal nanoparticles with 6 nm DNA and (b) for 20 nm circular nanoparticles with 6 nm DNA.

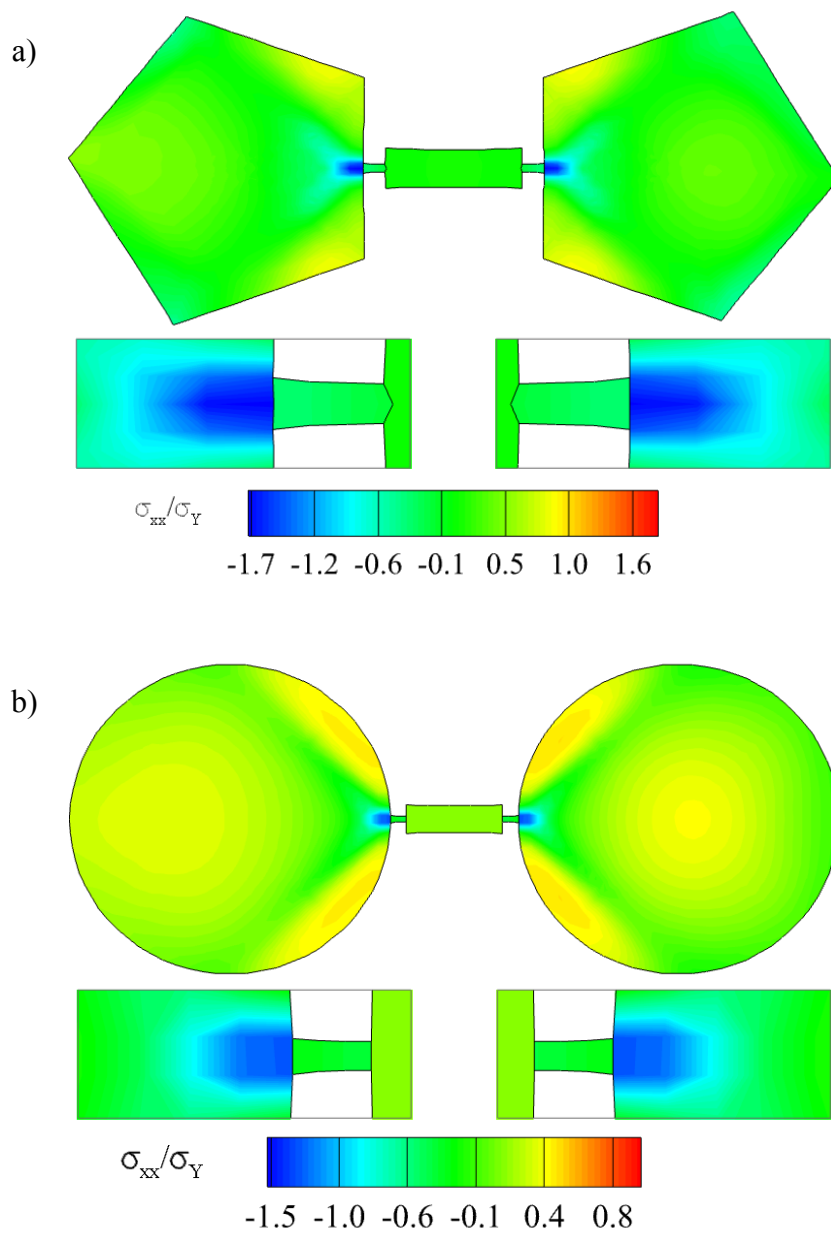
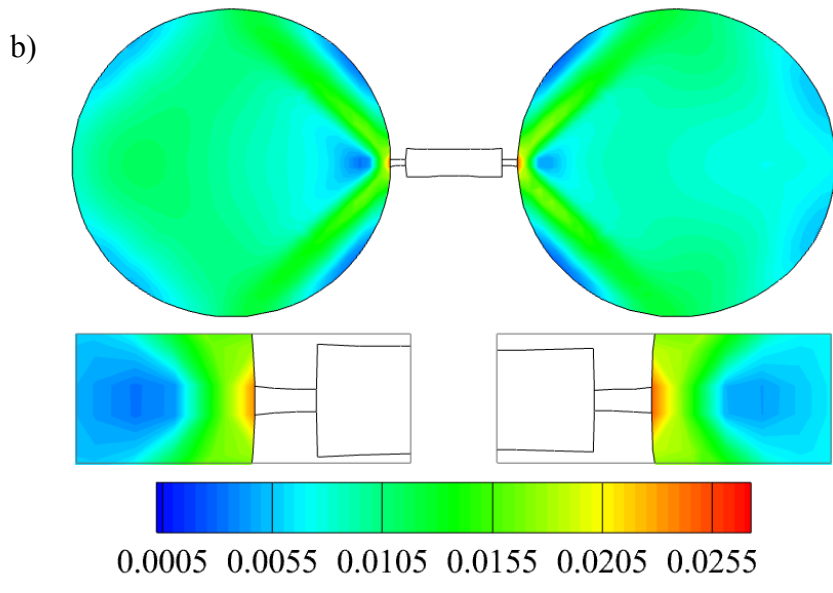
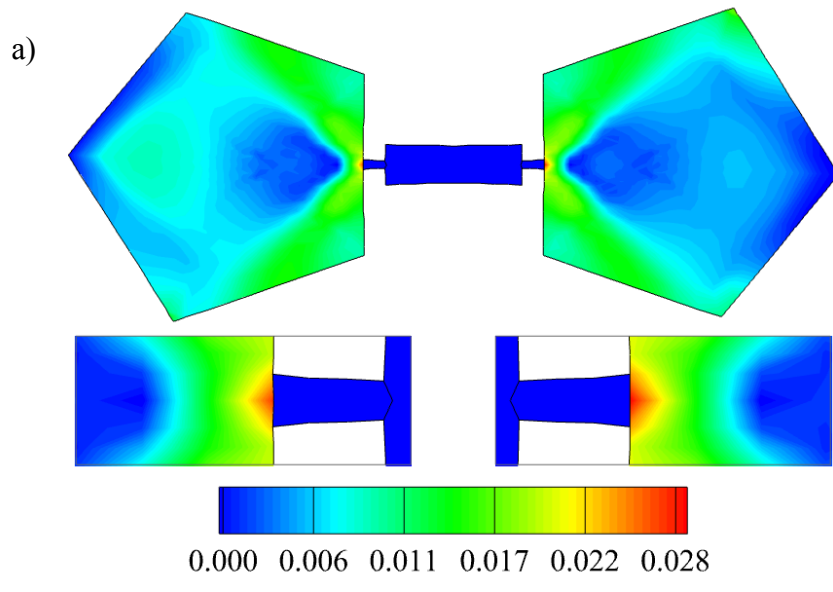
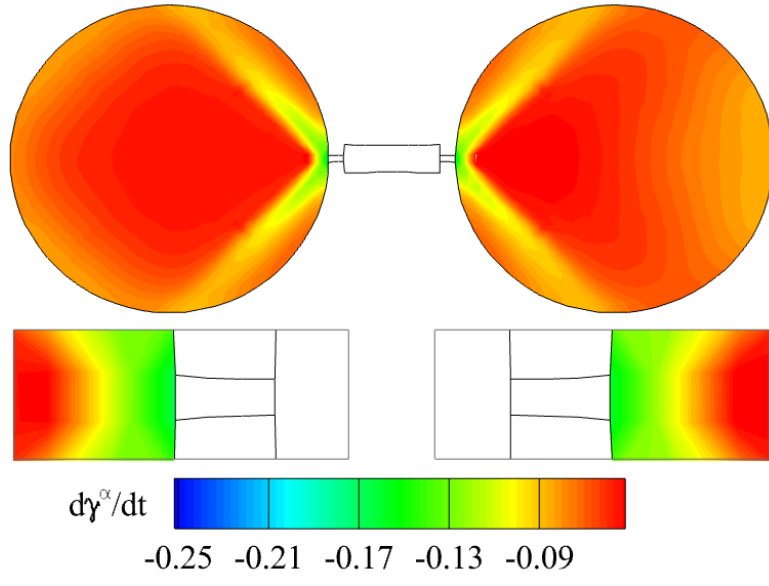


Figure 4.6: Normalized lateral stresses for 13.5 nm pentagonal nanoparticles with 6 nm DNA and (b) for 20 nm circular nanoparticles with 6 nm DNA.

Figure 4.7: (a) Shear slip for 13.5 nm pentagonal particles. (b) Shear slip and (c) slip rates for the most active slip system (1-11)[011] for 20 nm circular nanoparticles.



c)



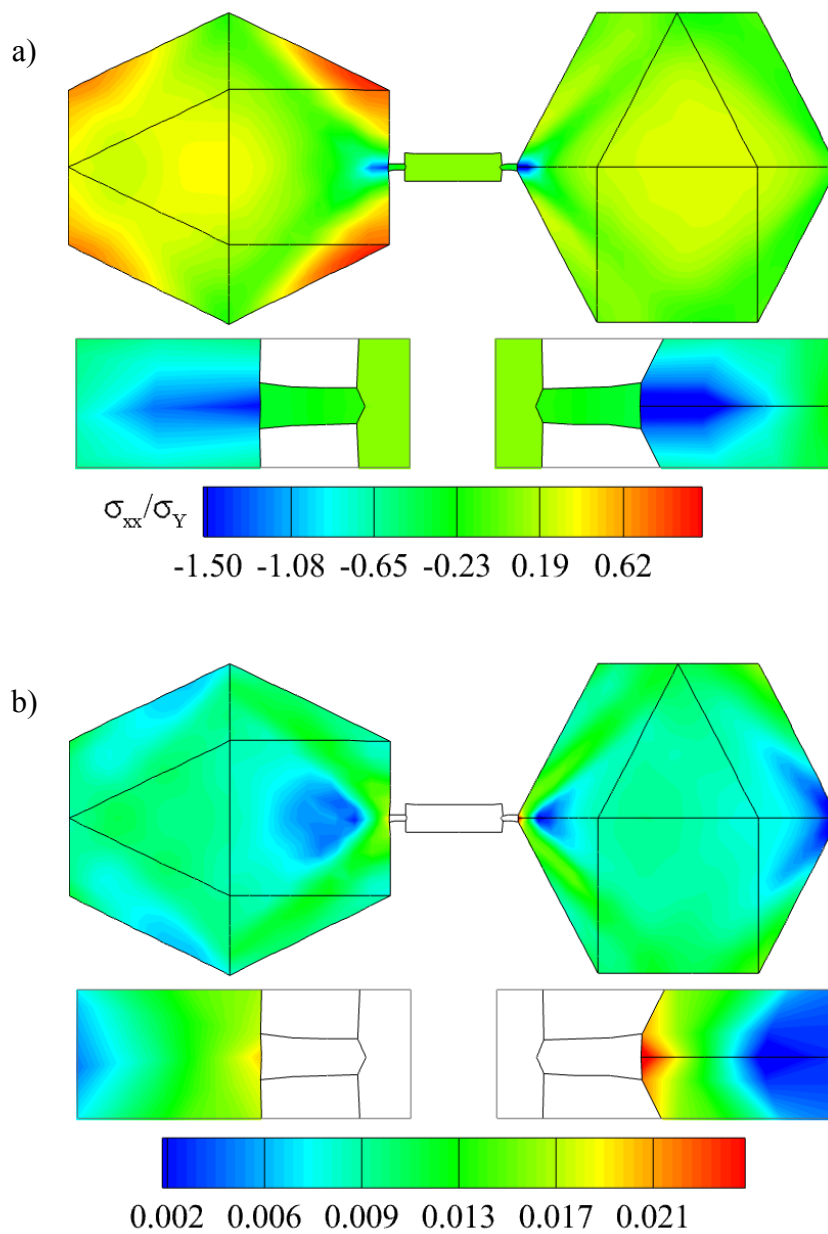
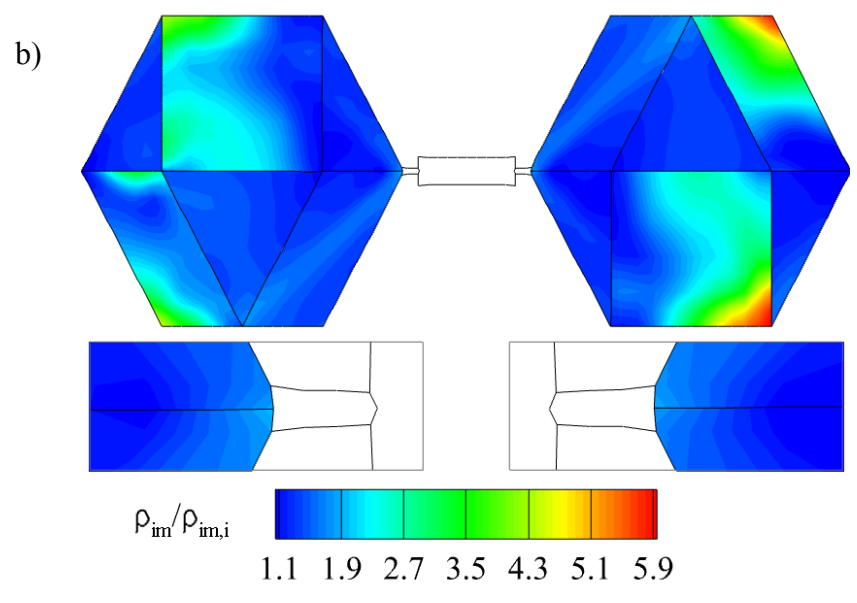
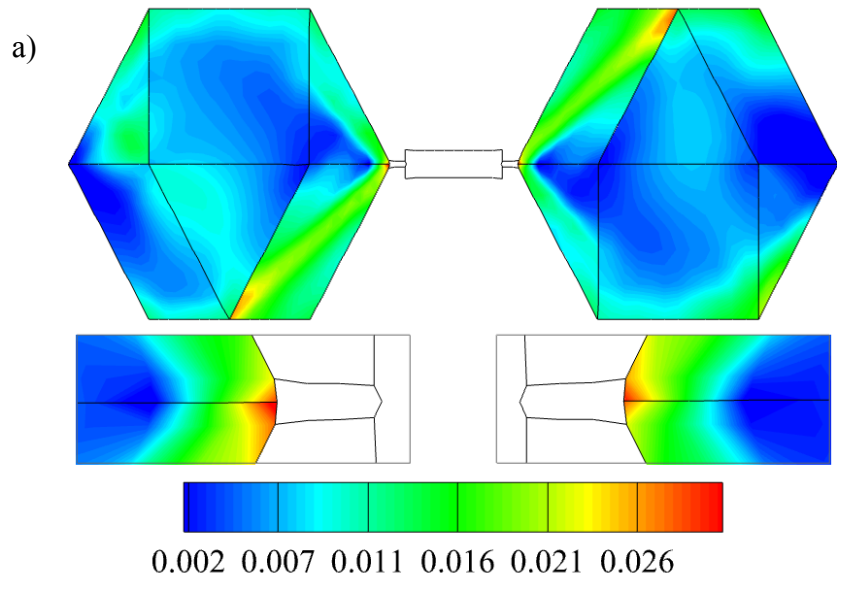
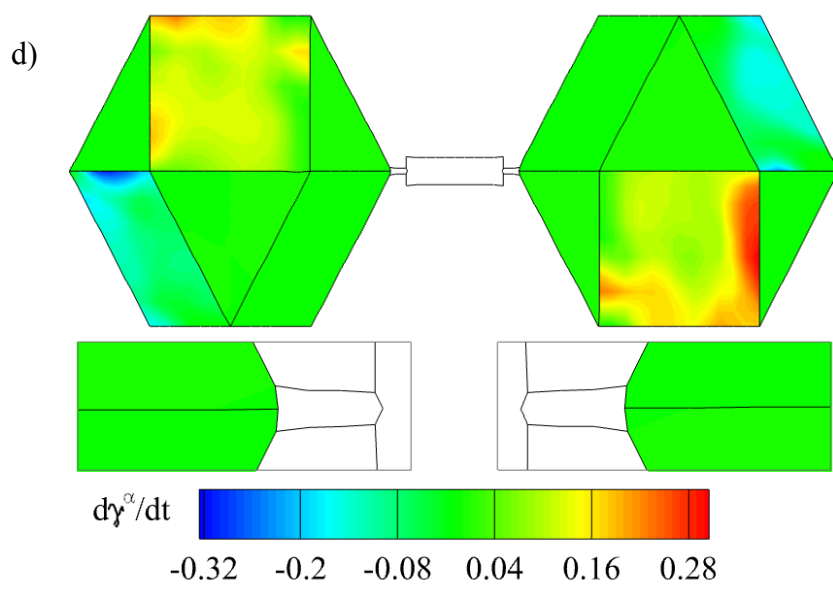
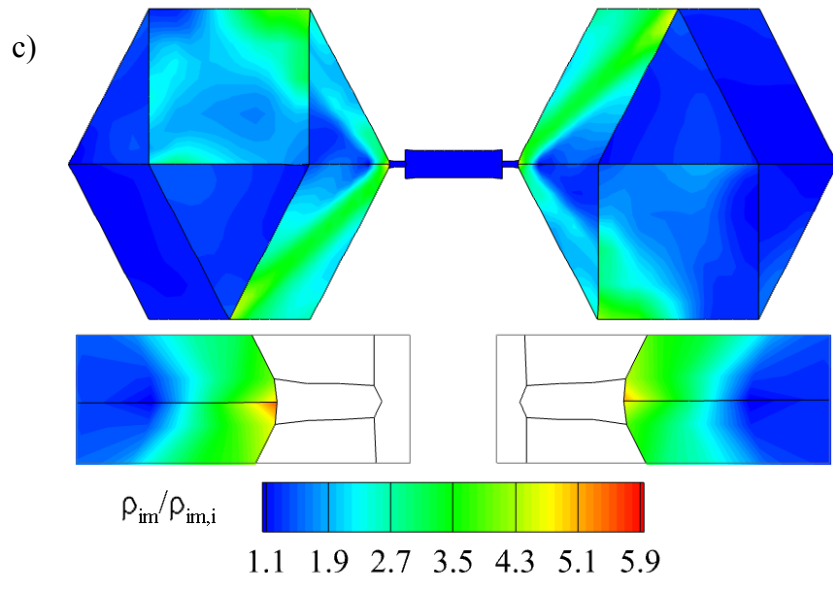


Figure 4.8: (a) Normalized lateral stress and (b) shear strain for 6 nm DNA and rotated, non-textured cuboctahedral particles.

Figure 4.9: (a) Shear slip, (b) immobile dislocation-density for the most active slip system (111)[-1-10], (c) immobile dislocation-density for the second most active slip system (111)[0-1-1], and (d) slip rates for the most active slip system (111)[-1-10].





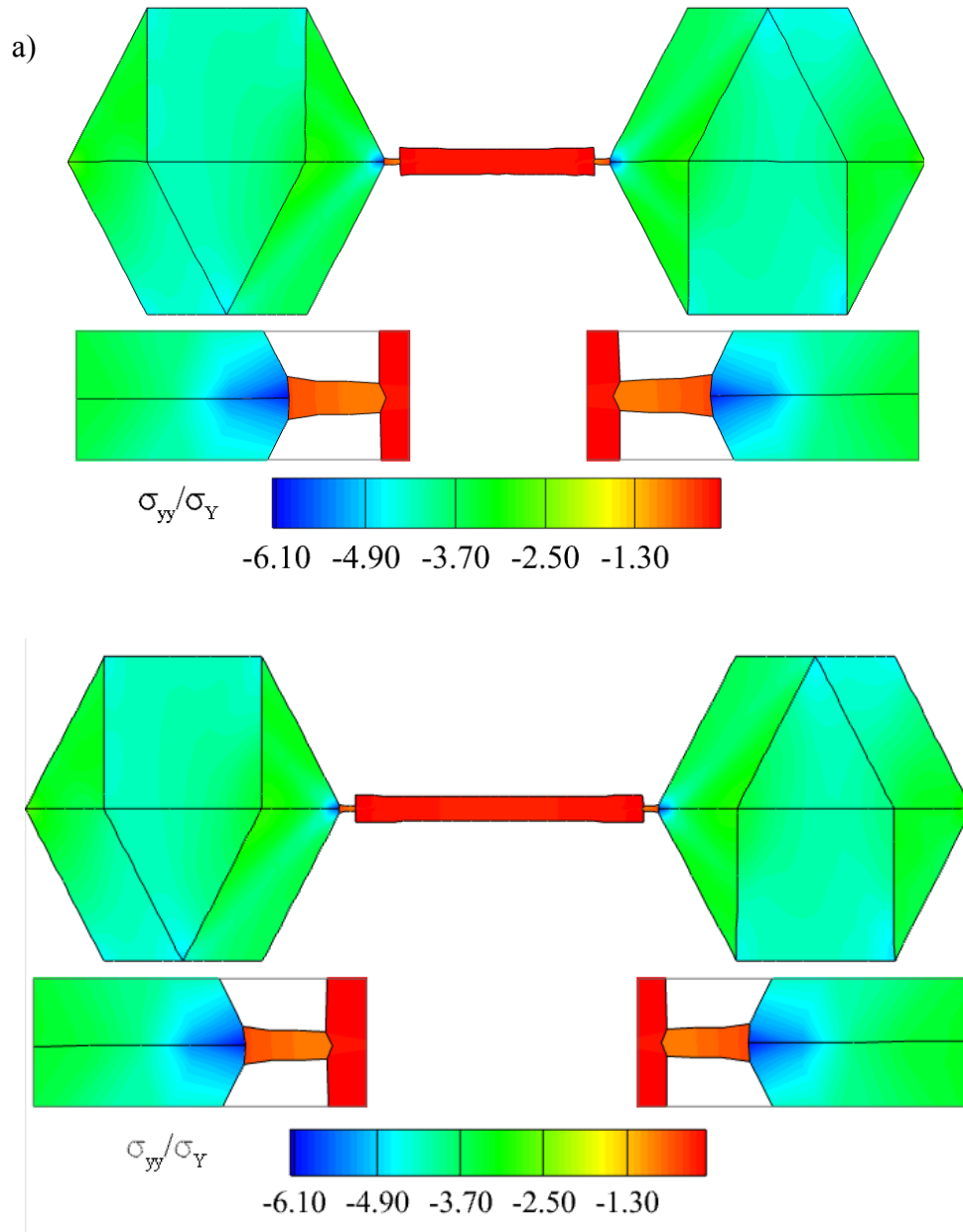


Figure 4.10: Normalized normal stress in systems with (a) 12 nm and (b) 18 nm DNA. Compare with figure 3a.

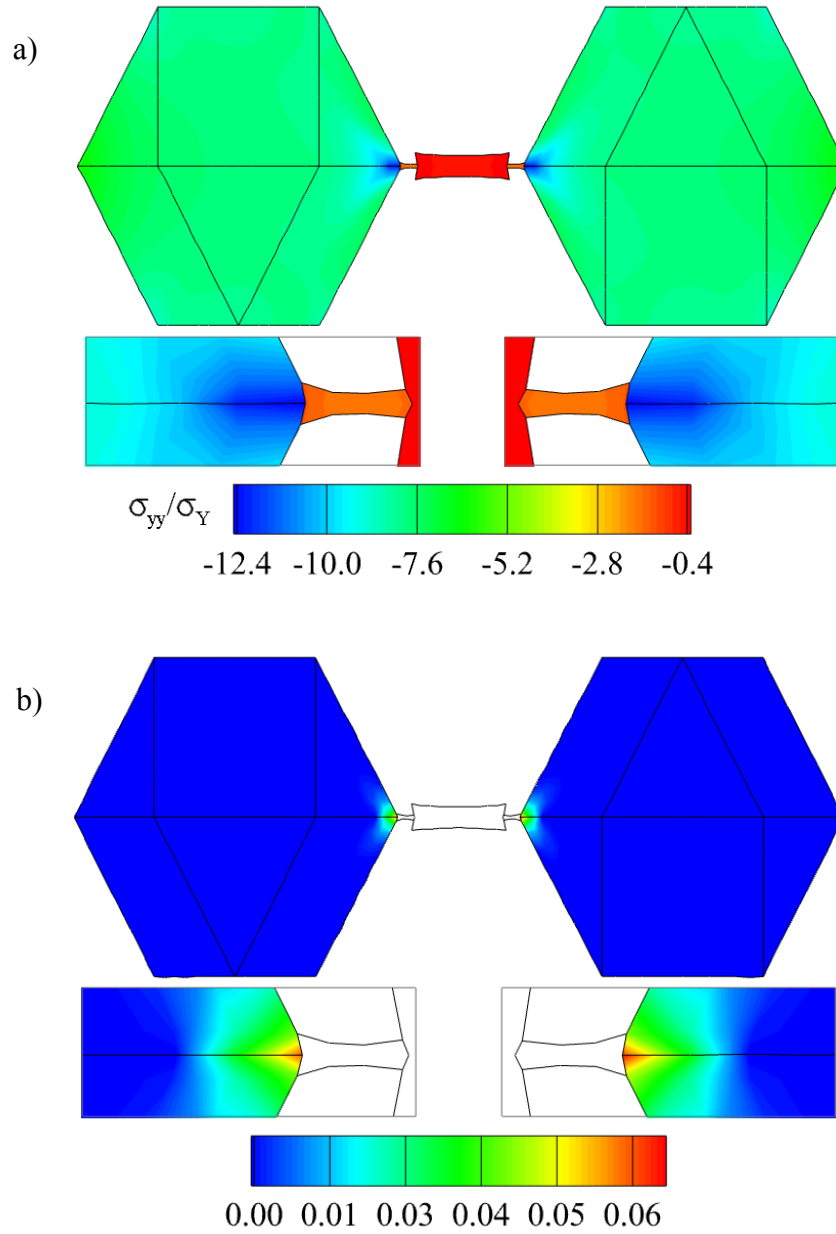


Figure 4.11: (a) Normalized normal stress and (b) shear slip for the system with biaxial displacement loading conditions at 1.2% nominal strain.

CHAPTER 5: Strength of AuNP-DNA Superlattice Systems

Composites in which the controlled arrangement and distribution of gold nanoparticles can be facilitated by utilizing functionalized DNA can be arranged in superlattice systems with crystallographic structures that mimic f.c.c. crystalline lattices. Control of AuNP placement is critical for new optical and electronic technologies and materials. Hence, a large-scale specialized finite-element approach with a dislocation-density based crystalline plasticity has been used to investigate the mechanical stability of AuNP-DNA superlattices and to provide guidelines for failure resistant systems. The effects of varying AuNP volume fractions and size, matrix strength, stress anisotropy and nanoparticle crystallographic orientations were analyzed to characterize the mechanical behavior of AuNP-DNA f.c.c. superlattice composites. The predictions indicate f.c.c. superlattices can have a combination of high strength and ductility, which is an indication that they can be candidate building blocks for new failure resistant material systems.

5.1 Motivation

It is well established that gold nanoparticles have desirable physical features not in bulk materials (Kelly, Coronado, Zhao, & Schatz, 2003), such as surface plasmon resonance (El-Sayed M. A., 2001). The ability to preferentially place AuNPs into three-dimensional structures with nanometer precision is highly sought after, and yet very few methods have come close to this achievement. Two-dimensional periodic particle arrays have been constructed using top-down approaches like nanosphere lithography (Hulteen & Van Duyne, 1995), electrodeposition (Lu & Tanaka, 1996), and laser pulses (Chumanov, Sokolov, Gregory, & Cotton, 1995), and three-dimensional advances that include bottom-up molecular

self-assembly (Zhang, 2003). Bottom-up molecular assembly is far less tedious than lithography and deposition techniques because molecules and particles self-organize. However, until recently, control over the placement of nanoparticles has proven difficult. Recently, though, Mirkin, *et al.* have conducted numerous investigations focused on functionalizing AuNPs with DNA using molecular assemblies to form three dimensional particle arrays called superlattices using DNA to govern the periodic positions of nanoparticles (Storhoff & Mirkin, 1999; Senesi, *et al.*, 2013).

The appeal of utilizing AuNP-DNA superlattices, including bottom-up assembly and predictable architecture control from precise nanoparticle placement, has spawned much experimental research. However, like the smaller systems in Chapter 4, little work has been done to optimize these nanoparticle lattices for mechanical stability. Experimental techniques such as *in situ* characterization methods are lacking, and atomistic and molecular dynamic techniques are too limited to adequately represent superlattices that have been processed, see for example Lee & Schatz (2009) and Singh, Snyder, Lee, Johnston, Caruso, & Yingling (2010).

The chemical assembly methods of AuNP-DNA superlattices are similar to those methods presented in Chapter 4. AuNPs are modified with oligonucleotides in solution, then agglomerate via the introduction of linker DNA, and an indefinitely stable crystalline lattice with accurately placed AuNPs is formed. For lattice structures, though, precise DNA lengths are crucial to accurately design the desired crystallographic assembly. Ultimately, the crystalline structure is governed by the hydrodynamic radius, which is comprised of the radius of the AuNP, the ligand and half the linker DNA, giving half the center-to-center

particle distance. Macfarlane, Lee, Jones, Harris, Schatz, & and Mirkin have shown that body-centered cubic and face-centered cubic arrangements can be obtained by exploiting the complementary nature of the oligonucleotides and DNA linkers (2011). For instance, when assembling with one type of AuNPs, each with self-complementary oligonucleotide and DNA linkers, an f.c.c. superlattice can be attained.

This investigation has focused on predicting and developing guidelines that can be used for determining the mechanical stability of these f.c.c. superlattices. The strength and stability of f.c.c. AuNP-DNA superlattices, as well as single nanoparticles were analyzed using the large-scale finite-element method described in Chapters 2 and 3. A dislocation-density based crystalline plasticity model was used to represent the behavior of the Au nanoparticles, and an elasticity model was used to represent the behavior of the ligands and DNA. All nanoparticles were 6-25 nm in diameter. The interrelated effects of the ligands and DNA, matrix encapsulation, AuNP volume fraction and crystallographic orientations on strength, dislocation-density, and overall behavior were investigated for f.c.c. superlattices.

5.2 Results

Using the multiple slip dislocation-density based crystal plasticity and the finite element algorithm, superlattice constructions were investigated for strength, toughening, and overall mechanical stability. The effects of different Au volume fractions, textures, matrix strengths, and stability effects on the AuNPs and the entire system were analyzed. In the case of AuNP orientations with respect to loading, Euler angle distributions were used to represent crystallographic orientations (see Section 4.1: Approach).

Figure 5.1 shows a representative model used for an f.c.c. superlattice. Each run analyzed a cross section of the $\{1\ 1\ 1\}$ f.c.c. close-packed planes with plane strain loading in $[1\ 1\ -2]$. As shown, the f.c.c. superlattice is represented by an AuNP placed on the center face and other AuNPs placed along the vertices. The model consists of 14, 6 - 24 nm diameter AuNPs with ligand-DNA-ligand connections to each nearest neighbor AuNP, representing the least amount of connections necessary to build an f.c.c. superlattice. Each assembly's dimensions depend on the both the Au volume fraction and its crystallographic lattice constant, with the addition of 4 nm of matrix material bordering the outermost AuNPs, giving an approximate cross sectional area of .01 to .02 μm^2 .

Because highly faceted f.c.c. AuNPs are regularly produced in the fabrication of the DNA-AuNP composites (Macfarlane, *et al.*, 2011), and because there is no great loss in the overall strength and stability analysis by ignoring individual AuNP shape (Lam & Zikry, 2013), each AuNP was modeled as a round, f.c.c. crystal with mechanical properties as seen in bulk Au (*see Table 5.1*).

DNA dimensions and elastic properties were obtained from experimental investigations, and the same assumptions from Chapter 4 were applied here. Each strand was assumed to be completely hybridized with the single stranded oligonucleotide linkers, forming perfect double-stranded DNA. Because the modulus of dsDNA is nucleotide-sequence dependent (Olson & Zhurkin, 2000), it has also been assumed that there were no A or T tracks that would cause intrinsic curvature, allowing all DNA to be modeled as isotropic elastic (Table 5.1). The rise per base pair of 0.26 nm and 2 nm diameter of each DNA strand was also inferred from experimental measurement (Macfarlane, Lee, Jones, Harris, Schatz, & Mirkin,

2011). During the analysis, different lengths of DNA were used and determined by the volume fraction of Au and the hydrodynamic radius of the specific model.

Gold and sulfur form a strong chemical bond, and therefore, the ligand is assumed to be a short functionalized thiol whose sulfur atom has bonded with the Au surface of the crystal. Each AuNP-DNA system was modeled with a single ligand connecting each dsDNA to its adjacent nanoparticle. The dimensions of the ligand material were chosen such that they encompassed each of the atomic bonds in the thiols, including the carbon and hydrogen atoms in their molecular backbone (Figure 5.1).

5.2.1 Effects of DNA and Ligands

In order to exploit the unique electro-optical properties of AuNPs in the periodic arrangement of superlattices, AuNP-DNA constituents must withstand application-specific mechanical loading conditions. The colloidal mixtures in which the structures are assembled limit the usefulness of the system, but the rod-like nature of the dsDNA is only maintained in ionic solutions. Recently, experiments by Auyeung, *et al.*, have shown that a stronger matrix can replace the colloidal solution in AuNP-DNA without significantly altering the ordering of the AuNPs (Auyeung, Macfarlane, Choi, Cutler, & Mirkin, 2012). To date, this is the only known method of transitioning AuNP-DNA systems into a solid-state composition. The DNA and ligand attachments, since the process involves encapsulation of the superlattice components, are preserved in the matrix. Hence the effects of DNA and ligands applied to the composites' and nanoparticles' stability are an essential aspect of defining the fundamental behavior of nanoparticle lattices which is also consistent with results of two-

dimensional nanoparticle superlattices suspended over micrometer-sized holes found by Mueggenburg, *et al.* (2007).

In this analysis, a superlattice with AuNPs, ligands and DNA, and two systems without ligands or DNA: one with AuNPs periodically arranged, the other with AuNPs randomly distributed throughout the matrix, were compared. The periodically and randomly arranged superlattices, with no DNA, had essentially the same normal stresses (Figure 5.2, *center* and *right*). These normal stress contours correspond to a close-packed $\{111\}$ plane at a nominal compressive strain of 2%. The presence of the ligands and the DNA, similar to transitioning superlattices from colloidal solutions to rigid materials (Auyeung, Macfarlane, Choi, Cutler, & Mirkin, 2012), result in tensile stresses in the ligand-DNA regions. These tensile stresses occur due to the negative Poisson's ratio of the DNA. When all three systems are strained to 2% nominal compressive strain along $[1\ 1\ -2]$, the system with DNA and ligands has approximately twice the normal compressive stress of the AuNPs without the DNA and ligands. These large normal stresses for the AuNP-DNA ligand arrangement occur at the DNA-ligand attachment. Therefore, these predictions indicate that the presence of the DNA and the ligands results in higher compressive stresses at the attachments, which would correspond to higher strengths. The tensile stresses, due to the DNA and ligands, indicates that the tensile stresses will cause expansion in the normal direction, and this can be used, with a matrix, to mediate the large attachment stresses.

The global stress-strain curves for an f.c.c. AuNP-DNA superlattice as well as for a system with periodically arranged AuNPs, both encapsulated in the same matrix material, are shown in Figure 5.3. The AuNP-matrix has a higher global stress-strain response than the

AuNP-DNA superlattice. This is due to the lower modulus of the DNA and ligands, which would affect the average response. As noted earlier, though, high stresses occurred at the attachments between the AuNPs and ligands. To further underscore this, the local normal stresses are shown for one of the AuNPs (Figure 5.3, *right*). These stresses are plotted along a line normal to the AuNP surface (*bright green line in Figure 5.3 inset*). The stresses for the nanoparticle with linker attachments are higher than the same nanoparticle suspended only in matrix material. Furthermore, because the ligand and DNA material properties are significantly different than the AuNP, the linker's expansion results in a region of concentrated stress surrounding the point of attachment (see inset of Figure 5.2).

AuNPs tethered with DNA resulted in accumulated plasticity adjacent to the AuNP-linker interface. The ligands and DNA act as attachments, concentrating stresses at these interfaces. The high normal stresses within the AuNPs cause yielding, which leads to an accumulation of mobile and immobile dislocation-densities, (Figure 5.4, *left*), similar to the Au nanoparticle indentation study by Mordehai, *et al.*, in which dislocations were observed to nucleate near the indenter tip (2011). Plastic localization did not occur in AuNP-matrix composites lacking DNA linkers, also shown in Figure 5.4 (*center*), nor did the random arrangement of particle locations affect overall dislocation-density distribution in the AuNPs (Figure 5.4, *right*). In Mordehai, *et al.*'s study, dislocations were observed to nucleate at the indenter, and then glide to lateral particle facets. In this work, however, the surfaces of AuNPs are not free surfaces, as they abut with the rigid, elastic matrix material as well as the ligand attachments, and so dislocations would not be expected to readily create surface steps from gliding to the lateral particle facets. Instead, the dislocation-densities are immobilized

(as indicated by the increase in immobile densities) and accumulate at the ligand-DNA attachment sites. In this analysis, only DNA linkers along the close-packed directions are represented. However, in reality each NP is attached to tens or hundreds of dsDNA and ligand linkers, and so many areas of elevated dislocation-density accumulation would be present in each AuNP, since the crystallographic orientation of the AuNPs and linker angles relative to loading facilitate plastic slip. The shear slip (Figure 5.5) consistently displayed a similar relation between inelastic strains and ligand attachments. These results clearly indicate that the linker attachments redistribute the dislocation-densities and the subsequent plasticity to accumulate near the attachment point. Therefore, not only do the DNA linkers provide strength, but some toughness that can mitigate onsets of fracture, by lowering local stresses.

5.2.2 *Effects of Superlattice Crystallographic Orientation with Respect to Loading Axis*

System stability was investigated by extracting the stresses along the AuNPs, DNA, and ligands along two directions in the f.c.c. superlattice. The stresses along the $[-1\ 1\ 0]$ and $[1\ 0\ 1]$ directions, representing close-packed directions normal and 30° to applied strains, respectively, are shown in Figure 5.6 (*inset*). The stresses were obtained by plotting the stresses along the integration point in the slip-directions. Large stress gradients have evolved at AuNP-ligand interfaces normal to loading (*red line*), while those along $[1\ 0\ 1]$ were half as large at a nominal compressive strain of 2%. The directionality of these stress gradients in superlattices parallels those of pure crystalline materials as both are subject to preferential weakening along specific slip systems. These gradients can lead to failure or detachment between Au and S atoms, possibly leading to superlattice fracture and collapse.

5.2.3 Effects of Matrix Strength and Load Transfer

AuNP-DNA superlattice composites can be tailored to desired mechanical behavior, which can result in design guidelines for superlattices to be employed in devices and materials not feasible in colloidal environments. Transitioning the superlattices into a more durable material matrix retains the advantages of the regular AuNP spacing while simultaneously increasing application potential.

In this analysis, four elastic materials were selected as matrix elements for AuNP-DNA superlattice models, such that the effects of stiffness and load transfer on the overall system can be understood. The matrix materials were chosen so that they had a variable range of stiffness. The Young's modulus of each matrix material was assigned a factor of the elastic modulus of bulk gold, and these were chosen as $E_{\text{matrix}} = \frac{1}{4} E_{\text{Au}}$, $\frac{1}{10} E_{\text{Au}}$, $\frac{1}{100} E_{\text{Au}}$, and $\frac{1}{1000} E_{\text{Au}}$. Each AuNP-DNA superlattice material was loaded to -2% nominal strain, and the global stress-strain curves are plotted in Figure 5.7. These systems have 24 nm diameter AuNPs with approximately 6 nm connecting dsDNA. Stress-strain curves for the four superlattice composite materials (*solid lines*) demonstrated a reduction in the critical nominal strain point for the onset on yielding. As the matrix material became stiffer, the stress required to yield the superlattice composite was significantly higher. For systems consisting only of matrix material with the same stiffness (*dashed lines*), the addition of AuNPs and DNA into the matrix lowered the yield stress, reducing the toughness of the system. However, because the elastic moduli for superlattices were substantially higher than their corresponding matrix-only moduli, the addition of the AuNPs and DNA effectively strengthened the composite.

5.2.4 Effects of AuNP Orientations with Respect to the Loading Axis

Once the AuNPs and DNA are transitioned into a rigid matrix, the application potential drastically increases. The mechanical strength and stability of AuNP-DNA superlattices as a measure of material durability is thus critical to understanding the overall behavior. Since Au is a crystalline material, behavior will depend on the crystallographic orientation of the metallic nanocrystals. In general, plasticity in the AuNPs is a measure of the resolved shear slip on each system as determined by the loading orientation. Slip activation and plasticity in the AuNP-DNA nanocrystals, then, varies with the distribution of orientations of the AuNPs (see, for example McLaughlin & Zikry, 2012).

Quantification of plastic variation based on texture between three AuNP-DNA superlattice composites was investigated by creating systems with three distributions of intrinsic nanoparticle crystallographic orientations: 1) a system in which all AuNPs have (1 0 0) planes aligned with the loading axis, 2) a low angle orientation system in which the (1 0 0) plane between AuNPs is allowed to randomly differ by less than 15°, and 3) a high angle orientation system in which a 30° random variation between the (1 0 0) plane to the loading axis is allowed. All volume fractions of gold, AuNP radii, and DNA lengths were the same between the three systems. Mobile and immobile dislocation-density accumulation was significantly affected by this orientation variation. The immobile dislocation-densities in one of the most active crystallographic slip systems, (111) [-1 0 1] is shown in Figure 5.8. When the AuNP crystallographic orientations are aligned with the loading direction (case 1), the dislocation-densities are uniform throughout the system. As the misorientation angles are allowed to span larger ranges, though, mobile and immobile dislocations-densities increase

depending on the particular slip system. For the active (1 1 1) [-1 0 1] slip system shown in Figure 5.8, for example, the highest dislocation-densities occur for a particle in the high angle random orientation system, while all other AuNPs have comparatively low dislocation-density. Significant dislocation differences between AuNPs arose in the low textured system as well, however, the disparity from particle to particle was not as great as it was for the high angle orientation case.

Control over crystallographic orientation of nanoparticles during experimental superlattice assembly is therefore critical. These variations in overall orientation would affect dislocation-density and plastic slip accumulation. For example, an AuNP for the high misorientation system had the largest normalized dislocation-density accumulation, which is approximately eight times higher than the case where slip systems were aligned with the loading axis. Given the small size of the crystals, only a few dislocations from even small strains need be nucleated before each defect is only nanometers from one another, leading to high internal stresses which lead to strain hardening and strengthening (Gerberich, *et al.*, 2005). The shear slip, which represents total plasticity on all slip systems, is shown in Figure 5.9. Shear slip was the highest for the high random angle case with a maximum of 3%, which is approximately eight times higher than the case where the slip systems were aligned with the loading axis. These variations in strength and toughness, as a function of misorientation, indicate that specific AuNPs can be targeted for strengthening and toughening.

5.2.5 Effect of Volume Fraction

Superlattices with the same hydrodynamic radius, but with different volume fractions of AuNPs were investigated. The systems with different volume fractions were created by decreasing the radius of each AuNP, while simultaneously lengthening the dsDNA. In this way, the hydrodynamic radius remains constant with AuNP radii of 24, 12, and 6 nm. Reducing the particle radii results in a decrease of the length and width of the entire systems' dimensions by at most 13 nm to allow for a uniform matrix border in each model. This process gave three systems with volume fractions, f_{Au} , 3.9, 1.6 and 0.2 (see Figure 5.10).

For all three volume fractions, the maximum normal stresses attained a maximum value of -1200 MPa. The difference between the three cases is that when the volume fraction is higher, the elastic effects of the DNA are minimized (Figure 5.10). The significance of this is that DNA can still provide the effects of attachments, but tensile elastic stress effects can be minimized.

Mobile and immobile dislocation-densities and shear slip also positively correlated with increasing volume fraction. Shear slip in the system with a volume fraction of 3.9 was nearly 200% higher than for the volume fraction case of 0.2. This substantiates that greater AuNP volume fractions add more ductility (Figure 5.11). By comparing systems with the same hydrodynamic radius loaded to the same nominal strain, it is clear gold nanoparticles are providing strength as well as toughness to AuNP-DNA superlattices with higher stresses and high plastic strains.

5.3 Conclusions

AuNP-DNA superlattices, in both colloidal solutions and when encapsulated in rigid matrices, have potential for a myriad of applications, and understanding and predicting the fundamental behavior of AuNP-ligand-DNA is essential. One potential application is as a material building block based on f.c.c. superlattices comprised of AuNPs, DNA strands, and ligands. The f.c.c. superlattice was based on using 14 AuNPs with ligand-DNA attachments along the close packed directions. The AuNPs provided both strength and toughness. The DNA and ligand attachments also facilitated hardening of the AuNPs by introducing large dislocation-density accumulation, and normal stresses at the attachment points. For compressive loading conditions, due to the negative Poisson's ratios, the DNA and the ligands provide tensile elastic strains, which can relax the large compressive stresses at the attachment points. Larger volume fractions of gold for the same hydrodynamic radius also resulted in particle hardening, strengthening and toughness. Furthermore, the f.c.c. superlattices had large stress gradients due to anisotropies, which can result resulting in ligand detachment and failure along specific planes because of instabilities at particle-ligand interfaces. The texture of AuNP-DNA superlattices resulted in stress inhomogeneities with significant changes in plasticity as a function of particle orientation. These predictions indicate that f.c.c. superlattices can be used as building blocks for new failure resistant materials, and this is due to controllable mechanisms and deformation modes related to AuNP size, orientations, and volume fractions.

REFERENCES – Chapter 5

- Ashmawi, W. M., & Zikry, M. A. (2002). Prediction of grain-boundary interfacial mechanisms in polycrystalline materials . *Journal of Engineering Materials and Technology: Transactions of the ASME*, 124, 88-96.
- Auyeung, E., Macfarlane, R. J., Choi, C. J., Cutler, J. I., & Mirkin, C. A. (2012). Transitioning DNA-engineered nanoparticle superlattices from solution to the solid state. *Advanced Materials*, 24, 5181-5186.
- Bensimon, D., Simon, A. J., Croquette, V., & Bensimon, A. (1995). Stretching DNA with a receding meniscus: Experiments and models. *Physical Review Letters*, 74 (23), 4754-4757.
- Chumanov, G., Sokolov, K., Gregory, B., & Cotton, T. M. (1995). Colloidal metal films as a substrate for surface-enhance spectroscopy. *Journal of Physical Chemistry*, 99, 9466-9471.
- El-Sayed, M. A. (2001). Some interesting properties of metals confined in time and nanometer space of different shapes. *Accounts of Chemical Research*, 34 (4), 257-264.
- Gerberich, W. W., Mook, W. M., Cordill, M. J., Carter, C. B., Perrey, C. R., Heberlein, J. V., *et al.* (2005). Reverse plasticity in single crystal nanospheres. *International Journal of Plasticity*, 21, 2391-2405.
- Hulteen, J. C., & Van Duyne, R. P. (1995). Nanosphere lithography: a materials general fabrication process for periodic particle array surfaces. *Journal of Vacuum Science & Technology A-Vacuum Surfaces and Films*, 13 (3), 1553-1558.
- Kelly, K. L., Coronado, E., Zhao, L. L., & Schatz, G. C. (2003). The optical properties of metal nanoparticles: the influence of size, shape, and dielectric environment. *Journal of Physical Chemistry B*, 107 (3), 668-677.
- Lam, L. M. & Zikry, M. A. (2013). The mechanical strength and stability of DNA-modified gold nanoparticle systems. *Manuscript submitted for publication*.
- Lee, O.-S., & Schatz, G. C. (2009). Interaction between DNAs on a gold surface. *Journal of Physical Chemistry C*, 113, 15941-15947.
- Link, S., & El-Sayed, M. (1999). Size and temperature dependence of the plasmon absorption of colloidal gold nanoparticles. *Journal of Physical Chemistry B*, 103, 4212-4217.

- Lu, D. L., & Tanaka, K. (1996). Gold particles deposited on electrodes in salt solutions under different potentials. *Journal of Physical Chemistry*, 100 (5), 1833-1837.
- Macfarlane, R. J., Lee, B., Jones, M. R., Harris, N., Schatz, G. C., & Mirkin, C. A. (2011). Nanoparticle Superlattice Engineering with DNA. *Science*, 334, 204-208.
- Manning, G. S. (1986). Correlation of polymer persistence length with Euler buckling fluctuations. *Physical Review A*, 34 (5), 4467-4468.
- Manning, G. S. (2012). Poisson's ratio for a polyelectrolyte. *Soft Matter*, 8, 9334-9337.
- McLaughlin, L. A., & Zikry, M. A. (2012). The mechanics and stability of gold-nanoparticle-oligo-ligand-DNA systems. In *Mechanical Behavior of Metallic Nanostructured Materials*, Edited By Q. Li, D. Farkas, P. Liaw, B. Boyce, J. Wang, pp. mrsf12-1513-gg10-16, *Materials Research Society Symposium Proceedings*, 1513, Warrendale, PA.
- Mordehai, D., Kazakevich, M., Srolovitz, D. J., & Rabkin, E. (2011). Nanoindentation size effect in single-crystal nanoparticles and thin films: A comparative experimental and simulation study. *Acta Materialia*, 59, 2309-2321.
- Mordehai, D., Lee, S.-W., Backes, B., Srolovitz, D. J., Nix, W. D., & Rabkin, E. (2011). Size effect in compression of single-crystal gold microparticles. *Acta Materialia*, 59, 5202-5215.
- Mueggenburg, K. E., Lin, X.-M., Goldsmith, R. H., & Jaeger, H. M. (2007). Elastic membranes of close-packed nanoparticle arrays. *Nature Materials*, 6, 656-660.
- Olson, W. K., & Zhurkin, V. B. (2000). Modeling DNA deformations. *Current Opinion in Structural Biology*, 10, 286-297.
- Olson, W. K., Marky, N. L., Jernigan, R. L., & Zhurkin, V. B. (1993). Influence of fluctuations on DNA curvature. A comparison of flexible and static wedge models of intrinsically bent DNA. *Journal of Molecular Biology*, 252, 530-554.
- Orsini, V. C., & Zikry, M. A. (2001). Void growth and interaction in crystalline materials. *International Journal of Plasticity*, 17, 1393-1417.
- Senesi, A. J., Eichelsdoerfer, D. J., Macfarlane, R. J., Jones, M. R., Auyeung, E., Lee, B., *et al.* (2013). Stepwise evolution of DNA-programmable nanoparticle superlattices. *Angewandte Communications*, 52, 6624-6628.
- Shanthraj, P., & Zikry, M. A. (2011). Dislocation density evolution and interactions in crystalline materials. *Acta Materialia*, 59, 7695-7702.

Singh, A., Snyder, S., Lee, L., Johnston, A. P., Caruso, F., & Yingling, Y. G. (2010). Effect of oligonucleotide length on the assembly of DNA materials: Molecular dynamics simulations of layer-by-layer DNA films. *Langmuir*, 26 (22), 17339-17343.

Storhoff, J. J., & Mirkin, C. A. (1999). Programmed materials synthesis with DNA. *Chemical Reviews*, 99 (7).

Zhang, S. (2003). Fabrication of novel biomaterials through molecular self-assembly. *Nature Biotechnology*, 21 (10), 1171-1178.

Table 5.1: Elastic properties of the AuNP-DNA components.

	AuNP	Ligand	DNA	Matrix
E (GPa)	70.0	0.35	0.11 ^a	17.5
ν	0.42	0.35	-0.70 ^b	0.45
σ_Y (MPa)	200	1000	1000	5250

^a (Bensimon, Simon, Croquette, & Bensimon, 1995)

^b (Manning, 1986; Manning, 2012)

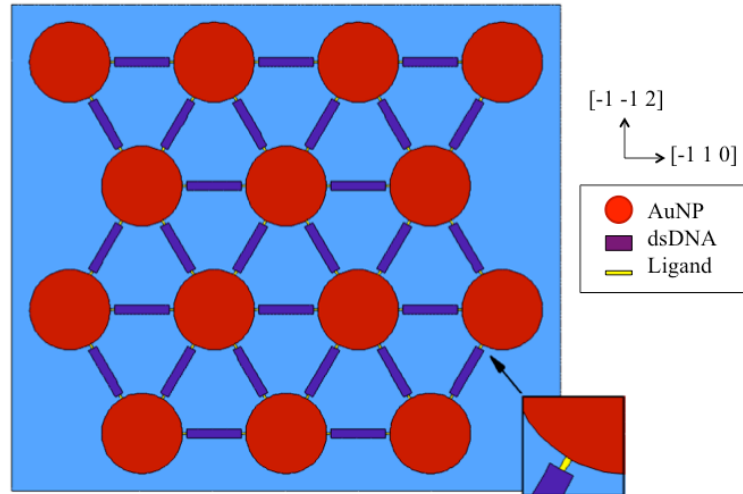


Figure 5.1: An f.c.c. superlattice with AuNPs, DNA, and ligands (*inset*). The (1 1 1) close packed plane is shown, and loading is applied along the $[1 1 -2]$ direction.

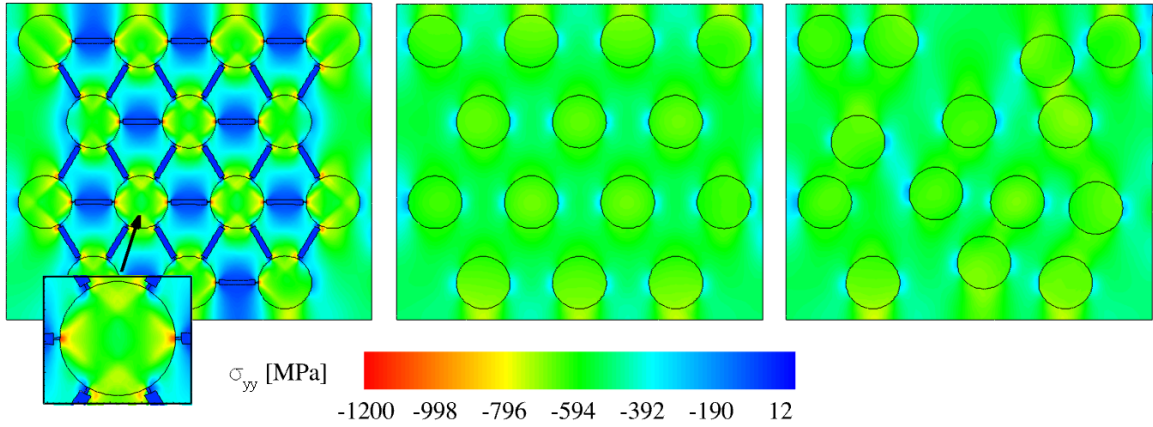


Figure 5.2: Normal stresses for a $\{1\ 1\ 1\}$ cross section of an f.c.c. AuNP-DNA superlattice (*left*), AuNPs/matrix composite with the same nanoparticle-spacing without DNA (*middle*), and AuNPs/matrix composite with random nanoparticle spacing without DNA (*right*). The ligand and DNA attachments concentrate stresses at the ligand-AuNP interface.

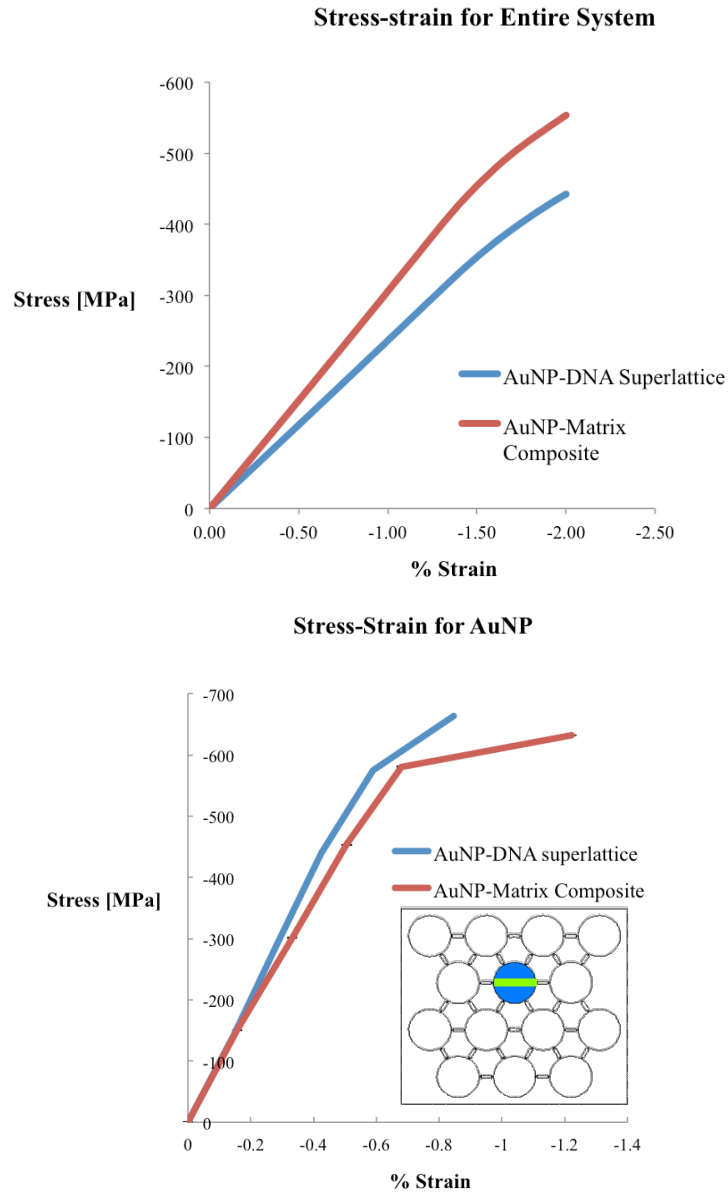


Figure 5.3: Global and local stress-strain curves for AuNP composites with and without DNA. (*Left*) When the AuNPs are regularly spaced using DNA (*blue*) a lower nominal stress is required to strain the material than when DNA is absent (*red*). However, the local stress-strain curve for one AuNP in the superlattice (*see inset for nanoparticle location*) and AuNP-matrix composite (*right*) reveal strengthening of the nanocrystals with the presence of the DNA.

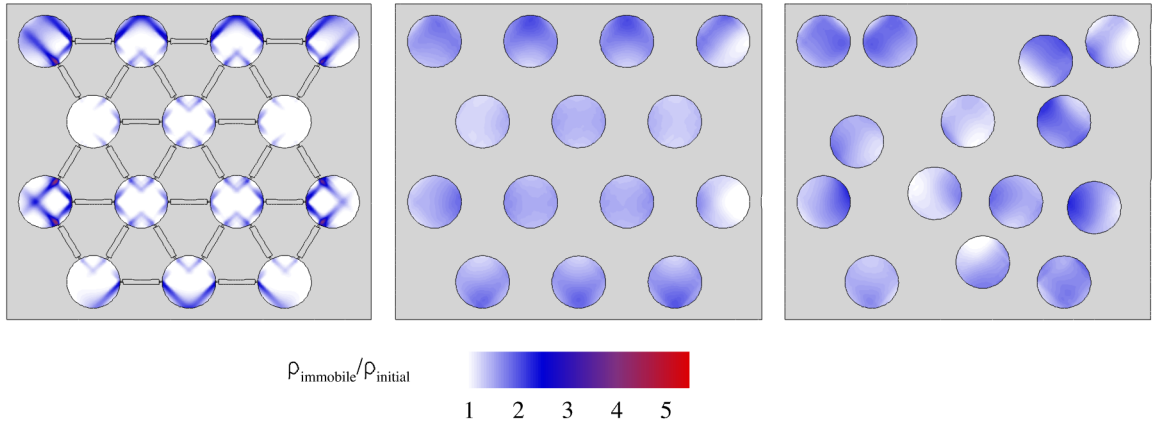


Figure 5.4: Immobile dislocation-densities for superlattices and AuNP-matrix composites without DNA linkers. Concentrated regions of stress in AuNPs resulting from ligand and DNA linkers in AuNP-DNA superlattices resulted in high dislocation-density accumulation adjacent to the attachment region. Dislocation-densities were uniform for the systems without DNA linkers (*center*) and (*right*).

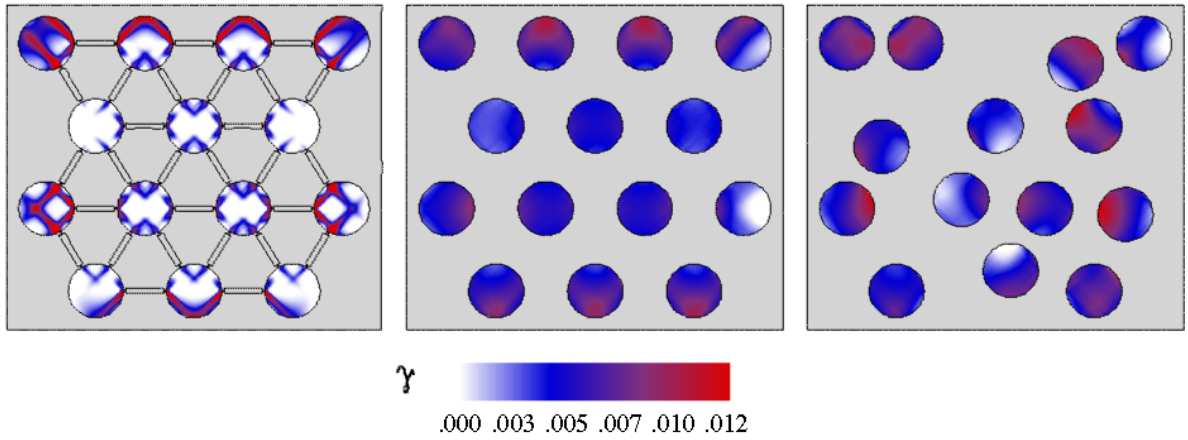


Figure 5.5: Shear slip for superlattices and AuNP-matrix composites without DNA linkers. Concentrated regions of stress in AuNPs from ligands and DNA linkers in AuNP-DNA superlattices resulted in higher slip adjacent to the attachment region. Shear slip was similar for the systems without DNA linkers (*center*) and (*right*).

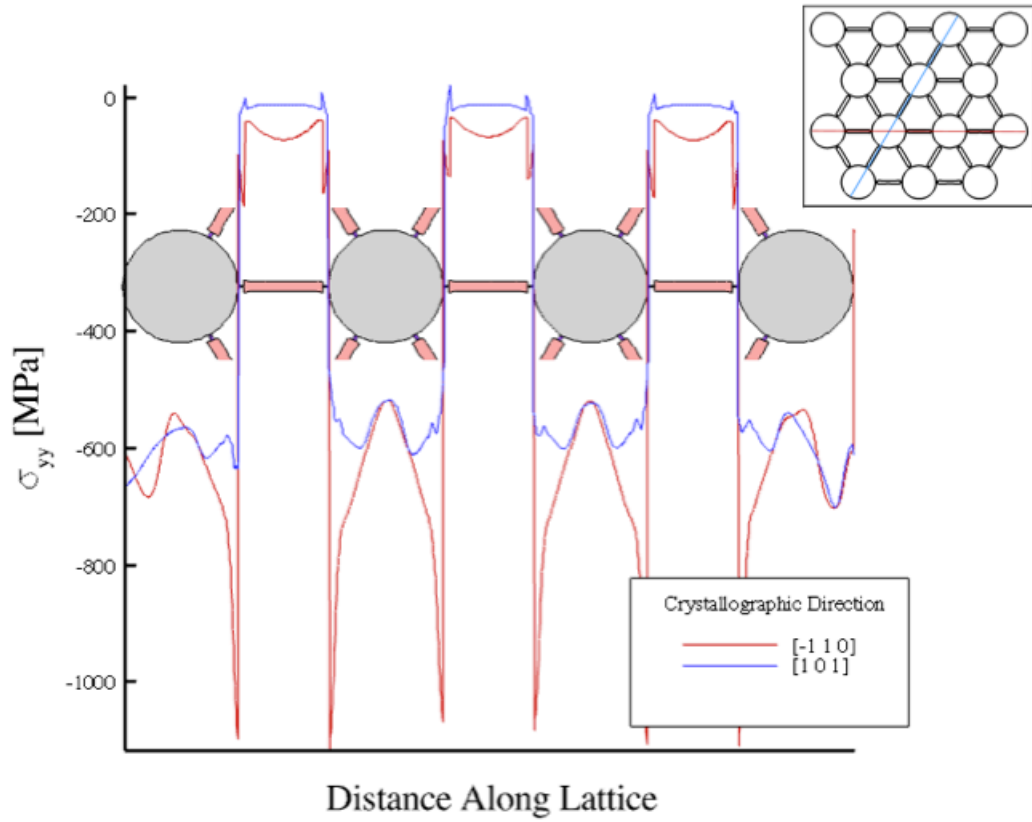


Figure 5.6: Effects of loading direction and anisotropy on stress. Normal stresses are shown along the components in two directions relative to loading, the $[-1\ 1\ 0]$ and $[1\ 0\ 1]$ directions. The interfacial stress gradients strongly correlate with loading direction.

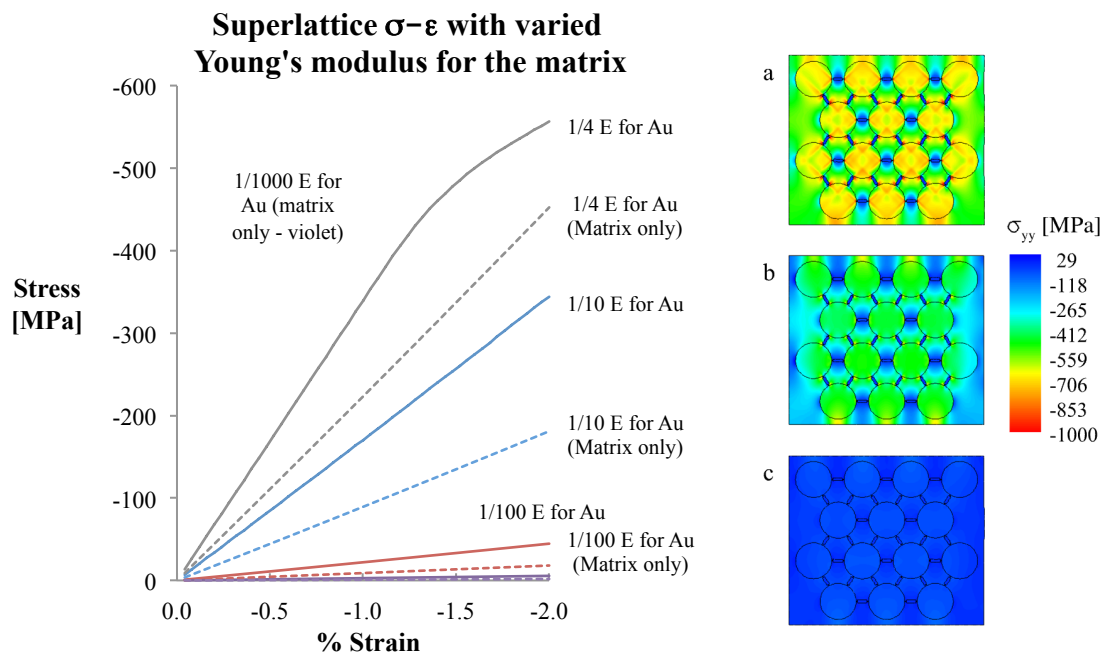


Figure 5.7: Global stress-strain curves for AuNP-DNA superlattices (*left*) and normal stress contours (*right*) with (a) $E_{matrix} = 1/4 E_{Au}$; (b) $E_{matrix} = 1/10 E_{Au}$; (c) $E_{matrix} = 1/100 E_{Au}$.

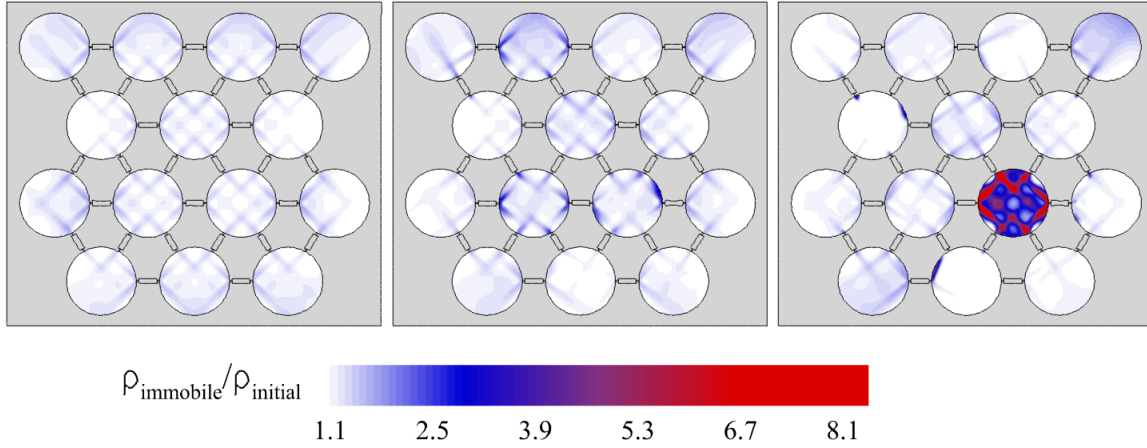


Figure 5.8: Immobile dislocation densities for three AuNP-DNA superlattice composites with different AuNP orientations for slip system (111) $[-1\ 0\ 1]$. The magnitudes of dislocation-densities are highly dependent on the orientation of each AuNP with respect to the loading axis, as shown by (*left*) uniform orientation alignment, (*center*) low angle alignment orientations, and (*right*) high angle alignment orientations. The dislocation-densities have been normalized to their initial values.

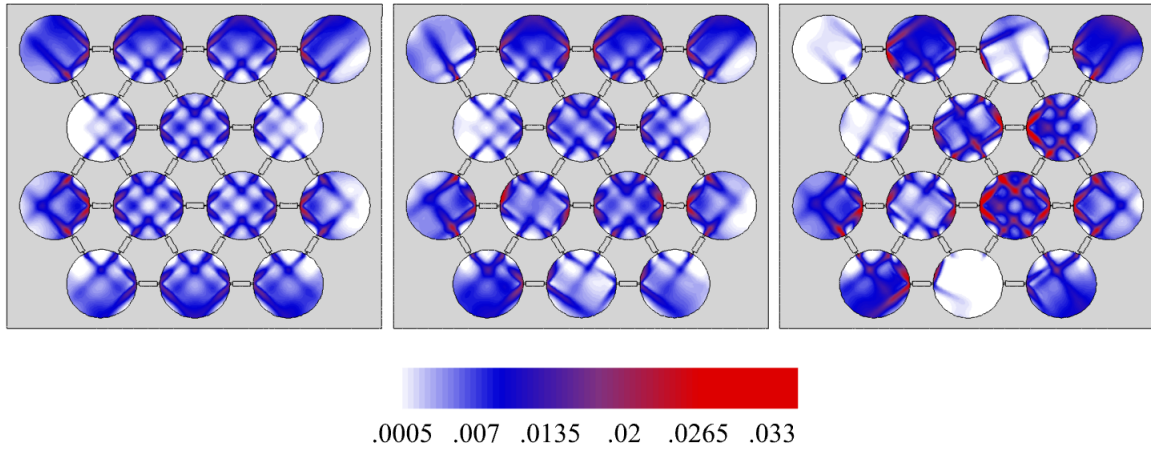


Figure 5.9: Shear slip for three AuNP-DNA superlattice composites with different AuNP orientations for (*left*) uniform alignment orientations, (*center*) low angle random orientations, and (*right*) high angle alignment orientations.

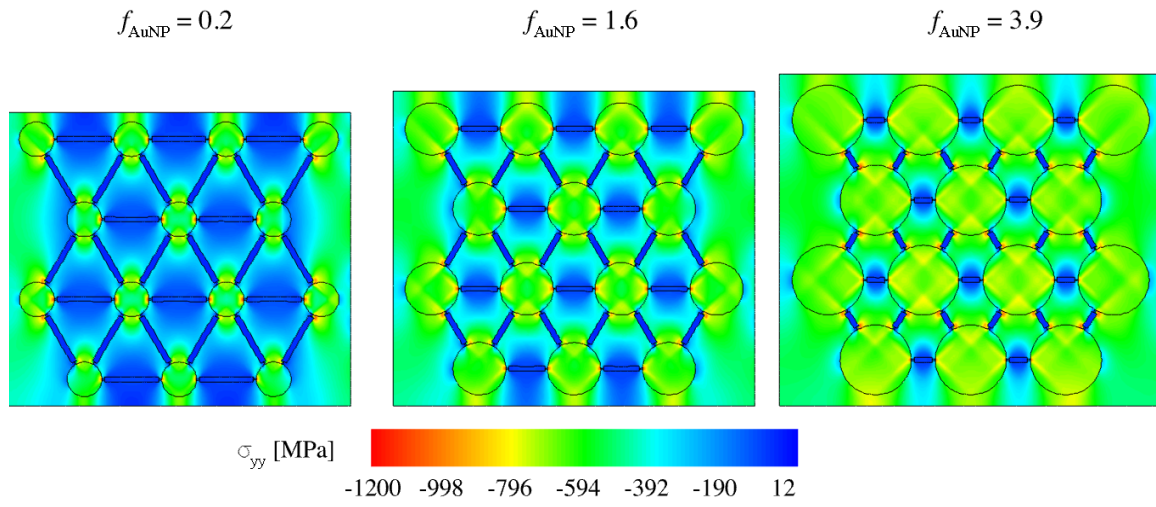


Figure 5.10: Normal stress for different volume fractions but the same hydrodynamic radius.

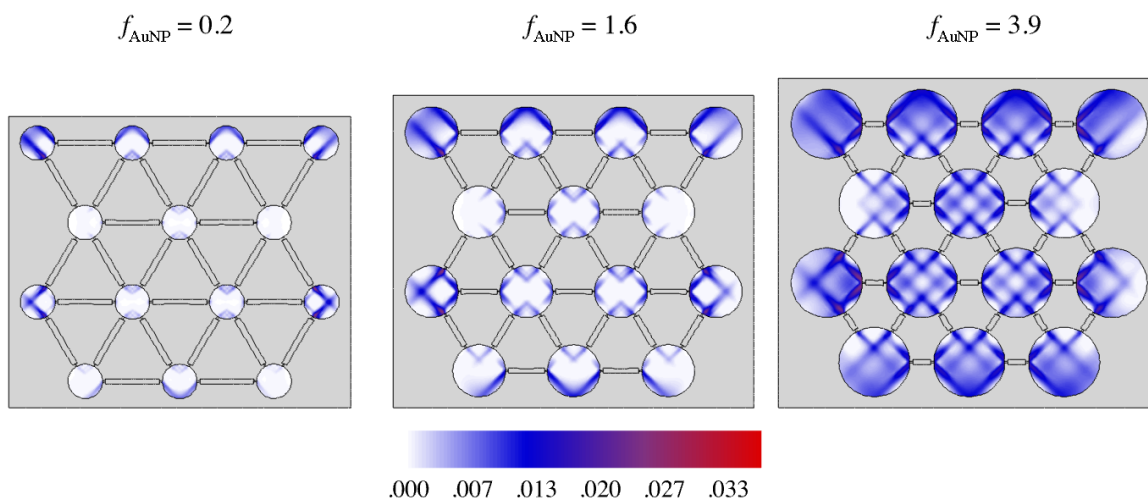


Figure 5.11: Shear slip for different volume fraction and the same hydrodynamic radius.

CHAPTER 6: AuNP-DNA Superlattice Thin Films

Plasmonic thin films consisting of noble metal nanostructures are of strong scientific and technological interest for their surface enhance Raman scattering (Corio, *et al.*, 2000), photocatalysis (Liu, Hou, Pavaskar, Aykol, & Cronin, 2011), and sensing (Tokareva, Minko, Fendler, & Hutter, 2004) in applications pertaining to thin film electronics and biomedical applications. A broad range of architectures for these thin films exist, including deposited nanoislands (Pavaskar, Hsu, Theiss, Hung, & Cronin, 2013), nanoparticles suspended in polymer brushes (Tokareva, Minko, Fendler, & Hutter, 2004), and semiconductor quantum dots metal/insulator sandwiches for solar cells (Pacifci, Lezec, & Atwater, 2007). As the market for plasmonic thin film technology expands, so does the demand for quick, relatively inexpensive manufacturing methods without loss in mechanical functionality.

DNA-AuNP superlattices can provide new applications that can be used and tailored for thin film applications. Bottom-up self-assembly methods of constructing AuNP-DNA systems in colloidal solutions are well documented (Storhoff & Mirkin, 1999; Park, Lazarides, Storhoff, Pesce, & Mirkin, 2004; Mirkin, Letsinger, Mucic, & Storhoff, 1996). Furthermore, the recently developed method of matrix encapsulation (Auyeung, Macfarlane, Choi, Cutler, & Mirkin, 2012) provides the material integrity required for the development of new nanomaterial thin films. Exploiting the opto-electronic properties that are available in precisely structured three-dimensional lattice arrays deposited onto thin film substrates can potentially provide for the demand of sustainable, low cost, and rapidly produced thin film technologies. Because both DNA and AuNPs are biocompatibility, the use of superlattice

thin films may be extended to those necessary for biomedical technologies, provided a suitable biocompatible substrate and encapsulation material is used.

Silicon (Si) is well-characterized, and its use in thin film applications has been thoroughly explored, thus this element is a strong candidate for AuNP-DNA superlattice films. Furthermore, Si also has mechanical features that may be tailored to a desired strength or flexibility. For instance, nano-thin Si layers are “floppy” in contrast to their brittle bulk counterparts (Yong & Ross, 2013). Because of the plasmonic features of AuNP-DNA particle structures, a flexible, biocompatible substrate on which to coat superlattices allows for sensitive sensing in both medical and mechanical realms.

Therefore, the work in this chapter is aimed at providing a first look at AuNP-DNA superlattice thin films. The effect of loading on a Si-encapsulated f.c.c. superlattice coating onto a Si substrate is examined for both tensile and compressive strains. Furthermore, the contribution from the Si substrate is investigated. The results indicate that superlattice thin films are both strong and ductile, however, high tensile and shear stresses may suggest possible failure modes.

6.1 Approach

Using the multiple slip dislocation-density based crystal plasticity and specialized finite element algorithm, Si-encapsulated f.c.c. superlattices and thin films were examined for ductility and strength. For AuNP misorientations, Euler angle distributions were used and are explained in Section 4.1: Approach. The matrix and substrate were assumed to be monocrystalline silicon because of its natural dielectric characteristic suitable for plasmonic devices. Si is an orthotropic material, however, when care is taken to align Si wafers and

thin films in specific orientations, the stiffness matrix may be simplified (Hopcroft, Nix, & Kenny, 2010). Therefore in this study, the Si is assumed to be oriented such that its (1 0 0) plane is aligned normal to the loading direction, and the stiffness can be represented by a single value for the elastic modulus (see Table 6.1). However, the Si matrix and substrate purposely remain elastic throughout the loading intervals by artificially raising its yield strength, $\sigma_{Y,si}$. This allows the plastic response in the system to be limited to the AuNPs, creating a focused view of the nanocrystalline deformation throughout loading.

The thin film was modeled as one continuous Si material, *i.e.* there is no physical boundary between the substrate and lattice. Loading was applied in the [0 -1 0] direction relative to the AuNP orientations, and simultaneously in the [-1 0 0] direction relative to the Si substrate orientation. In other words, the AuNP and Si orientations are not aligned. Similar to Chapter 5, the AuNP-DNA superlattice shown in Figure 6.1 is a cross-section of the (1 1 1) close packed plane, such that the strain displacements are applied along the [1 1 2] superlattice direction. All loading is in the form of plane strain displacements and each system is consistently loaded to 1.6% nominal strain, both compressively and tensile. The thin film model was approximately 220 nm by 120 nm, and incorporated approximately 18 nm circular AuNPs with approximately 12 nm dsDNA.

Comparisons were also made between the AuNP-DNA f.c.c. superlattice as a stand-alone composite material and also with the addition of the Si substrate. The system in Figure 6.2 was modeled under the same loading conditions as the thin film, as outlined above. All material properties are identical and may be found in Table 6.1.

6.2 Results

6.2.1 Thin Film Superlattice Behavior in Compression and Tension

Figure 6.3 shows the normal stresses in the thin film under compressive loading conditions. The dashed line denotes the interface between the substrate and encapsulated f.c.c. superlattice coating. Peak stresses were greater than -6600 MPa in the Si matrix and occurred near the free edge (Figure 6.3). The average normal stresses in the matrix's central region were approximately -700 MPa, and approximately -1300 MPa in the AuNPs. The DNA's modulus and negative Poisson's ratio somewhat negate compressive stresses in the region local to the biopolymer. High stress gradients at the ligand-AuNP interface exist, as they did in the two particle systems and AuNP-DNA f.c.c. superlattice composites (see Chapter 5).

The superlattice thin film in tension yielded similar stress topography when loaded to 1.6% nominal tensile strains as with compression, however, the actual value of the stresses was different (Figure 6.4). The average tensile stresses in the Si matrix exceeded the maximum compressive stresses by 16%, but for the AuNPs, tensile loading created slightly larger stresses. This anisotropic response can be due to the substrate thickness and elastic deformation dominating thin film behavior. Figure 6.4 shows tensile results, and for the sake of comparison the contour coloring has been modified so that, as in Figure 6.3, red represents the highest stresses, be they compressive or tensile. The high tensile stresses, which are approximately 6.5 times the Young's modulus of bulk Au, is an indication that the film can delaminate under these opening mode stresses (See, for example, Ashmawi, *et al.*, 2004), especially in the presence of the free edge singularity (He, Hutchinson & Evans, 2011). For

the free edge (*right side of thin film*), tensile stresses are highly elevated compared to the Si matrix and across the superlattice coating-substrate interface, indicating possible opening mode fracture at the interface.

Furthermore, loading of the thin film resulted in very high shear stresses, as shown in Figures 6.5 and 6.6. The highest shear stresses were exhibited in the compressive case (Figure 6.5), and occurred between the AuNP and matrix. The maximum shear stresses for the thin film in compression exceeded those in tension by 25%. Shear stresses of this magnitude could signify failure, however, superlattice AuNPs are coated with tens to hundreds of oligonucleotides, meaning the AuNP is bonded with ligands as well as abut against the Si boundary, hence straightforward predictions for failure in the regions with large shear stresses close to the AuNP surface is impossible from this method.

Shear slip, the measure of all plasticity on all slip systems, is shown in Figures 6.7 and 6.8 for compression and tension. In the case of tension AuNPs, especially in the central regions, were pulled apart and experienced the most plastic deformation closer to the center of the AuNPs. Compressed AuNPs, on the other hand, were mostly affected by the DNA-ligand interactions at the AuNP-ligand interface. The most severe deformation and plastic accumulation took place in this region, as shown in the inset in Figure 6.5, as well as in the compressive models described in Chapters 3 and 4. Most importantly, the substantial plastic responses between the two systems have proven AuNPs within the thin films are endowed with ductility, allowing them to react to the increasing strains in the matrix and from concentrated stresses from the DNA-ligand scaffolds.

6.2.2 Film-substrate Strength and Behavior

To investigate the mechanical contributions of adhering the f.c.c. superlattice to a Si substrate in the form of a coating material, an f.c.c. AuNP-DNA composite with a Si matrix (Figure 6.2) was also modeled. The resulting stress-strain curve (Figure 6.10) shows that the addition of Si substrate has greatly increased the strength of the material, since the slope of the stress-strain is higher for the thin film. Contours in Figure 6.11 confirm this result, since the maximum normal compressive stress is roughly half that of the thin film. The average normal stress in the central region of the material is also approximately -750 MPa, which is also twice as small as the thin film's average interior normal stress. These results signify a good relationship between the substrate and the coating, in which the substrate provides strength, and hence increased stability, to the f.c.c. superlattice composite. Additionally, Si has intrinsic advantages not limited to protection from corrosion and wear.

The superlattice composite itself imparts a tensile and compressive stress onto the substrate when loaded in compression and tension. Figure 6.12 displays the normal stresses for the thin film in compression, but with contours adjusted to highlight the stress topography specific to the substrate. The substrate is characterized by a reduction in compressive stress, attributed to it from the superlattice material, and creates an approximate 400 MPa stress gradient laterally along the substrate. The affected region of the substrate's interior was also observed in shear stresses, given in Figure 6.6 for the tensile case. The interface between the substrate and coating, denoted by the dashed line, experienced a moderate increase in negative shear stresses. In this analysis, this region was modeled as a continuum of the Si matrix, however, if an interfacial region owing to the lattice mismatches from coating the

substrate was present, the increased shear could facilitate delamination between the two materials. However, ductility is also increased in the AuNPs upon the addition of a Si substrate. Figure 6.9 displays a 4% increase in mobile dislocations on the most active slip system $(-1\ 1\ 1)$ $[0\ -1\ 1]$ for the thin film as opposed the superlattice matrix composite without substrate.

6.3 Conclusions

The presented analysis of AuNP-DNA superlattice thin films, specifically under the effect of tensile and compressive loading, further demonstrated the AuNPs ductility under the influence of extensive deformations. Additionally, on a global level the results indicated that the Si substrate provides strengthening in compression, but local opening mode stresses near the interface can result in delamination. Therefore, for increasing film thicknesses, delamination would be more likely because opening mode stresses will be higher for tensile loading conditions. For compressive loading conditions, as the film thickness increases, failure would be likely due to high shear stresses.

REFERENCES – Chapter 6

- Ashmawi, W. M., Zikry, M. A., Wang, Kai, & Reeber, R. R. (2004). Modeling of residual stresses for thermally strained GaN/Al₂O₃ heterostructures. *Journal of Crystal Growth*, 266 (4), 415-422.
- Auyeung, E., Macfarlane, R. J., Choi, C. J., Cutler, J. I., & Mirkin, C. A. (2012). Transitioning DNA-engineered nanoparticle superlattices from solution to the solid state. *Advanced Materials*, 24, 5181-5186.
- Bensimon, D., Simon, A. J., Croquette, V., & Bensimon, A. (1995). Stretching DNA with a receding meniscus: Experiments and models. *Physical Review Letters*, 74 (23), 4754-4757.
- Corio, P., Brown, S. M., Marucci, A., Pimenta, M. A., Kneipp, K., Dresselhaus, G., *et al.* (2000). Surface-enhanced resonant Raman spectroscopy of single-wall carbon nanotubes adsorbed on silver and gold surfaces. *Physical Review B, Condensed Matter*, 61 (19), 13202-13211.
- He, M. Y., Hutchinson, J. W., & Evans, A. G. (2011). A stretch/bend method for in situ measurement of the delamination toughness of coatings and films attached to substrates. *Transactions of the American Society of Mechanical Engineers*, 78, 011009-1-011009-5.
- Hopcroft, M., Nix, W. D., & Kenny, T. W. (2010). What is the Young's modulus of silicon? *Journal of Microelectromechanical Systems*, 19 (2), 229-238.
- Liu, Z., Hou, W., Pavaskar, P., Aykol, M., & Cronin, S. B. (2011). Plasmon resonant enhancement of photocatalytic water splitting under visible illumination. *Nano Letters*, 11, 1111-1116.
- Manning, G. S. (1986). Correlation of polymer persistence length with Euler buckling fluctuations. *Physical Review A*, 34 (5), 4467-4468.
- Manning, G. S. (2012). Poisson's ratio for a polyelectrolyte. *Soft Matter*, 8, 9334-9337.
- Mirkin, C. A., Letsinger, R. L., Mucic, R. C., & Storhoff, J. J. (1996). A DNA-based method for rationally assembling nanoparticles into macroscopic materials. *Nature*, 382, 607-609.
- Pacifici, D., Lezec, H., & Atwater, H. A. (2007). 73. All-optical modulation by plasmonic excitation of CdSe quantum dots. *Nature Photon*, 1, 402-406.

- Park, S.-J., Lazarides, A. A., Storhoff, J. J., Pesce, L., & Mirkin, C. A. (2004). The structural characterization of oligonucleotide-modified gold nanoparticle networks formed by DNA hybridization. *Journal of Physical Chemistry B*, *108*, 12375-12380.
- Pavaskar, P., Hsu, I.-K., Theiss, J., Hung, W. H., & Cronin, S. B. (2013). A microscopic study of strongly plasmonic Au and Ag island thin films. *Journal of Applied Physics*, *113*, 034302.
- Storhoff, J. J., & Mirkin, C. A. (1999). Programmed materials synthesis with DNA. *Chemical Reviews*, *99* (7).
- Tokareva, I., Minko, S., Fendler, J. H., & Hutter, E. (2004). Nanosensors based on responsive polymer brushes and gold nanoparticle enhanced transmission surface plasmon resonance spectroscopy. *Journal of the American Chemical Society*, *126*, 15950-15951.
- Yong, E., & Ross, V. (2013). Stretchy, flexy future. *Discover*, *7* (34), 30-35.

Table 6.1: Elastic properties of the AuNP-DNA superlattices and Si matrix.

	AuNP	Ligand	DNA	Si Matrix
E (GPa)	70.0	0.35	0.11 ^a	130 ^c
ν	0.42	0.35	-0.70 ^b	0.28 ^c
σ_Y (MPa)	200	1000	1000	10000

^a (Bensimon, *et al.*, 1995);

^b (Manning, 1986, Manning, 2012)

^c (Hopcroft, Nix, & Kenny, 2010)

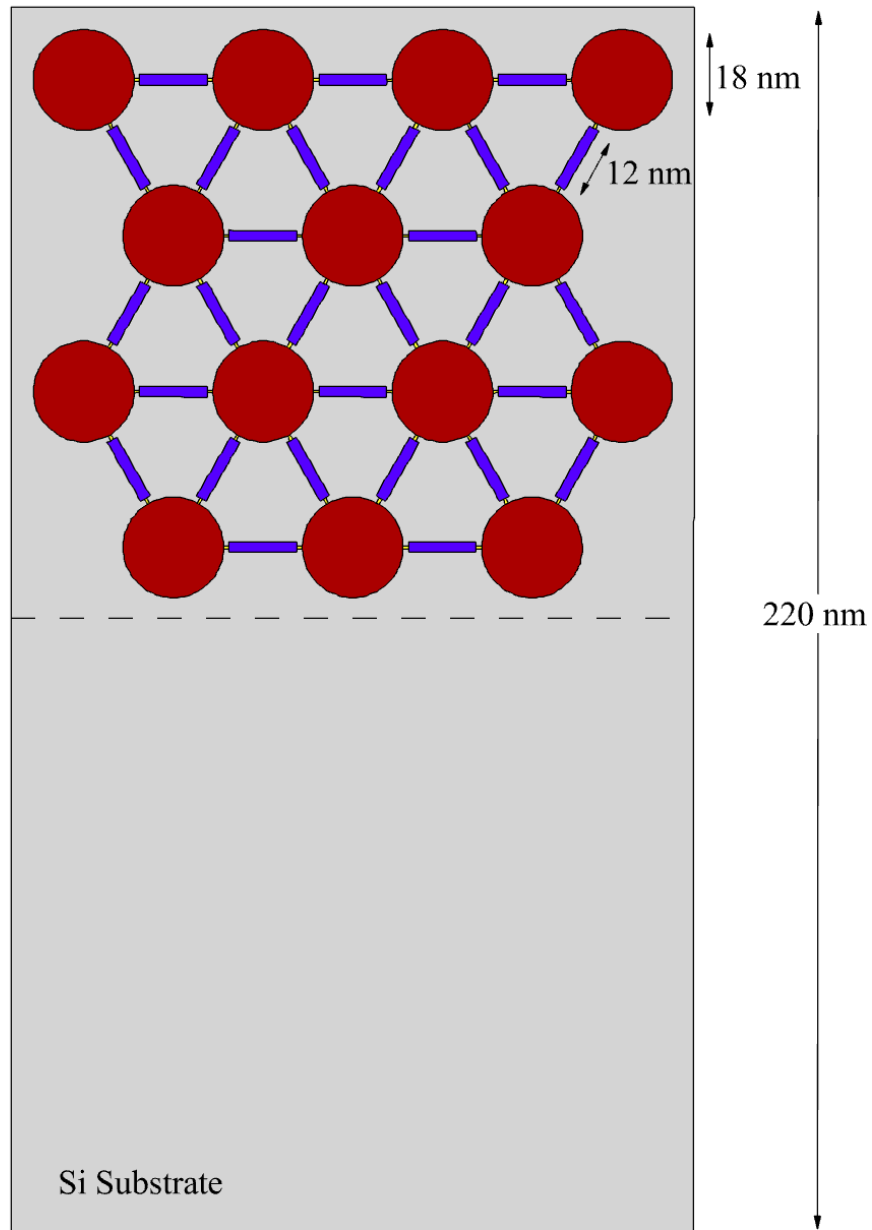


Figure 6.1: The thin film model. The dashed line represents the continuous boundary between the substrate and the encapsulated Si particle lattice.

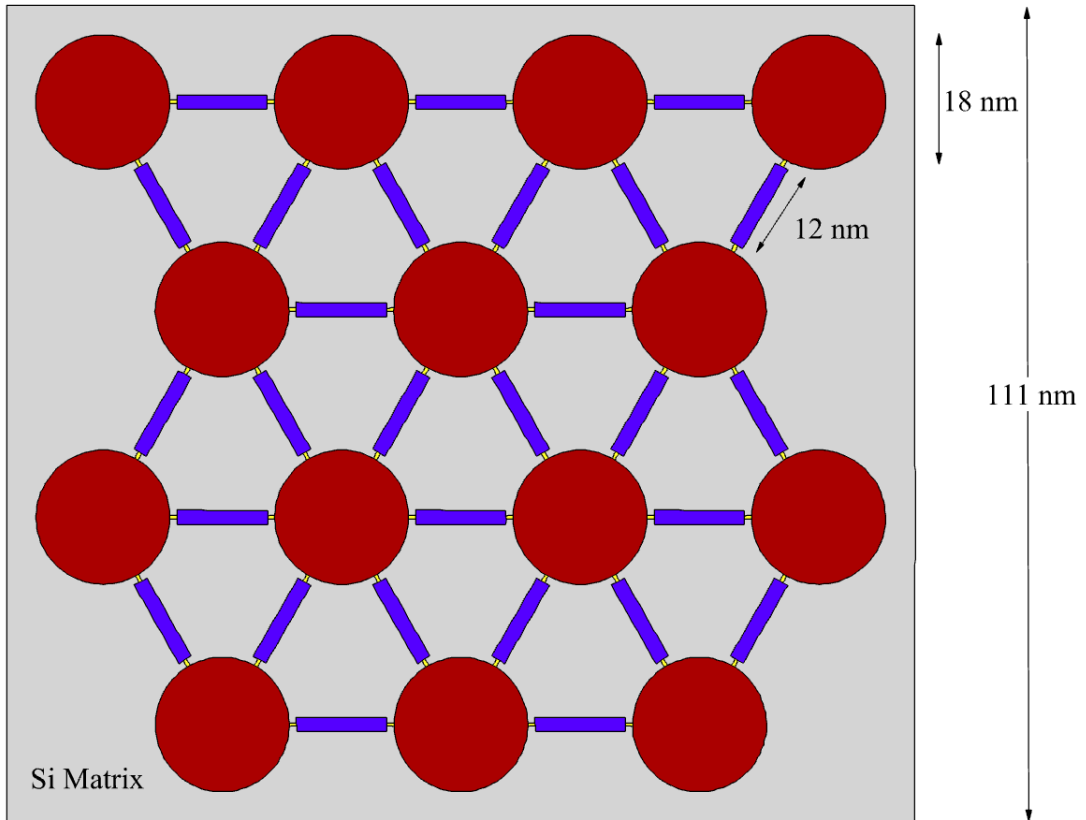


Figure 6.2: The superlattice-Si composite model.

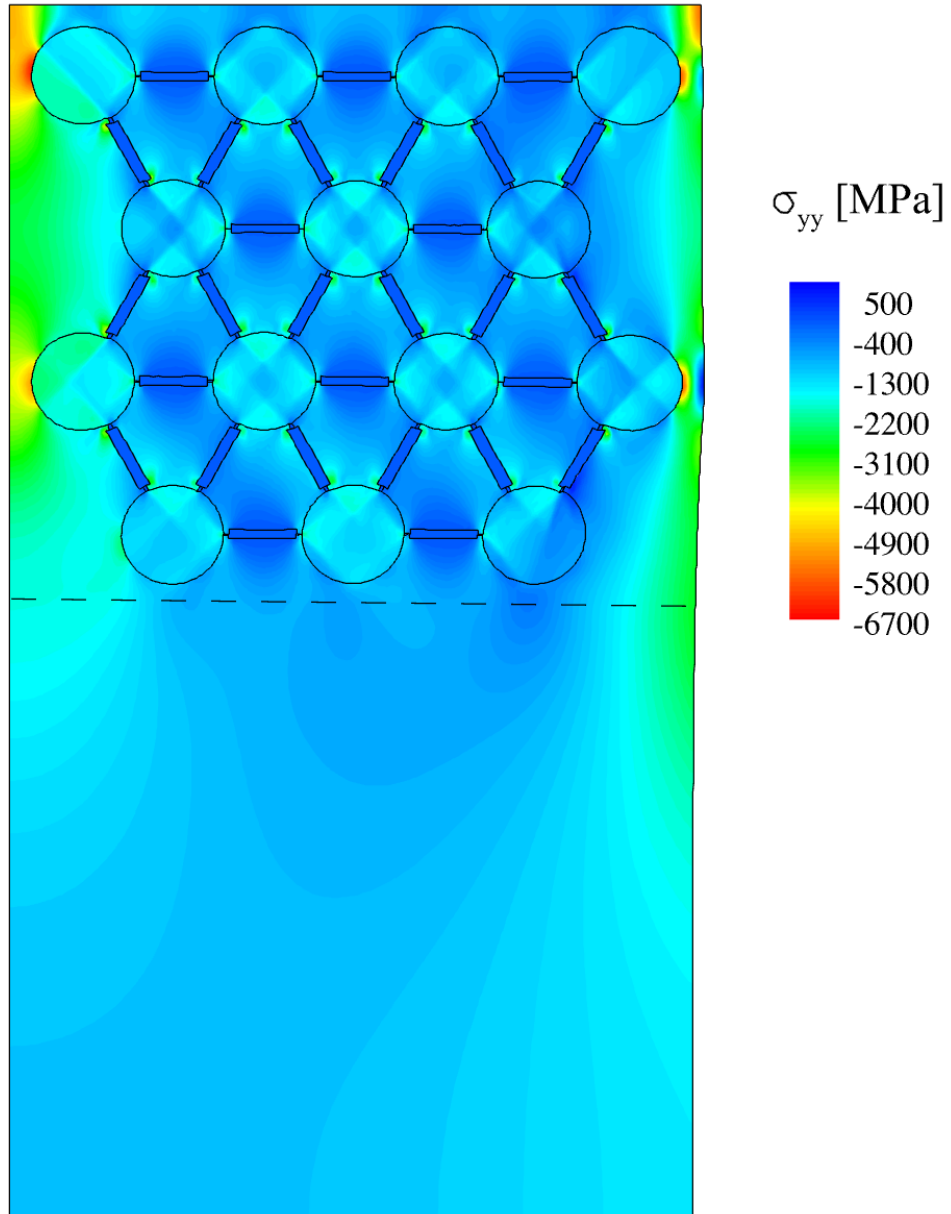


Figure 6.3: Normal stress in the f.c.c. superlattice thin film in compression. The dashed line represents the continuous interface between the substrate and the encapsulated Si particle lattice.

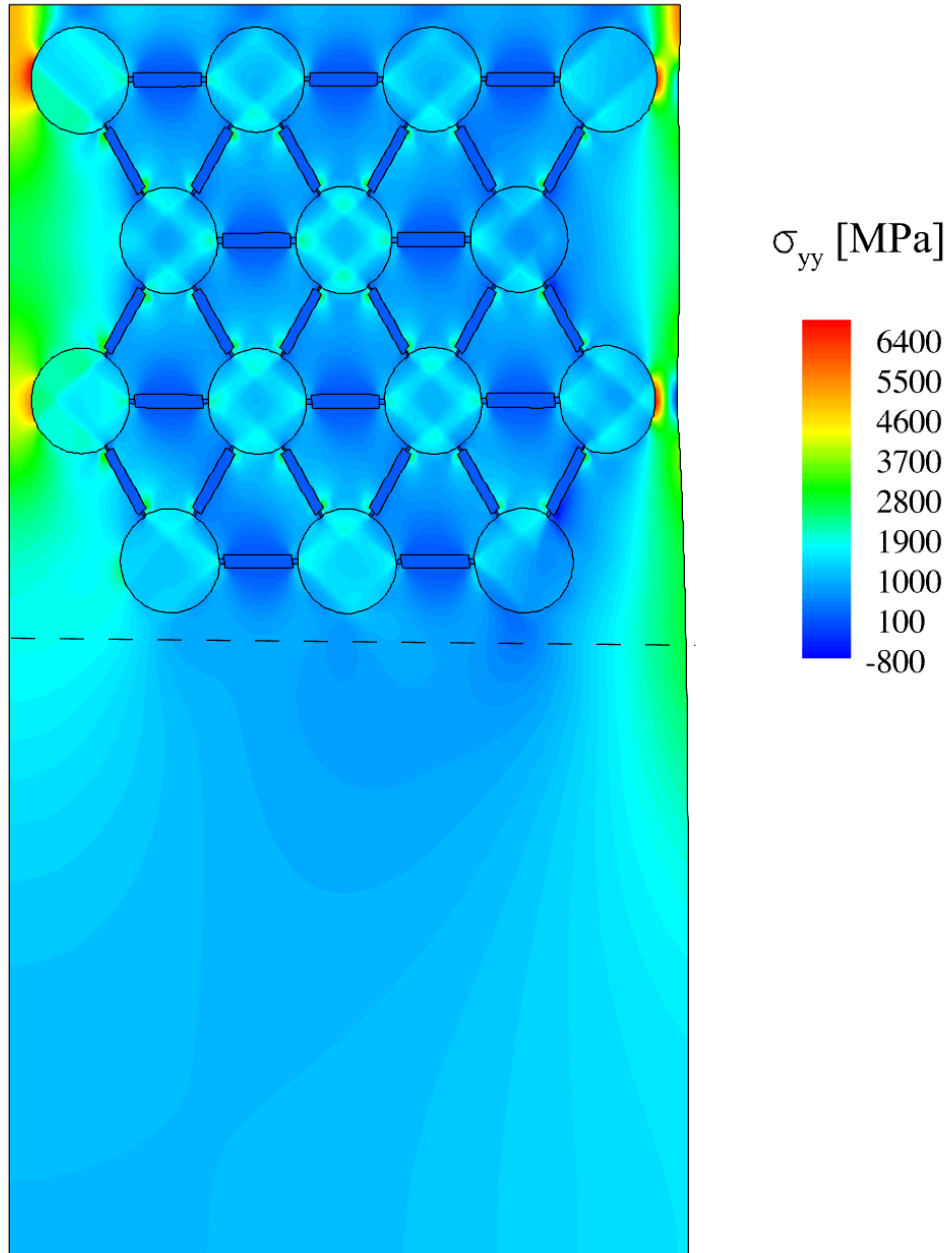


Figure 6.4: Normal stresses in the f.c.c. superlattice thin film in tension.

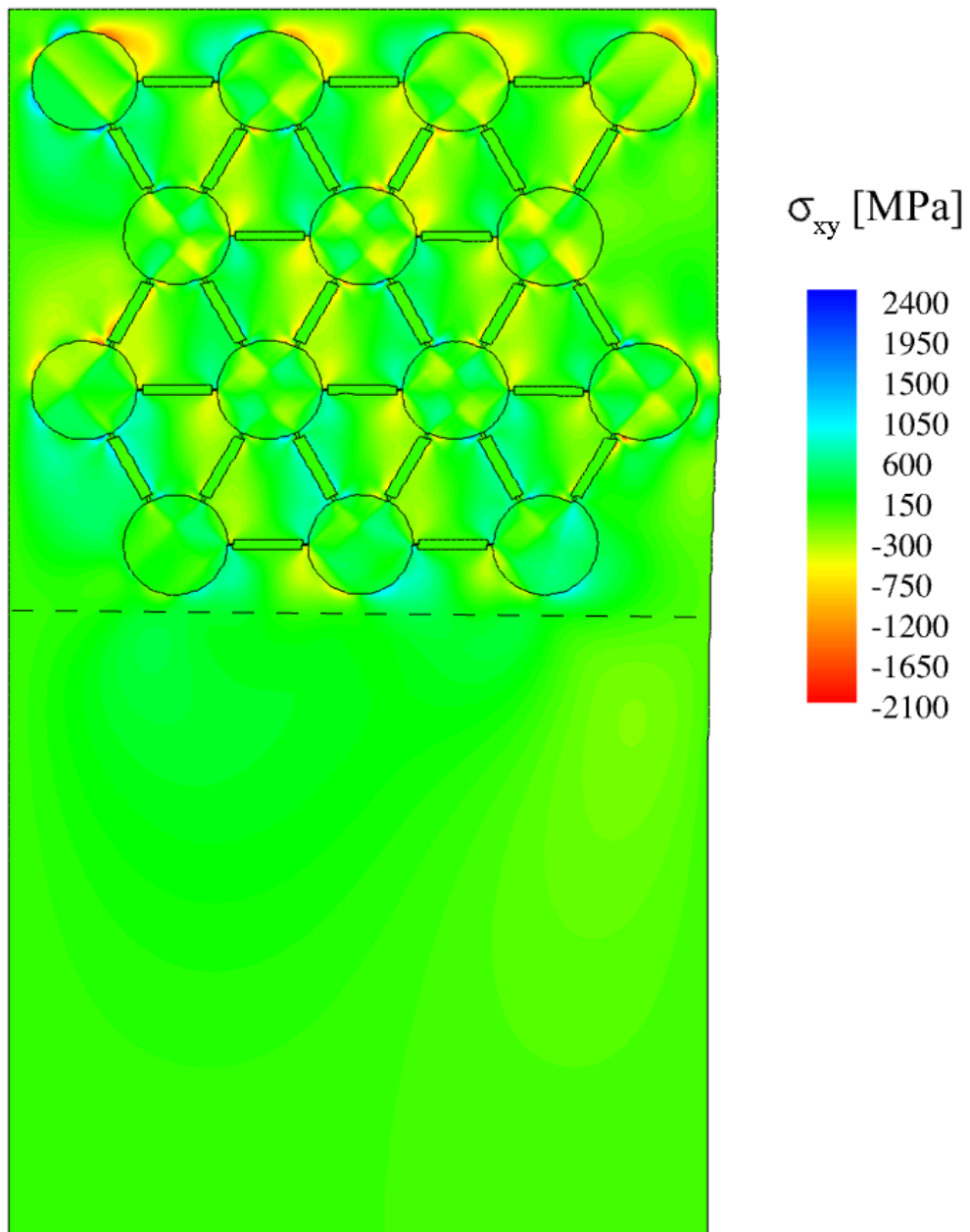


Figure 6.5: Shear stresses for the AuNP-DNA thin film in compression.

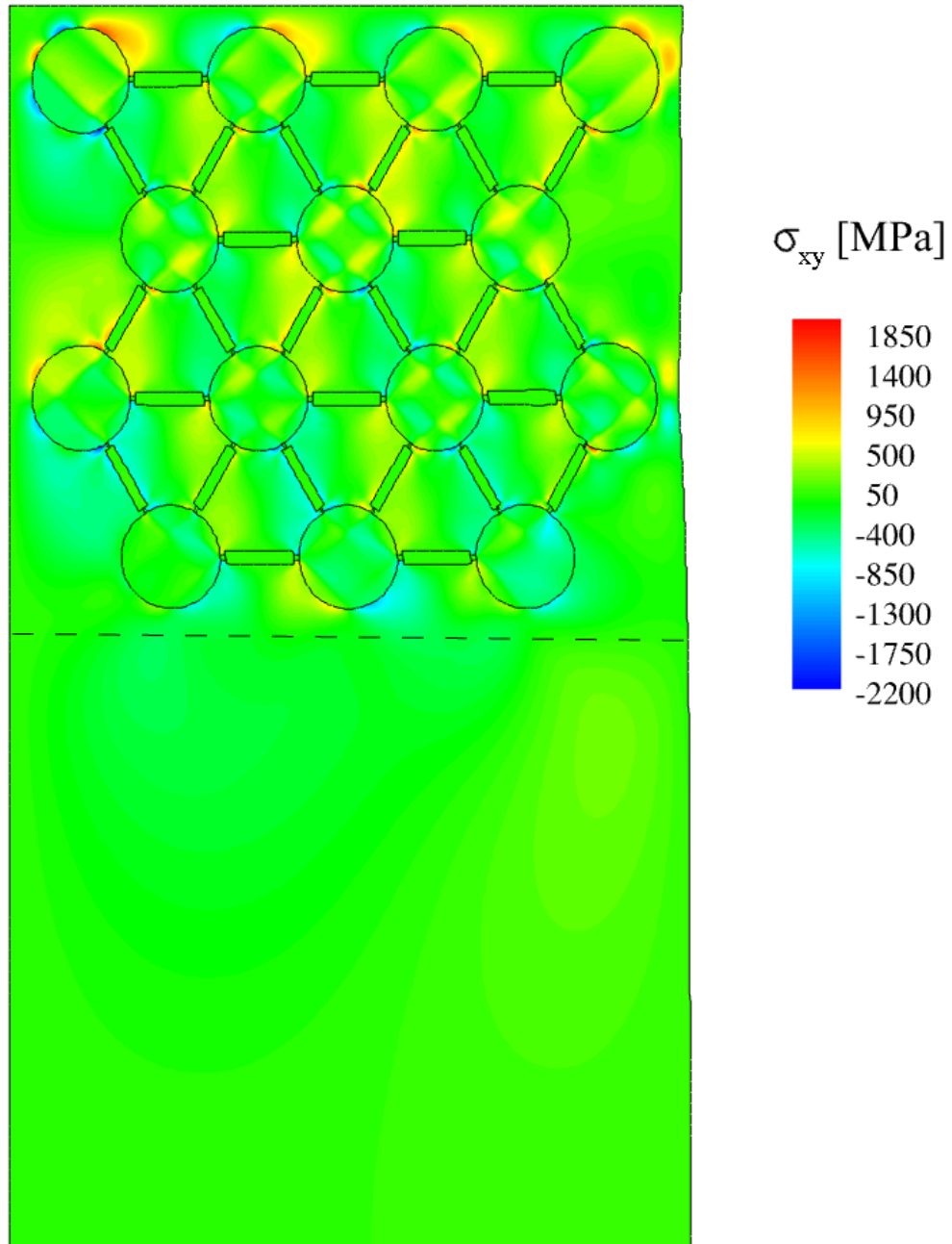


Figure 6.6: Shear stress for the AuNP-DNA superlattice thin film in tension.

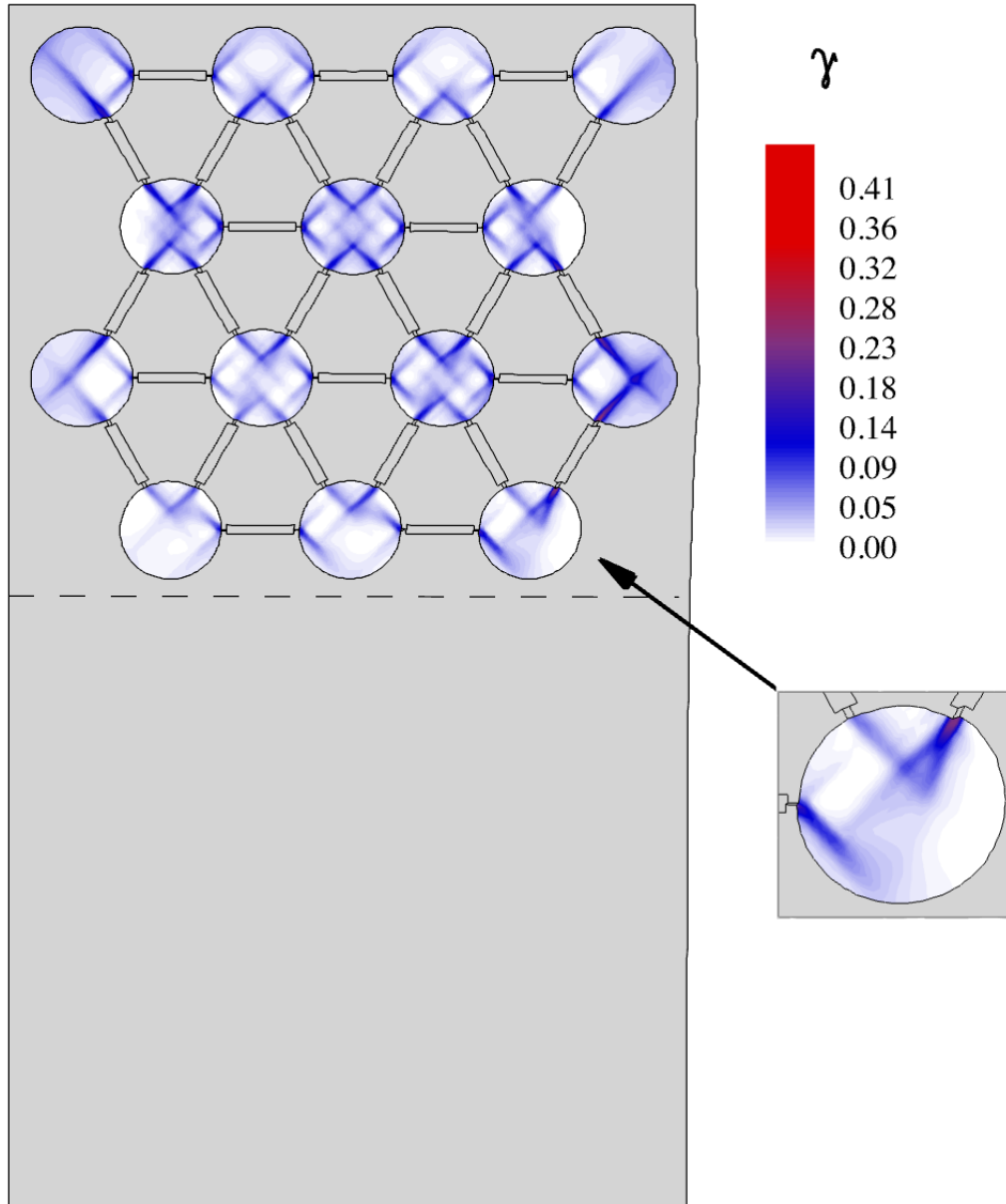


Figure 6.7: Shear slip for a thin film in displaced to 1.6% nominal compressive strain. Highest plasticity occurred in the deformed AuNP shown in the inset.

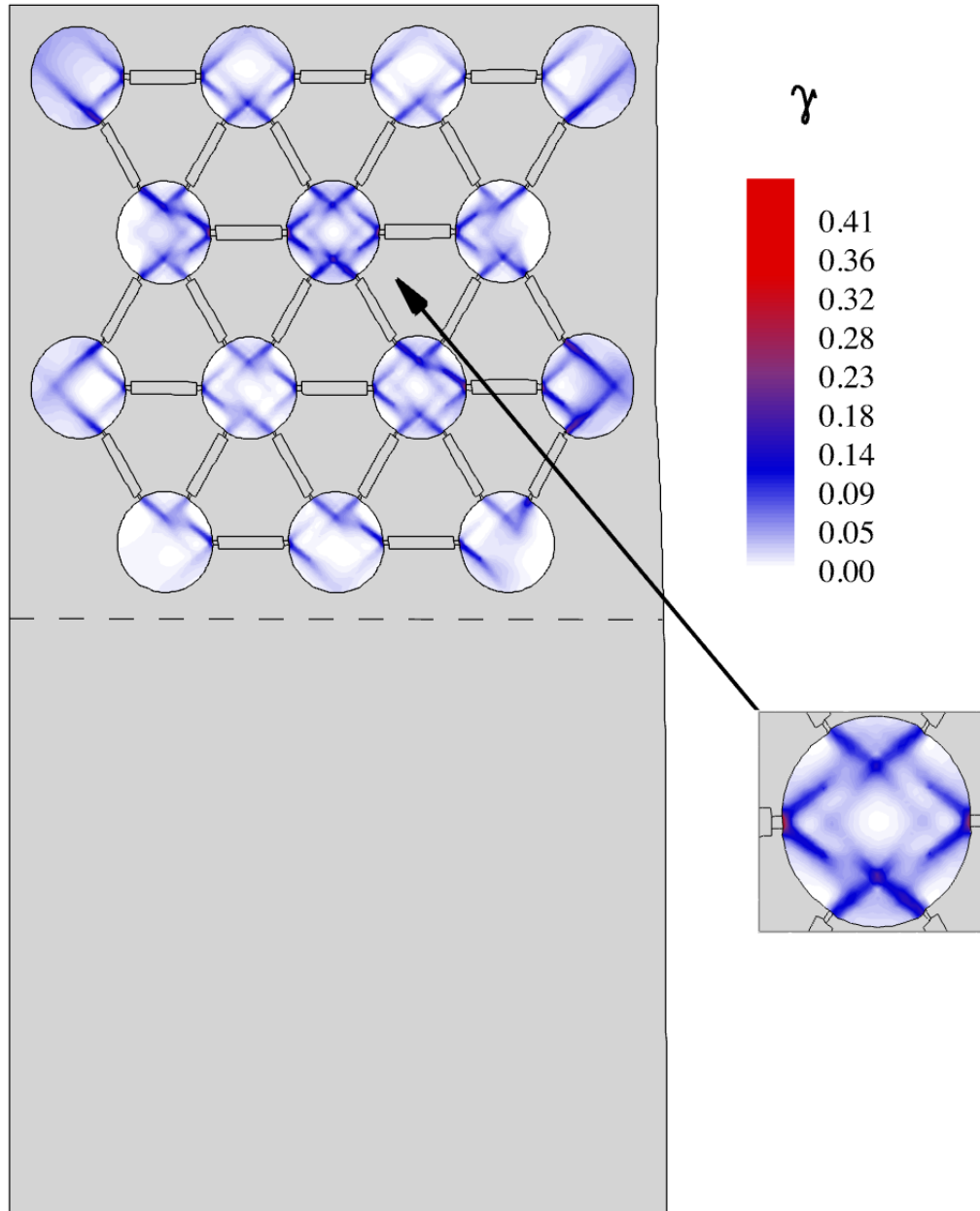


Figure 6.8: Shear slip for a thin film displaced to 1.6% nominal tensile strain. Highest plasticity occurred in the central most AuNP, as shown in the inset.

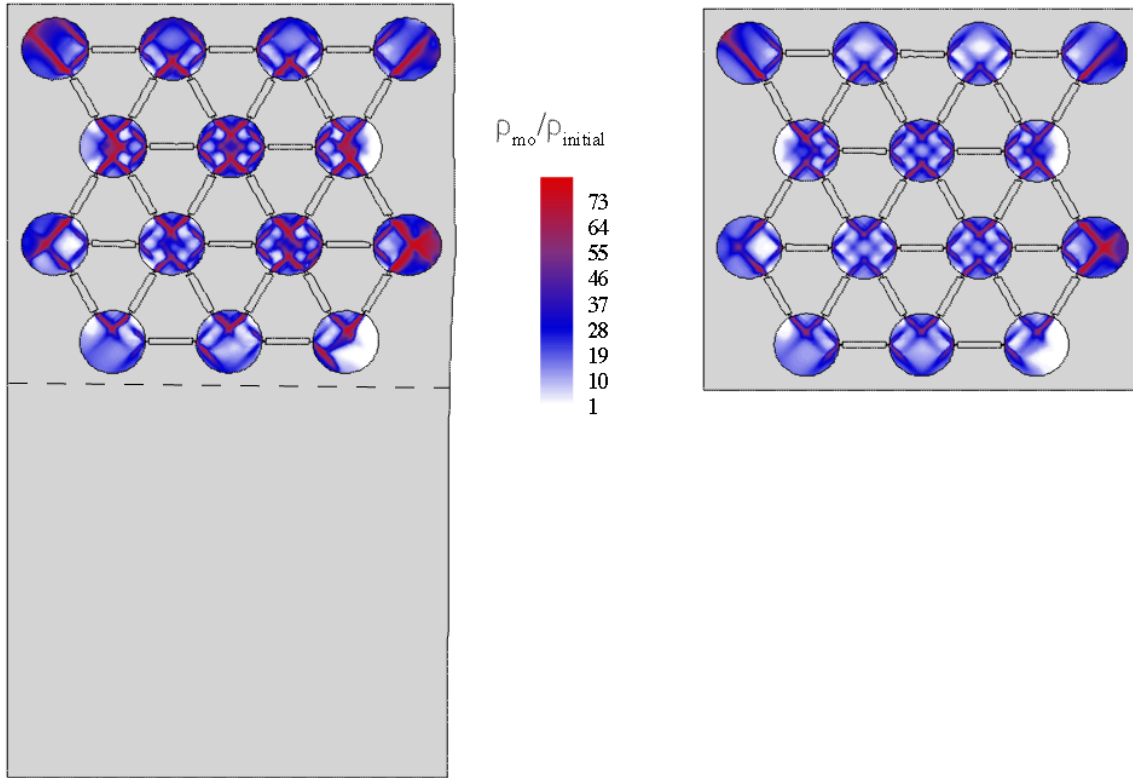


Figure 6.9: Mobile dislocation-densities are lower for the AuNP-DNA superlattice (*right*) and the thin film (*left*) for the most active slip system $(-1\ 1\ 1)\ [0\ -1\ 1]$.

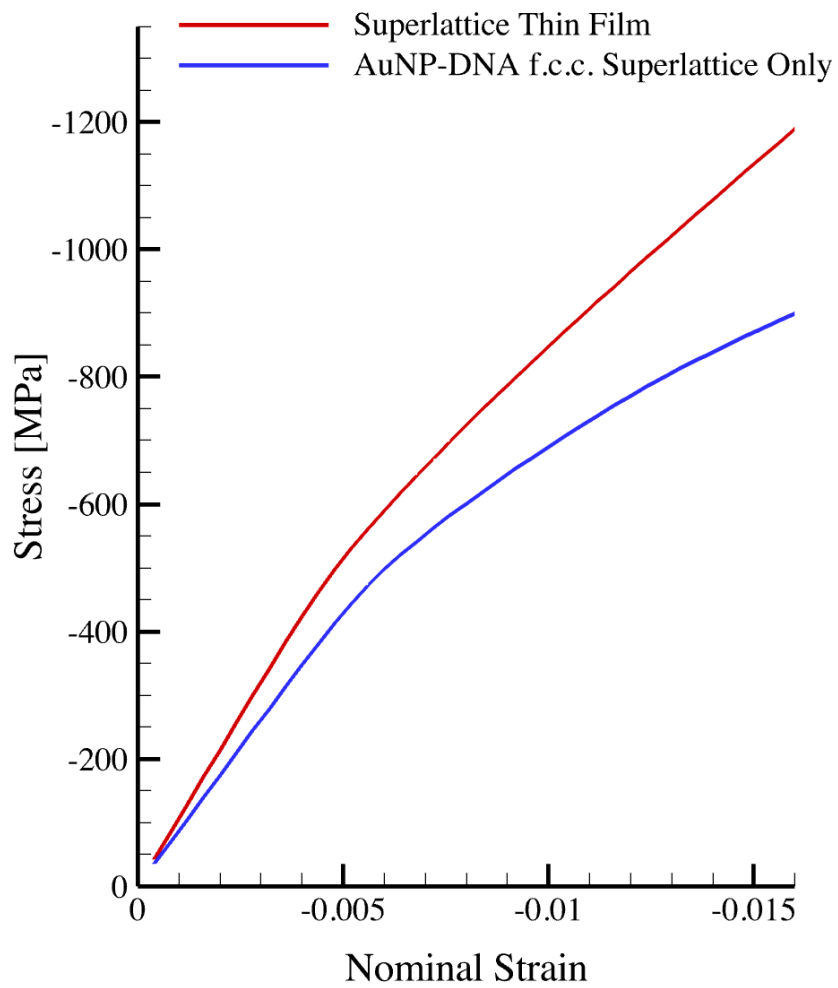


Figure 6.10: Stress-strain curves for (*red*) the AuNP-DNA superlattice thin film and (*blue*) the AuNP-DNA lattice coating only (see Figure 6.1,2).

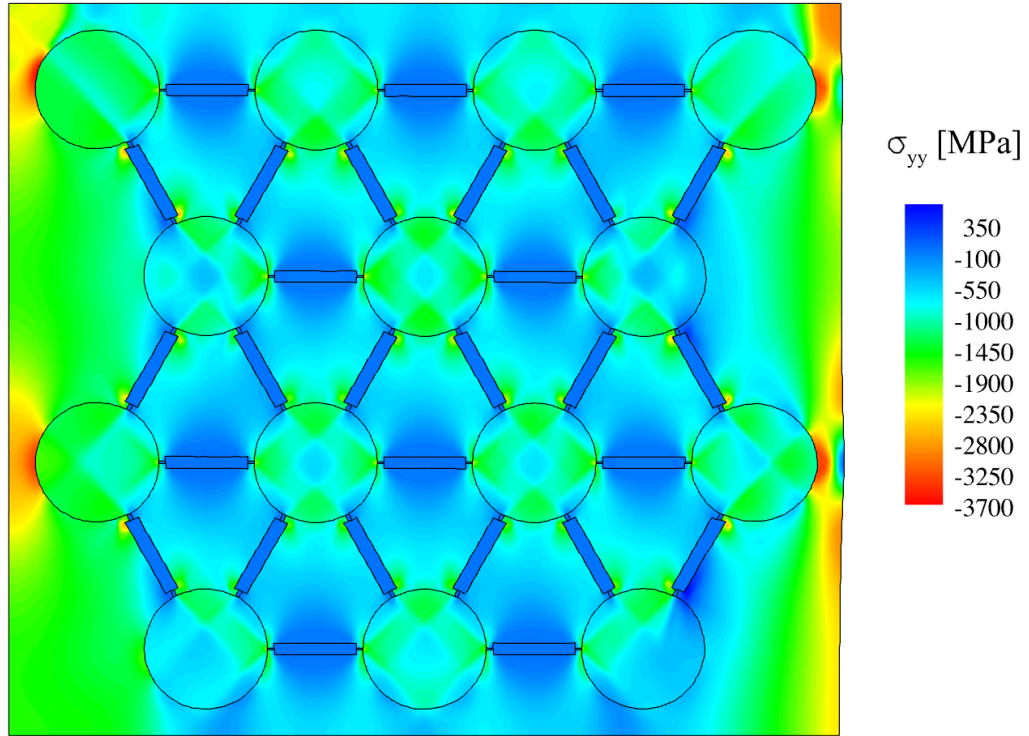


Figure 6.11: Normal stress in the f.c.c. superlattice-Si composite.

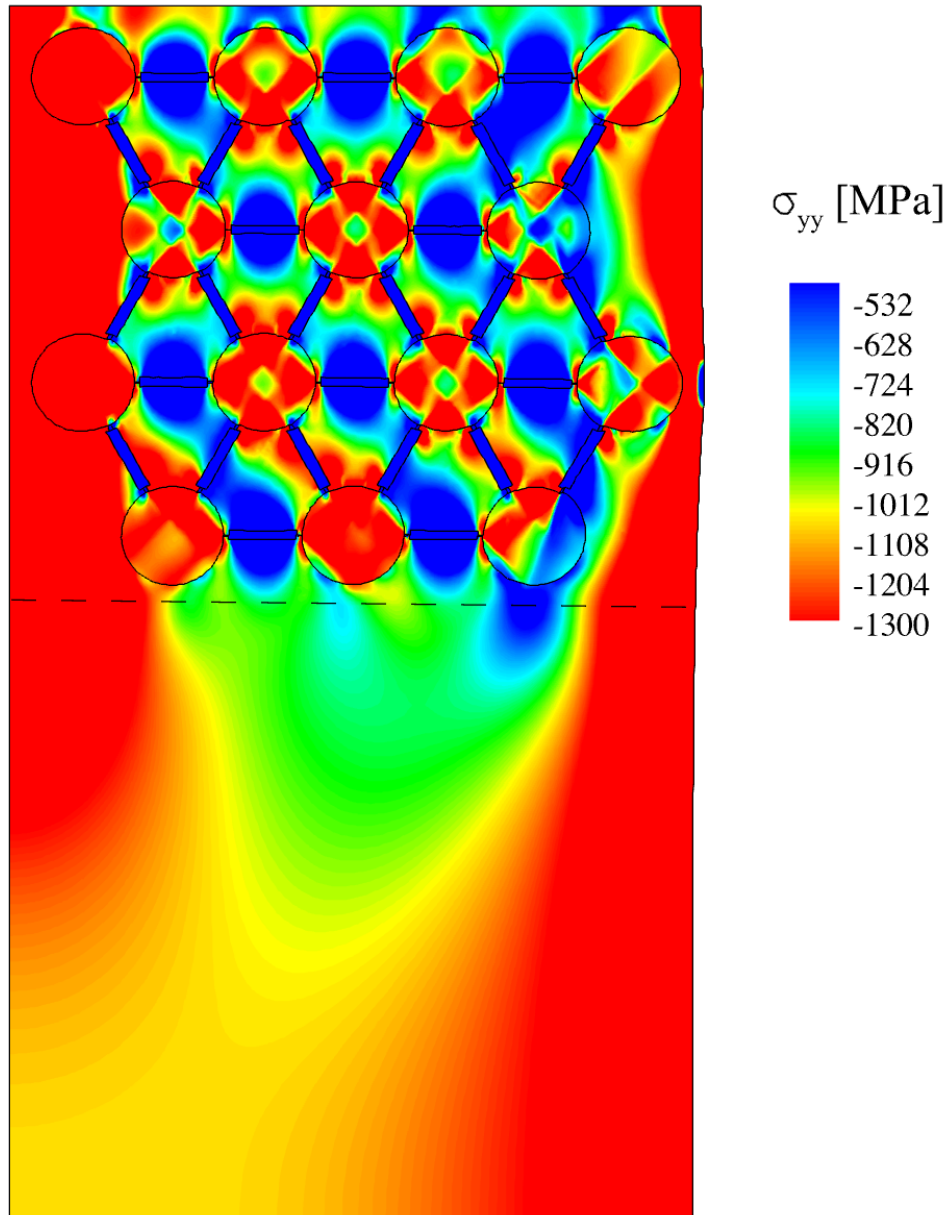


Figure 6.12: Normal stresses for the thin film in compression with contours adjusted to emphasize compressive stress contribution from the superlattice into the substrate.

CHAPTER 7: Future Research Recommendations

- Expand the superlattice analysis to three dimensions to observe the full range of anisotropic loading responses. Specifically, three-dimensions will allow out-of-plane ligand-DNA attachment, such that more loading directions and directionalities of stress evolution and inelastic deformations may be examined.
- Observe the effects of different hydrodynamic radii and the same hydrodynamic radii but with varied particle sizes. Chapter 5 showed the importance of AuNP volume fraction, and Auyeung, *et al.*, have shown different hydrodynamic radii are responsible for creating a variety of lattice structures like CsCl, etc (2012). Hence, exploring these variations would give a great breath to mechanical strength and stability of AuNP-DNA systems.
- Examine the relationship between stress and the plasmon absorbance wavelengths. It is well established that distances between AuNPs and the size of particles both alter the wavelength at which LSPR occurs, and both of these factors are potentially altered during loading. Creation of a coupled relationship between stress and plasmon absorption would be a major contribution to AuNP-DNA systems, as well as many other plasmonic analyses.

REFERENCES – Chapter 7

- Auyeung, E., Macfarlane, R. J., Choi, C. J., Cutler, J. I., & Mirkin, C. A. (2012).
Transitioning DNA-engineered nanoparticle superlattices from solution to the solid
state. *Advanced Materials*, 24, 5181-5186.